

REPUBLIQUE ALGERIENNE DEMOCRATIQUE ET POPULAIRE
MINISTRE DE L'ENSEIGNEMENT SUPERIEUR ET DE LA RECHERCHE
SCIENTIFIQUE

UNIVERSITE DE RELIZANE
Faculté des sciences et Technologies
Département de physique



Thèse de doctorat LMD 3^{ème} Cycle

Filière : Science de la matière

Spécialité : Physique Énergétique et Énergies Renouvelables

Présenté par

Mr DAHAMNI Mohamed Elamine

Titre de thèse :

Synthèse par voie chimique des couches nanométriques d'oxydes métalliques (M-O, M-O₂) transparents et leurs caractérisations morphologiques, optiques et électrique.

Devant le jury compose de :

Président	MESBAH Smain	MCA	Université Relizane
Directeur de these	GHAMNIA Mostefa	PR	Université Oran 1
Co-directeur de thèse	BOUADI Abed	MCA	Université USTO-Oran
Examineur	NAIM Houcine	MCA	Université USTO-Oran
Examineur	HOCINE Kamel	MCA	Université Relizane
Examineur	FARES Redouane	MCA	Université Relizane
Invité	FAUQUET Carole	MCA	Université aix-Marseille

Abstract:

The purpose of this thesis is to synthesize by depositing manganese oxide as TCO thin films on heated glass substrates. TCO materials exhibit optical transparency and electrical conductivity only in the case where TCO materials are in a nonstoichiometric composition or in a doped one. Pure and doped Mg-Manganese oxides were synthesized by spraying aqueous solution using the spray pyrolysis method. The solution was obtained from manganese chloride ($\text{MnCl}_2, 6\text{H}_2\text{O}$) with 0.1 M onto glass substrates heated at 350°C . Mg-doped Mn-O oxide films were obtained by adding a second aqueous solution prepared by dissolving in distilled water the precursor magnesium chloride hexahydrate ($\text{MgCl}_2, 6\text{H}_2\text{O}$). The Mg-concentrations of 3%, 5%, 7% and 9% were used. The chemical composition of the samples was investigated by X-ray photoelectron spectroscopy (XPS) which showed typical Mn ($2p_{3/2}$), ($2p_{1/2}$) and O (1s) peaks with slight shift attributed to the formation of different chemical states of manganese. Structural and morphological properties were studied by using X-ray diffraction (XRD), scanning electron microscope (SEM) and atomic force microscopy (AFM). XRD analysis revealed a mixture of different manganese oxides phases dominated by tetragonal phase structure of Mn_3O_4 with a preferred (211) growth orientation. SEM images of Manganese oxide films showed rough surfaces composed of uniformly distributed nanograins whose size decreases with the Mg-doping while AFM analysis revealed a textured, rough and porous surface that is improved by the increase of Mg-doping concentration. Optical properties deduced from UV-visible spectroscopy indicated transparent films. The use of Tauc's relationship allowed the determination of the band gap energy. The decrease of the band gap from 2.5 to 1.5 eV with the increase of Mg-doping is attributed to the influence of the greater size of the Mg^{2+} ion in the manganese oxide lattice.

Résumé :

Le but de cette thèse est de synthétiser des couches minces de TCO d'oxyde de manganèse sur des substrats de verre chauffés. Les matériaux TCO présentent une transparence optique et une conductivité électrique uniquement dans le cas où les matériaux TCO sont dans une composition non stœchiométrique ou dopée. L'oxyde de manganèse pur et dopé Mg a été synthétisé en pulvérisant par technique spray pyrolyse une solution aqueuse obtenue à partir de chlorure de manganèse ($\text{MnCl}_2, 6\text{H}_2\text{O}$) à 0,1 M sur des substrats de verre chauffés à 350°C . Des films d'oxyde de Mn-O dopés au Mg ont été obtenus en ajoutant une seconde solution aqueuse préparée en dissolvant dans de l'eau distillée le précurseur de chlorure de magnésium hexahydraté ($\text{MgCl}_2, 6\text{H}_2\text{O}$). Les concentrations de Mg de 3 %, 5 %, 7 % et 9 % ont été utilisées. La composition chimique des échantillons a été étudiée par spectroscopie de photoélectron (XPS) qui montre des pics typiques de Mn ($2p_{3/2}$), ($2p_{1/2}$)

et O (1s) avec un léger shift en énergie attribué à la formation de différents états chimiques de manganèse. Les propriétés structurales et morphologiques ont été étudiées en utilisant la diffraction des rayons X (XRD), le microscope électronique à balayage (SEM) et la microscopie à force atomique (AFM). L'analyse XRD a révélé une mixture de différentes phases d'oxydes de manganèse dominées par la structure de phase tétragonale de Mn_3O_4 avec une orientation préférentielle selon la direction (211). Les images SEM de films d'oxyde de manganèse ont montré des surfaces rugueuses composées de nano grains uniformément répartis dont la taille diminue avec l'augmentation de la concentration du dopage tandis que l'analyse AFM a révélé une surface texturée, rugueuse et poreuse qui s'améliore par l'augmentation du taux de dopage au Mg. Les propriétés optiques déduites de la spectroscopie UV-visible indiquent des films transparents. L'utilisation de la relation de Tauc a permis de déterminer l'énergie de la bande interdite. La diminution de la bande interdite de 2,5 à 1,5 eV avec l'augmentation du dopage au Mg est attribuée à un effet de taille. L'ion Mg^{2+} ayant un rayon ionique plus important que celui de Mn^{2+} distorde le réseau lorsqu'il s'insère dans un site Mn^{2+} et par conséquent il modifie la structure qui se répercute sur la bande interdite.

الملخص:

الهدف من هذه الرسالة هو توليف طبقات رقيقة من مركب أكسيد المنجنيز TCO على قواعد زجاجية مسخنة. تتميز المواد TCO بالشفافية البصرية والتوصيل الكهربائي فقط في حالة تواجدها في تركيبة غير ستوكيومترية. تم توليف أكسيد المنجنيز النقي والمشوب بالمغنيسيوم عن طريق رش محلول مائي محضر من كلوريد المنجنيز $(H_2O_6, MnCl_2)$ بتركيز 0.1 مولار على قواعد زجاجية مسخنة عند درجة حرارة 350 درجة مئوية باستخدام تقنية رش البخاخة البايرووليزية. تم الحصول على أفلام أكسيد المنجنيز المشوبة بالمغنيسيوم من خلال إضافة محلول مائي ثانوي محضر عن طريق ذوبان مادة كلوريد المغنيسيوم السداسي هيدراتي $(MgCl_2, H_2O_6)$ في الماء المقطر. تم استخدام تراكيز مشوبات المغنيسيوم بنسب 7%، 5%، 3% و 9%. تم دراسة التركيب الكيميائي للعينات باستخدام الطيف الكهروني للإلكترونات (XPS) الذي يظهر ذروات مميزة للمنجنيز $(2p_{3/2})$ ؛ $(2p_{1/2})$ والأكسجين (O1s) مع انحراف طفيف في الطاقة يرجع إلى تشكيل حالات كيميائية مختلفة للمنجنيز. تم دراسة الخواص البنيوية والمورفولوجية باستخدام تفريغ الأشعة السينية (XRD) والمجهر الإلكتروني الماسح (SEM) ومجهر القوى الذرية (AFM). توضح تحليل XRD مزيجا من مراحل مختلفة لأكاسيد المنغنيز يهيمن عليها تركيب المرحلة التتراجونية لـ Mn_3O_4 مع توجه تفضيلي وفقاً للاتجاه (211) أظهرت صور SEM لأغشية أكسيد المنغنيز سطوحاً خشنة مكونة من حبيبات نانوية موزعة بشكل متجانس يقل حجمها مع زيادة تركيز المنغنيز. أما تحليل AFM فكشف عن سطح نصف مرئي مموج وخشن ومسامي يتحسن مع زيادة معدل الشوائب بالمنغنيز. تشير الخصائص البصرية المستنتجة من الطيفية UV-visible إلى وجود أفلام شفافة. استخدام علاقة تاوك أتاح تحديد طاقة الفجوة المحظورة. يُعزى تقلص الفجوة المحظورة من 2.5 إلى 1.5 إلكترون فولت مع زيادة شوائب المنغنيز إلى تأثير الحجم. حيث يؤدي أيون المنغنيز Mg^{2+} ذو نصف قطر أيوني أكبر من نصف قطر Mn^{2+} إلى تشوه الشبكة عند إدراجه في موقع Mn^{2+} ، وبالتالي يعدل الهيكل مما ينعكس على الفجوة المحظورة

Acknowledgements

In the beginning, I express my gratitude to the Allah for granting me His boundless benevolence, bravery, strength, and endurance to accomplish this modest work.

Subsequently, I would like to express my deep gratitude to my supervisor Professor Ghamnia Mostefa, who serves as the director of the LSMC Laboratory at Oran 1. I want to acknowledge his invaluable assistance, unwavering support, expert guidance, and constant encouragement. He has consistently been a pillar of strength throughout every aspect of my doctoral thesis, transforming my journey into an unforgettable and enriching experience.

I also express my gratitude to my co-supervisor Professor Bouadi Abed for her valuable support in the successful completion of this thesis.

I extend my heartfelt gratitude to Dr. MESBAH Smain for the honor bestowed upon me through the acceptance of the role as the president of this jury.

I express my gratitude to Dr. FARES Redouane, Dr. HOCINE Kamel, and Dr. NAIM Houcine for kindly agreeing to be part of the committee and for undertaking the evaluation of my research.

I would like to express my heartfelt gratitude to Dr. FAUQUET Carole and Professor Didier Tonneau for their active involvement in my research project and their generous assistance during the experimental phase conducted at the CINaM laboratory at the University of Marseille.

I would like to express my heartfelt gratitude to Pr. Taïbi Hamed and also Pr ZEKRI Nouredine, Laboratoire d'études physique des matériaux, LEPM, USTO.

I also express my gratitude to my Friends Dr. Salah eddine Nacéri, Dr. Menad Abdelkader, Bouchelaghem Azzedine, Bahri Ali, Bettaher Soufiane, Midani mahfoudh.

I express my gratitude to the close person in my heart Sarrah K that supported me and helped me through all the steps of my thesis duration and her mother Ayesha K.

Finally, I would like to express my gratitude to each individual teacher and member of the LSMC laboratory at Oran 1 like: Dr. Benameur Nadir, Dr. Ouhaïbi Abdelhalim, Dr. Hacini Nouredine, Dr. Zakaria Youcefi, Dr. Ali Dahmane, Dr. Bousbahi Khaled, Dr. Hireche Lamia, Dr. Nassima Hamzaoui, Dr. Kerroum Sabrina, Dr. Aroussi Soumia, Dr. Amel Loukil, Malika allali and Kheira, as well as the faculty within the Department of Physics at the universities of Relizane and Oran 1 like Dr. Imam and Dr. Djermouni Mostefa.

Dedication

To my parents,

To my grandmother,

**To my brothers and sisters and everyone who supported
me.**

Contents

Contents	i
Figure list	iii
Introduction.....	A
Bibliography of general introduction.....	E
Chapter I:	1
I.I. Introduction:	2
I.II. The important properties of TCO materials:.....	3
I.III. The interest of thin films in technology devices.....	5
I.III.1. Particle size effects:.....	6
I.III.2. TCO in nanometric scale	7
I.III.3. Some properties of SnO ₂ films	7
I.III.4. Presentation of some properties of ZnO films.....	10
I.IV. Fabrication of TCO in nanometric scale:	12
I.IV.1. Zero-dimensional nanofilms.....	14
I.IV.2. One-dimensional (1D) nanomaterial:	15
I.IV.3. Two-dimensional nanomaterial:	15
I.IV.4. Three-dimensional nanomaterial:	15
I.V. Properties of Nanomaterials:	15
I.VI. Metal oxides nanofilms:	16
I.VI.1. Metal oxides:	16
I.VI.2. Manganese oxide:.....	18
I.VI.3. Trimanganese tetraoxide (Mn ₃ O ₄):	18
Bibliography of chapter I.....	24
Chapter II:	29
II.I. Definition of thin Film:	30
II.I.1. Thin film deposition:.....	30
II.I.2. The importance of thin film deposition and coating:.....	32
II.II. Thin films deposition:.....	32
II.II.1. Thin-film growth:	33
II.II.2. Parameters influencing thin film depositions:	36
II.II.3. Properties of nanofilms:.....	36
II.III. The used synthesis methods in this work	37
II.III.1. Spin coating method.....	37

II.III.2. Spray pyrolysis:.....	38
II.III.3. Advantages of Spray pyrolysis:.....	39
II.III.4. Application Domain of spray pyrolysis technique:.....	39
II.IV. Synthesis of pure and doped MnO.....	40
Bibliography of chapter II.....	41
Chapter III:.....	43
III.I.1. X-Ray Diffraction (XRD):.....	45
III.II. Chemical Composition:.....	50
III.II.1. X-ray Photoelectron Spectroscopy (XPS):.....	50
III.III. Morphology study:.....	52
III.III.1. Scanning Electron Microscopy (SEM):.....	52
III.III.2. Atomic Force Microscopy (AFM).....	55
III.III.3. AFM of laboratory:.....	59
III.IV. Optical Analysis:.....	60
III.IV.1. UV–visible spectroscopy.....	60
III.IV.2. Photo-Luminescence (PL):.....	62
Bibliography of chapter III.....	63
Chapter IV:.....	64
IV.I. Compositional analysis of Mn-O thin films:.....	66
IV.I.1. XPS results.....	66
IV.I.2. Fitting of Oxygen and Mn transitions:.....	70
IV.II. Structural properties of Mn-O thin films:.....	71
IV.II.1. Mn-O films structure.....	71
IV.II.2. Exploitation of XRD spectra.....	74
IV.III. Morphological properties of Mn-O thin films:.....	76
IV.III.1. Scanning Electron Microscopy (SEM).....	76
IV.III.2. Atomic force microscope (AFM) analysis.....	78
IV.IV. Optical properties of Mn-O thin films:.....	81
IV.IV.1. Transmittance of deposited Mn-O films:.....	81
IV.IV.2. Extraction of the band gap of Mn-O:.....	82
Bibliography of chapter IV.....	85
General conclusion.....	88

Figure list

Figure 1 Number of publications per year from the University of Michigan library between 2000 and 2022 [6].	B
Figure 2: Number of patents related to manganese oxide since 1975 [7].	C
Figure 3 : Evolution of the number of articles since the discovery of the properties of TCO materials	2
Figure 4 : Variation in the electrical and optical properties of ATO thin films.	5
Figure 5 : Scheme of the relative size of objects in comparison to the nanoscale size range.	7
Figure 6 : Transmittance and absorbance signals of SnO ₂ films	8
Figure 7 : Variation of the resistivity of SnO ₂ films versus annealing temperature by varying precursor concentration.	9
Figure 8 : Transmittance curve of ZnO films of different thickness	10
Figure 9 : the linear curve of the I(V) measurement of ZnO thin films in ambient light with voltage supply ranging from -5 to 5 V (a) and The resistivity at different film thickness (b)	12
Figure 10 : Nanomaterials synthesis routes.	12
Figure 11 : A diagram depicting how nanomaterials can be classified using various criteria.	14
Figure 12 : Schematic Representation of the atomic percentage of elements found in the Earth's crust.	16
Figure 13 : different forms of manganese oxide	18
Figure 14 : A schematic of Hausmannite crystal structures of Mn ₃ O ₄	20
Figure 15 : schematic of the thin film in size range.	30
Figure 16 : Different techniques of thin films deposition.	31
Figure 17 : (a) Physical methods, (b) chemical methods.	32
Figure 18 : Different phases of thin film growth	34
Figure 19 : The three model of growth issued from the fundamental modes of nucleation. .	35
Figure 20 : schematic representation of different spin coating method.	38
Figure 21 : Schematic experimental system of spray pyrolysis process.	38
Figure 22 : The multi-layer build-up of photovoltaic CIGS Solar cell.	40
Figure 23 : Some characterization techniques adapted to nanomaterials properties study.	44
Figure 24 : Basic schema explaining the diffraction Bragg's law	46
Figure 25 : schematic representation of XRD diffraction.	47

Figure 26 : schematic diagram of an: a) X-ray diffractometer b) full width at half maxima FWHM.	50
Figure 27 : Principal schema of photoelectron emission in XPS.....	50
Figure 28 : Schematic representation of XPS Instrument.....	51
Figure 29 : Typical XPS spectrum of silicon detected from SiO ₂ sample.....	52
Figure 30: Schematic representation of SEM.	54
Figure 31 : Schematic representation of AFM.....	56
Figure 32 : law Contact mode in AFM	58
Figure 33 : Tapping mode in AFM (a): schematic tip interaction, (b): Mode contact from Lennard-Jones potential	59
Figure 34 : AFM Dimension Edge Model of LSMC Laboratory	60
Figure 35 : A simplified Schema of Uv-visible spectroscopy	61
Figure 36 : Uv-visible spectrometer of LSMC laboratory	62
Figure 37 : Survey XPS Spectra of pure and Mg doped Manganese oxide thin films.	67
Figure 38 : XPS shifts of the most intense core levels peaks of oxygen O (1s) of pure and Mg- doped MnO	68
Figure 39 : Shift of Mn2p and Mn 2p _{1/2} transitions highlighting the formation of a non-stoichiometric MnO oxide	69
Figure 40 : XPS spectra of O (1s) transition and its fitting	70
Figure 41 : Curve-fitted XPS spectra of Mn (2p _{1/2}) and Mn (2p _{3/2}) core level.....	71
Figure 42 : X-ray diffraction spectra of pure and Mg-doped Mn-O thin films. (A); (B); (C); (D) ;(E) represent: MnO pur; 3% Mg-doped MnO; 5% Mg-doped MnO; 7% Mg-doped MnO; 9% Mg-doped MnO respectively.	72
Figure 43 : Shift of the XRD peak (211).	74
Figure 44 : SEM images of pure and Mg-doped Mn-O oxide recorded at different magnification	78
Figure 45 : AFM images of 2 μm × 2 μm scan areas of Mg-doped Mn-O oxide (in left) with the profile of the horizontal line of each image (3%: a and b; 5%: c and e; 7%: e and f)(in right).....	79
Figure 46 : AFM images of pure and Mg-doped Manganese oxide recorded in 3 μm × 3 μm scan areas	81
Figure 47 : The transmittance spectra of pure and Mg-doped Manganese oxide.....	82

Figure 48 : The plot of $(\alpha h\nu)^2$ versus $(h\nu)$ according to Tauc's relation..... 83

Introduction

Transparent conducting oxide (TCO) thin films are of interest to many researchers around the world due to their unique two properties which should exhibit both electrical conductivity and optical transparency in the visible region. These two properties open up good prospects in wide applications: in renewable energy as its use in solar cells, in optoelectronic devices such as touch screens, liquid crystal displays, solar cells, light emitting diodes, gas sensors... ZnO and SnO₂ are among the first synthesized TCO materials [1-4].

There is currently a strong demand for new TCO materials because they have been successfully synthesized using a variety of low-cost deposition technique, for example via spray pyrolysis, used in this work to synthesize manganese oxide films. Formerly, manganese oxide was studied extensively for its magnetic properties. For example, in 1948, Louis Néel, discovered the antiferromagnetic phenomenon of manganese oxide [5] which made him the laureate of the Nobel Prize in physics in 1970. Since then, manganese oxide has been a subject of interest in many fields of science. According to the University of Michigan library and as plotted in Figure 3, the number of publications related to manganese oxide has been steadily increasing over the past few decades. In 1975, there were only about a hundred publications related to manganese oxide. Currently, in 2022, the number of publications on manganese oxide is increased to up 500 demonstrating the growing interest in this material.

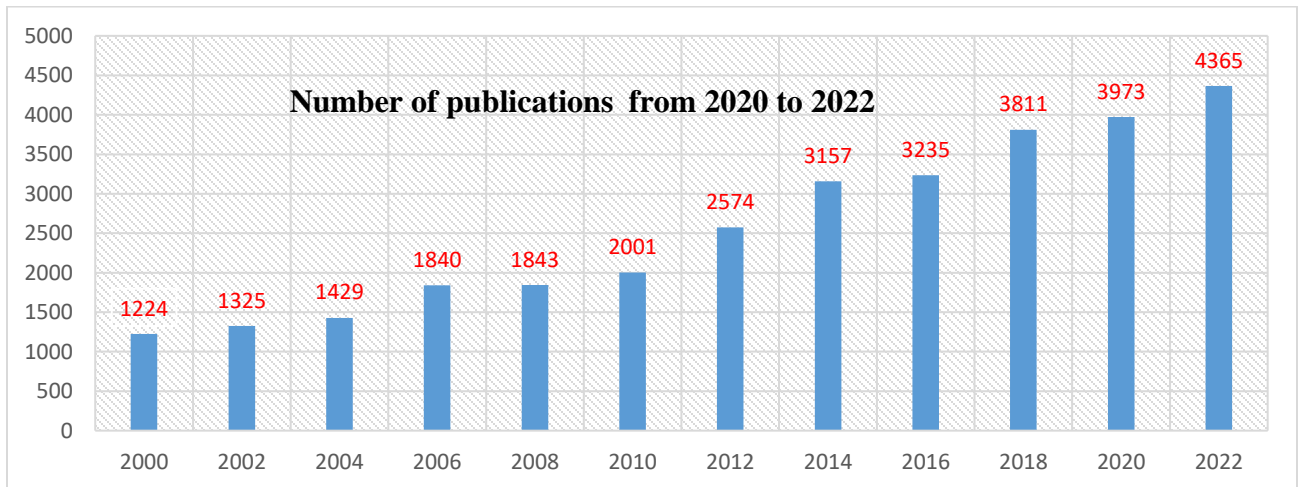


Figure 1 Number of publications per year from the University of Michigan library between 2000 and 2022 [6].

Manganese oxide has also been the subject of many patents. According to the Lens.org database, there have been 5717 patent applications related to manganese oxide since 1975. The majority of these patents are related to catalysts and batteries which suggest that manganese

oxide has practical applications in various industries. In Figure 4, we show the evolution of patent number during time.

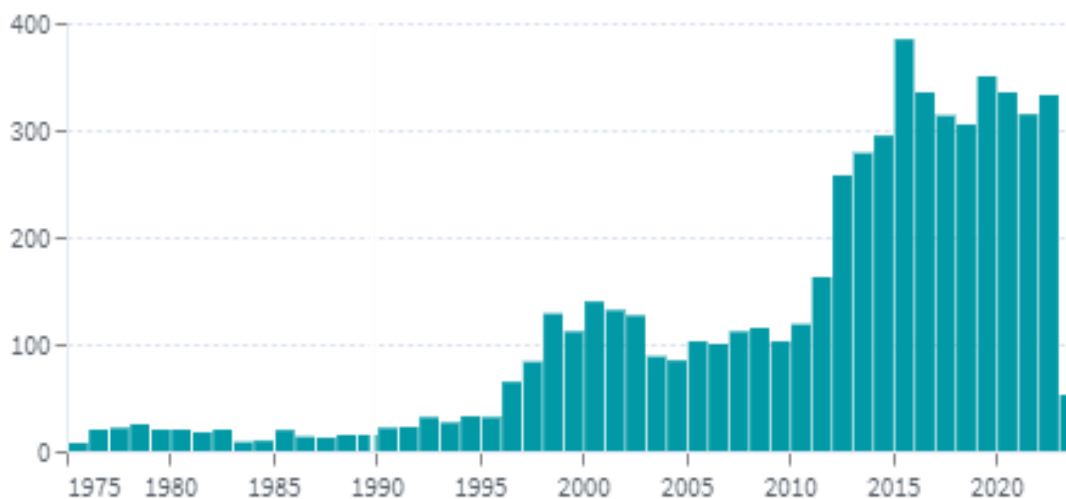


Figure 2: Number of patents related to manganese oxide since 1975 [7]

In the nanoscience domain, manganese oxide has been studied extensively for its catalytic properties [8-10]. Nanoparticles of manganese oxide have been shown to be effective catalysts for various chemical reactions, including the oxidation of alcohols and the reduction of nitrate in water. Manganese oxide nanoparticles have also been used in biomedical imaging, as they exhibit strong magnetic resonance imaging (MRI) contrast. One of the challenges in using manganese oxide nanoparticles is the control of their sizes and their shapes. Various synthesis methods have been developed to produce nanoparticles of manganese oxide with specific sizes and shapes.

It is in this context that we are interested in the synthesis of transparent conducting Manganese oxide films because at first and as discussed just above, manganese oxide is a well-known material in the field of nanoscience. Secondly, it is a naturally occurring mineral, commonly found in nature. The optical and electrical properties of Manganese oxide films offer a wide area of applications, including catalysis, energy storage, water treatment, gas sensors and many others. Because of that and of its interesting physical and chemical

General Introduction

properties, Manganese oxide may be a very good TCO synthesized thin film. As spray pyrolysis is an easy method to implement, and to have the ability to prepare large-scale thin films, we have used it herein to synthesize pure and Mg-doped manganese oxide films.

Good and important results were obtained; they are presented in this manuscript which is composed of four chapters; chapter 1 is a general review on TCO materials taking manganese oxide as example. Chapter 2 is devoted to the various deposition methods used in thin films science with a specific focus on spray pyrolysis process is used in this work, in chapter 3, we explore the different characterization techniques that we have used for Manganese oxide analysis, the fourth chapter is dedicated to the experimental results, to their analysis and interpretation;

Bibliography of general introduction

1. Rogers, D., et al. *ZnO thin films and nanostructures for emerging optoelectronic applications*. in *Optoelectronic Integrated Circuits XII*. 2010. SPIE.
2. Voggu, V.R., et al., *Flexible CuInSe₂ nanocrystal solar cells on paper*. ACS Energy Letters, 2017. **2**(3): p. 574-581.
3. Dalapati, G.K., et al., *Tin oxide for optoelectronic, photovoltaic and energy storage devices: a review*. Journal of Materials Chemistry A, 2021. **9**(31): p. 16621-16684.
4. Lee, W.-J., et al., *Transparent perovskite barium stannate with high electron mobility and thermal stability*. Annual Review of Materials Research, 2017. **47**: p. 391-423.
5. Néel, L., *Magnetic properties of ferrites: ferrimagnetism and antiferromagnetism*. Physical Chemical & Earth Sciences, 1984(31): p. 18.
6. Library, U.o.M. *University of Michigan Library*. [cited 2023; Available from: <https://search.lib.umich.edu/articles>].
7. lens.org. *Patent Search Results of manganese oxide*. [cited 2023; Available from: [https://www.lens.org/lens/search/patent/table?q=title:\(manganese%20oxide\)](https://www.lens.org/lens/search/patent/table?q=title:(manganese%20oxide))].
8. Lima, F.H., M.L. Calegari, and E.A. Ticianelli, *Investigations of the catalytic properties of manganese oxides for the oxygen reduction reaction in alkaline media*. Journal of Electroanalytical Chemistry, 2006. **590**(2): p. 152-160.
9. Tang, Q., et al., *Structure and catalytic properties of K-doped manganese oxide supported on alumina*. Journal of Molecular Catalysis A: Chemical, 2009. **306**(1-2): p. 48-53.
10. Adil, S., et al., *Nano silver-doped manganese oxide as catalyst for oxidation of benzyl alcohol and its derivatives: synthesis, characterisation, thermal study and evaluation of catalytic properties*. Oxidation Communications, 2013. **36**(3): p. 778-791.

Chapter I:
A general review on
Transparent Conducting
Oxides materials in thin and
nanometric films: the case of
Mn₃O₄

I.I. Introduction:

The discovery of TCO materials dates back to the work of Badeker [1] in 1904 when he observed an oxidation of Cadmium (Cd) metal thin films deposited in a glow discharge chamber. After oxidation, Cd-O films became transparent in conserving their electrical conductivity [2]. Since this discovery, the list of TCO material expanded to other oxide materials as ZnO, TiO₂, SnO₂, In₂O₃... in pure or doped form. Currently, the properties of TCO materials remain a subject of intense research around the world, the number of publications published per year shown in figure 3 testifies the interest of these materials.

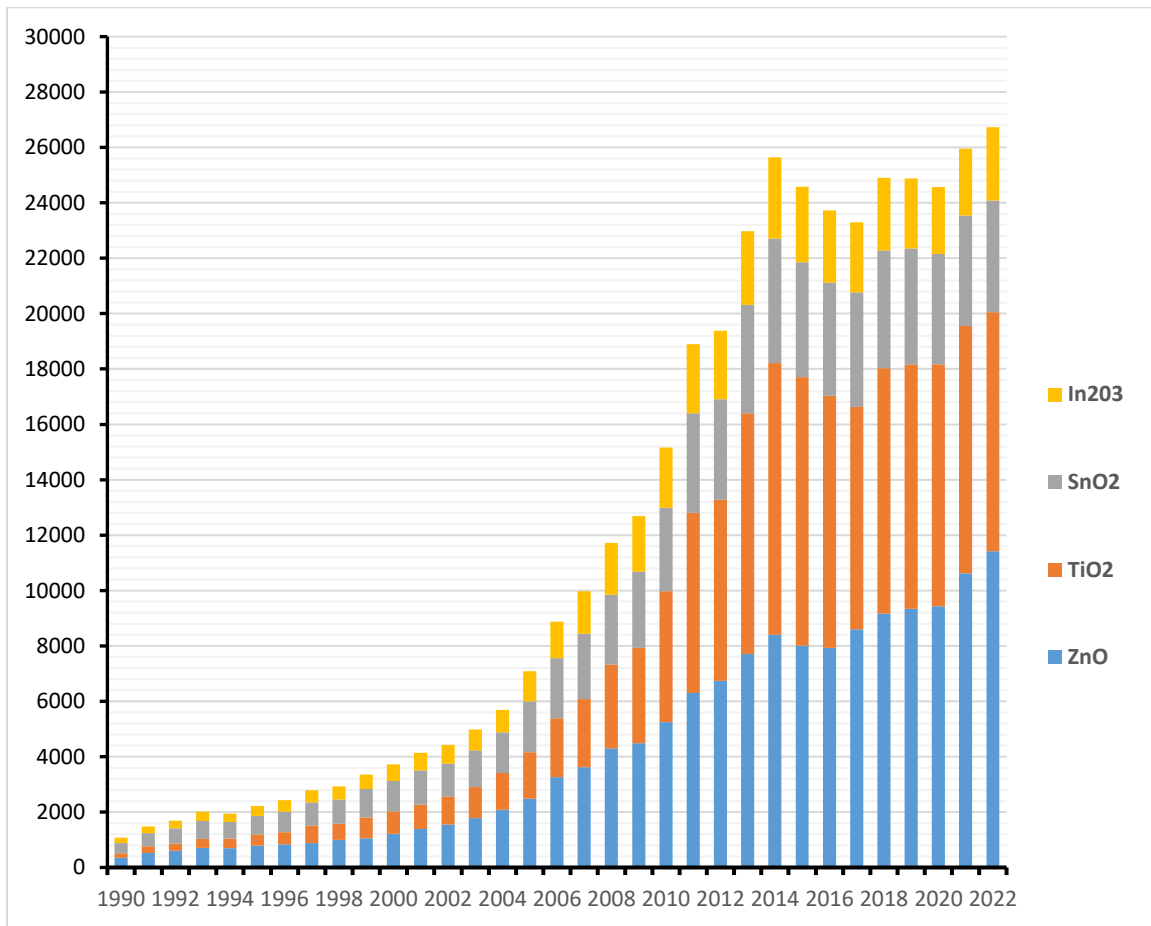


Figure 3 : Evolution of the number of articles since the discovery of the properties [3] of TCO materials

Due to its interesting properties, TCO (Transparent Conductive Oxide) materials have found diverse applications in various fields. Some of the key areas where TCO materials are extensively utilized include:

- **Optoelectronic Devices:** TCO materials are commonly used as transparent electrodes in optoelectronic devices such as touch panels, OLED (Organic Light-Emitting Diode) displays, and photodetectors. These materials provide high electrical conductivity while maintaining transparency, allowing for efficient light transmission [4].
- **Solar Cells:** TCO materials is used in solar cell technology. They are commonly used as transparent electrodes in both traditional silicon-based solar cells and emerging technologies like perovskite solar cells and thin-film solar cells.
- **Electrochromic Devices:** TCO coatings are employed in electrochromic devices, which can change their color or transparency in response to an electrical stimulus. These devices have applications in smart windows, rearview mirrors, and displays, offering dynamic control of light transmission [5, 6].
- **Gas Sensors:** TCO thin films can be used as gas sensing devices. By monitoring changes in the electrical properties of TCO materials when exposed to specific gases, these sensors can detect and quantify the presence of harmful gases in industrial or environmental settings [7, 8].

I.II. The important properties of TCO materials:

Transparent Conducting Oxides (TCO) are materials that possess at the same time the property of high electrical conductivity and high optical transparency in the UV-visible domain at the same time. This possibility is closely related to the structure and to the bandgap of TCO. The conductivity is highly dependent on the carrier concentration and mobility which are related by the following relation:

$$\sigma = n \cdot q \cdot \mu \quad (1)$$

Where n is the density of electron in the conduction band, q is the charge of the electron and μ is the mobility of charge carriers. It can therefore be seen that the conductivity is increased by the presence of defects linked to oxygen vacancies or by controlled doping with appropriate external impurities. The electrical resistivity (ρ) is expressed in $\Omega \cdot \text{cm}$, as below:

$$\rho = \frac{1}{\sigma} \quad \text{Eq. 1}$$

ρ is low and is ranging between 10^{-3} and 10^{-4} Ω .cm.

The mobility of free electrons in the conduction band is given by:

$$\mu = \frac{e \cdot \tau}{m^*} \quad \text{Eq. 2}$$

where τ is the mean time between collisions, and m^* is the effective electron mass. However, as m^* and τ are negatively correlated, the magnitude of μ is limited. D

Since the band gaps of these materials lie in the ultraviolet wavelength [200-400 nm] region where $E_g > 3$ eV, they hardly absorb visible light and appear to be transparent with a high optical transparency (transmittance $>80\%$).

The optical properties of TCO materials as transmission T, reflection R, and absorption A, are determined by its refraction index n, extinction coefficient k, bandgap E_g . In the case of TCO films where the stoichiometry is not respected, T, R and A are often depending on the thickness uniformity, and on the surface roughness. T, R, and A are also depending on the chemical composition and solid structure of the material.

T, R and A are of interest when attention is being focused on a thin film because they actually determine how the film behaves to incident beam of light as X-rays for example.

The law of conservation of energy implies that the sum of parameters T, R and A is equal to as:

$$T + R + A = 1 \quad \text{Eq. 3}$$

These optical properties of thin films are not constants because they are influenced by various factors such as the substrate temperature, film thickness, crystallinity, nature and amount of dopants. These factors also affect greatly the electrical properties of thin films [9].

The Figure 4 shows some examples of the conductivity and transmittance of ATO thin films annealed in nitrogen and Forming gas atmospheres a) 325°C and b) 425°C [10].

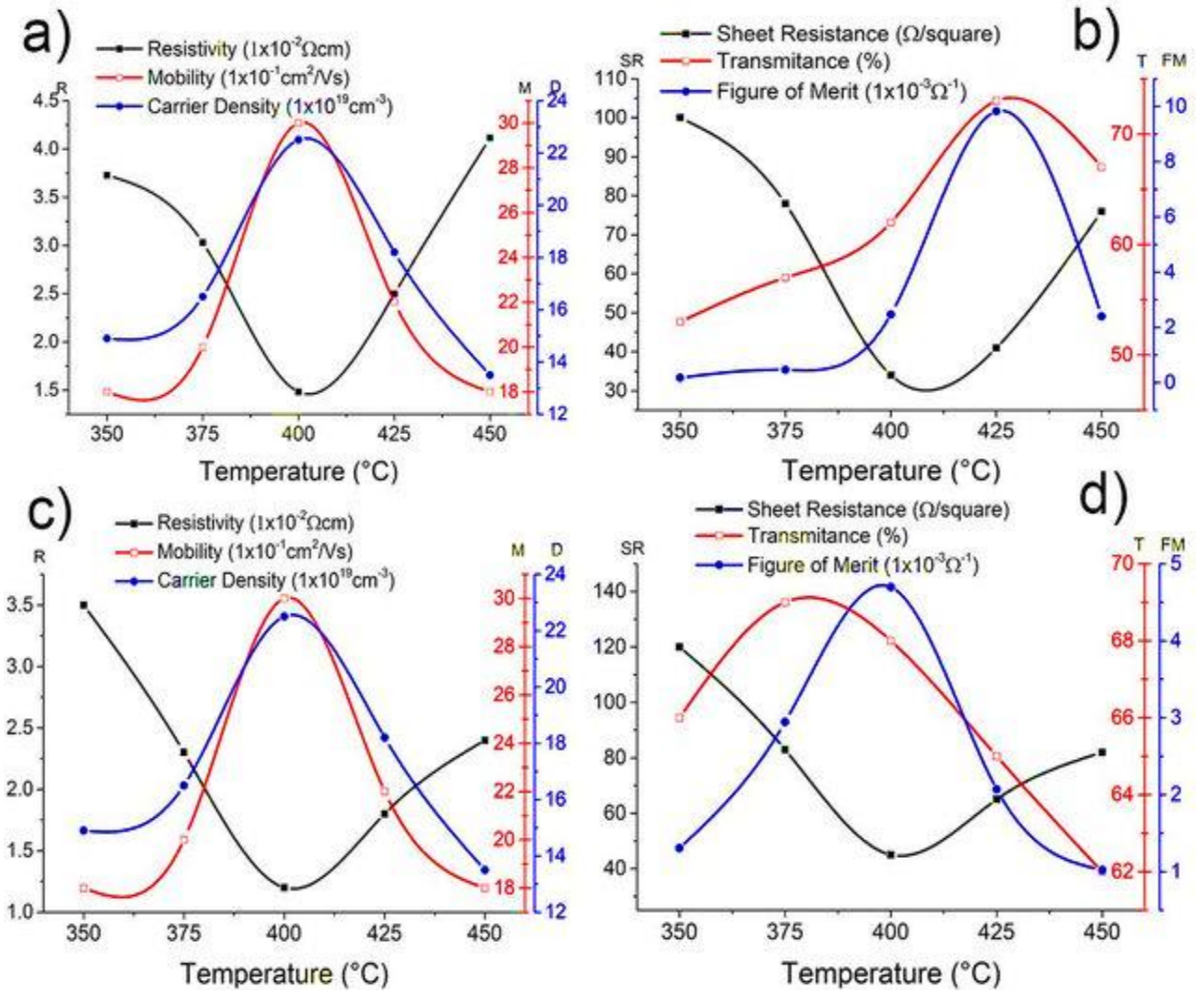


Figure 4 : Variation in the electrical and optical properties of ATO thin films [10]

I.III. The interest of thin films in technology devices

The chemical and physical properties of thin films are different of those of bulk. Thin film studies have directly or indirectly advanced many new areas of research in solid state physics and chemistry which are based on phenomena uniquely characteristic of the thickness, geometry and structure of the film. Modern technology requires thin films for different applications fields of electronics, optics, space science, aircrafts, and other industries.

The requirements for TCO are good electrical conductivity and high transparency in the visible domain. They get better when the TCOs are made in nanoscale layers ranging from 1 to 100 nm.

Their physical properties are different from those they have when they are micro or macroscopic in size. When we reduce the size of a material, we increase its surface area by freeing more space to interact with other atoms and/or molecules. When we reduce the size to the nanometric scale, the exposed surface area increases and this favors the greater interaction between nearby atoms and molecules, giving rise to various interactions as attractions and repulsions that cause surface, electronic and quantum effects affecting greatly physical properties as the optical, electric or magnetic.

For example, the mechanical properties of carbon nanotubes are greater than those of steel where the tensile strength of carbon nanotubes is approximately 100 times greater than that of steel. The discovery of nanomaterials opened up a new domain to science and technology called now nanoscience and nanotechnology.

Nanotechnology has become an interdisciplinary field in physics and materials sciences. It refers to those areas of engineering and science where phenomena occur at small dimensions in the range of nanometers < 100 nm. This field is used in materials design, characterization, production, and other applications.

I.III.1. Particle size effects:

The main difference between bulk material and nanomaterial is the size difference and properties related to particle size. The decrease in the particle size will change the properties of nanomaterials more than in the bulk material. These changes make the nanomaterials into a different class of materials with new applications. The Figure 5 shows some examples of the size of some objects.

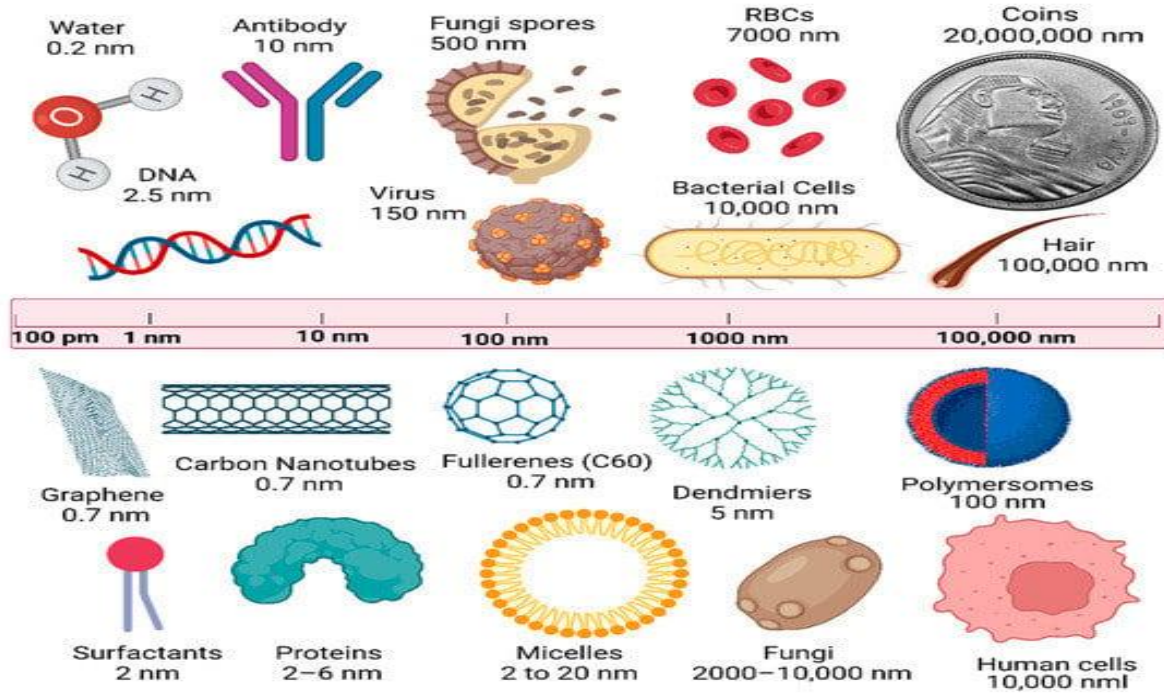


Figure 5 : Scheme of the relative size of objects in comparison to the nanoscale size range. [11]

I.III.2. TCO in nanometric scale

As we reminded, transparent conductive oxides have an important which combines two properties: high optical transmission at visible wavelengths and electrical conductivity close to that of metals.

Both of these properties improve when TCO is synthesized in nanoscale layers. Thanks to these two properties, transparent conductive oxides (TCO) are used in a wide range of applications such as transparent contacts for solar cells, optoelectronic devices, flat panel displays, liquid crystal devices, touch screens... SnO₂, In₂O₃ and ZnO are among the first studied TCO materials. We present some properties of these three materials.

I.III.3. Some properties of SnO₂ films

I.III.3.1. Transparent properties

Tin oxide (SnO₂) is tetragonal structure with oxygen-deficient *n*-type having wide band gap (3.6 eV) [12-14] and it is considered as a very suitable material due to its attractive properties like low resistivity, optical transmittance and piezoelectric behavior [12, 15, 16].

SnO₂ is also a more suitable candidate for some applications such as solar cell window layer and optoelectronic devices. From the following Figure 6 (a) and 4(b), pure and Mg doped SnO₂ films show a higher absorption coefficient in the UV region than in the visible light region.

The absorbance curve which possesses three regions has its first region between the ranges of 800 nm to 370 nm where there is fluctuation in the absorbance [17, 18].

SnO₂ films transmittance is influenced by the bandgap energy, film crystallinity, surface morphology and concentration doping. For the case of the system Mg-SnO₂, the transmittance yield is between 50 and 75%. The doping improves the crystallinity of SnO₂ films and reduces the transmittance.

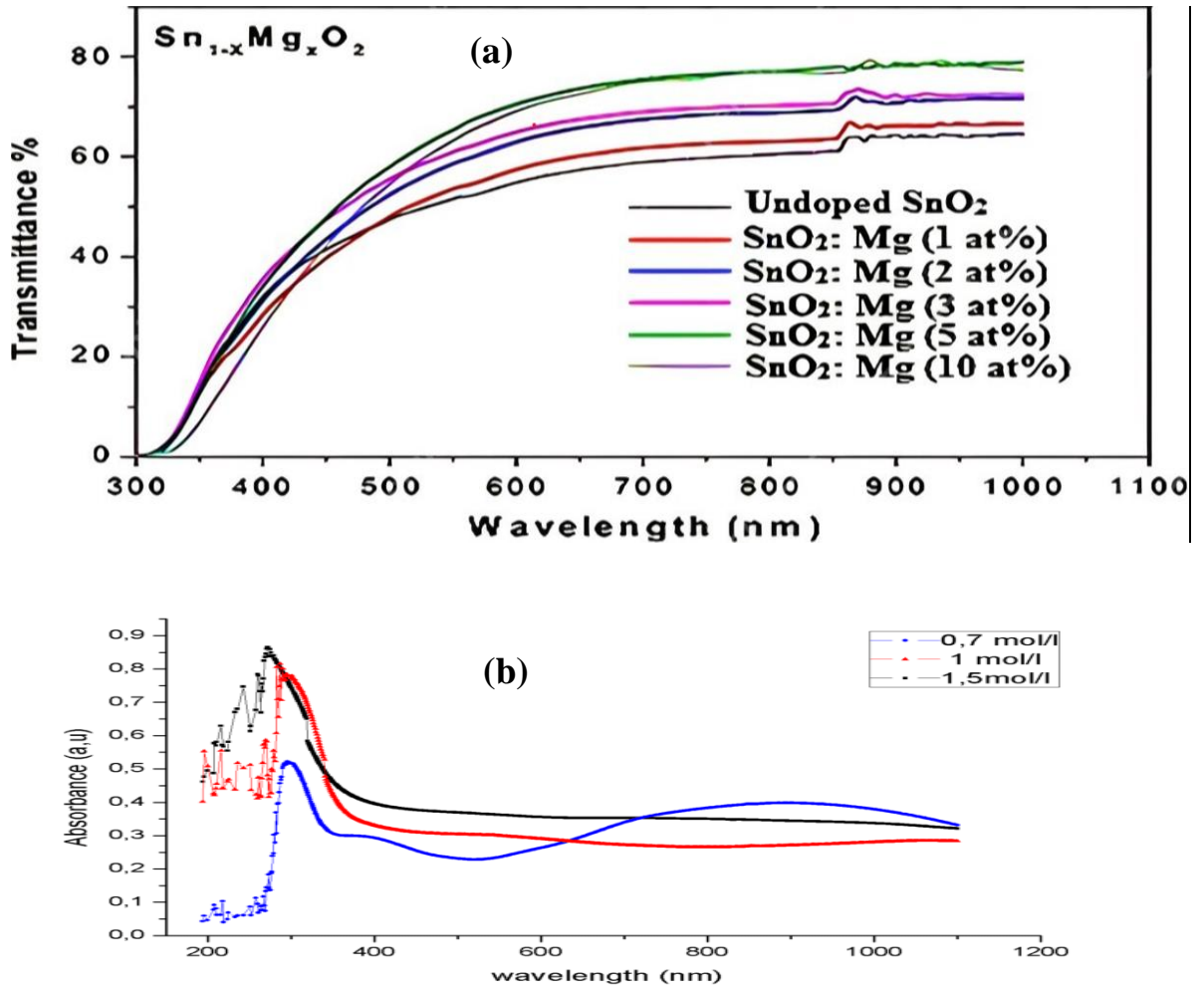


Figure 6 : Transmittance and absorbance signals of SnO₂ films

[19, 20]

I.III.3.2. Electrical properties

SnO₂ films possess good electrical properties equivalent to semiconducting behavior. The conductivity of SnO₂ films is most suitable for preparation of gas sensors.

The activation energy is one of the important parameters to understand the gas sensing mechanism. The activation energy can be calculated with the help of electrical resistivity measurements.

In Figure 7, we show the plot of ln(σ) versus (1000/T) for SnO₂ thin films. From this figure we can observe a decrease in conductivity with increasing temperature for SnO₂ thin films. This decrease confirms the semiconducting behavior of SnO₂.

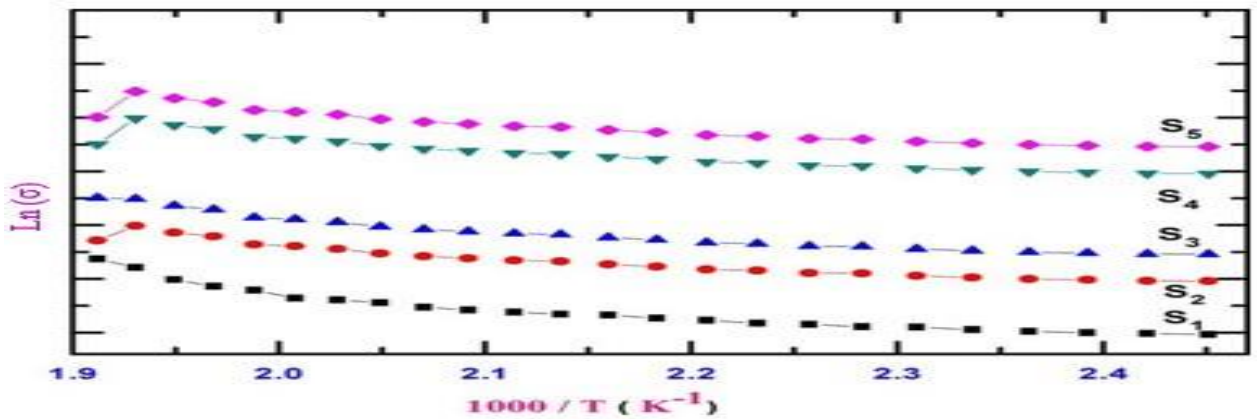


Figure 7 : Variation of the resistivity of SnO₂ films versus annealing temperature [21] by varying precursor concentration.

The activation energies can be determined by using Arrhenius equation:

$$\sigma(T) = \sigma_0 e^{-\frac{E_a}{k_B T}} \quad \text{Eq. 4}$$

Where σ is the conductivity of SnO₂ thin film at temperature T, σ₀: conductivity at temperature T₀, E_a: activation energy and k_B: is Boltzmann's constant.

The activation energy obtained from the plot of σ(T) is found to be 2.9, 2.6, 2.4, 2.2 and 2.0 meV for SnO₂ samples S1, S2...S5 (the different concentrations 0.1 M, 0.2 M, 0.3 M,

0.4 M and 0.5 M)

I.III.4. Presentation of some properties of ZnO films

ZnO is an example of wide band gap semiconductors which have been used in optoelectronic devices [22-24] for the realization of light emitting diodes and laser diodes. ZnO is mostly chosen for its better excitonic energy of 60 meV at room temperature [25-27]) properties compared to GaN. Besides that, ZnO is characterized by a high transparency in the visible region and by high conductive properties. Because of these interesting properties, ZnO is widely used in photovoltaic devices, and sensors.

The conductive property of ZnO is due to the presence of defects in its crystalline structure such as oxygen deficiency or zinc excess in interstitial sites. We present in this chapter some properties of ZnO as the transparency and the conductive properties.

I.III.4.1. The transparency properties of ZnO films

Optical transmittance of ZnO films with different thickness is plotted in a wavelength range of 300 to 1000 nm as shown in Fig. 6. The films are highly transparent in the visible range (above 90%). The transparence is depending on the thickness of the films.

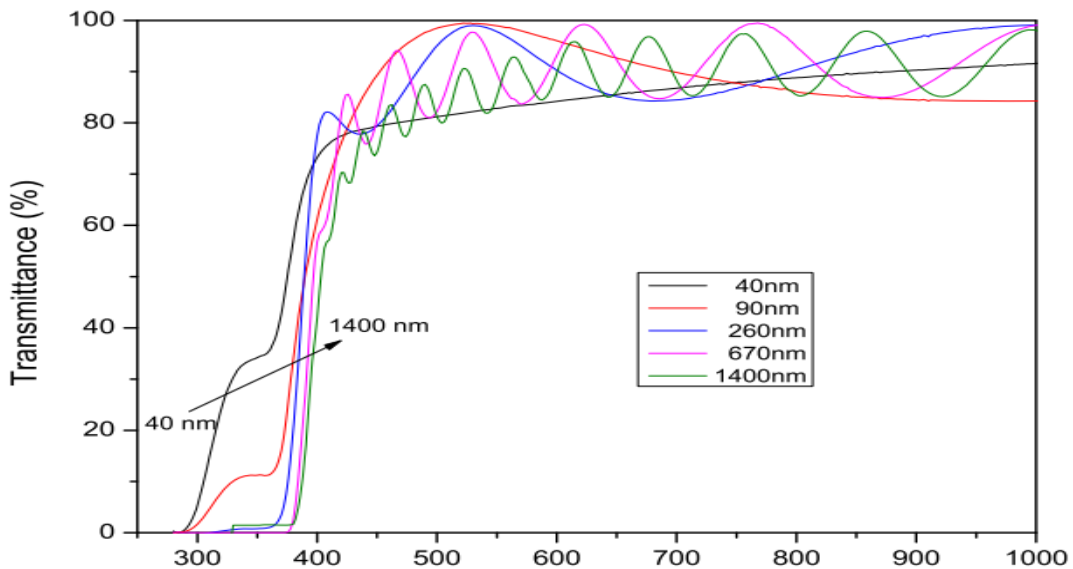


Figure 8 : Transmittance curve of ZnO films of different thickness [28]

I.III.4.2. Electrical properties of ZnO films

Figure 9 (a) shows the linear curve of the I(V) measurement of ZnO thin films in ambient light with voltage supply ranging from -5 to 5 V [29].

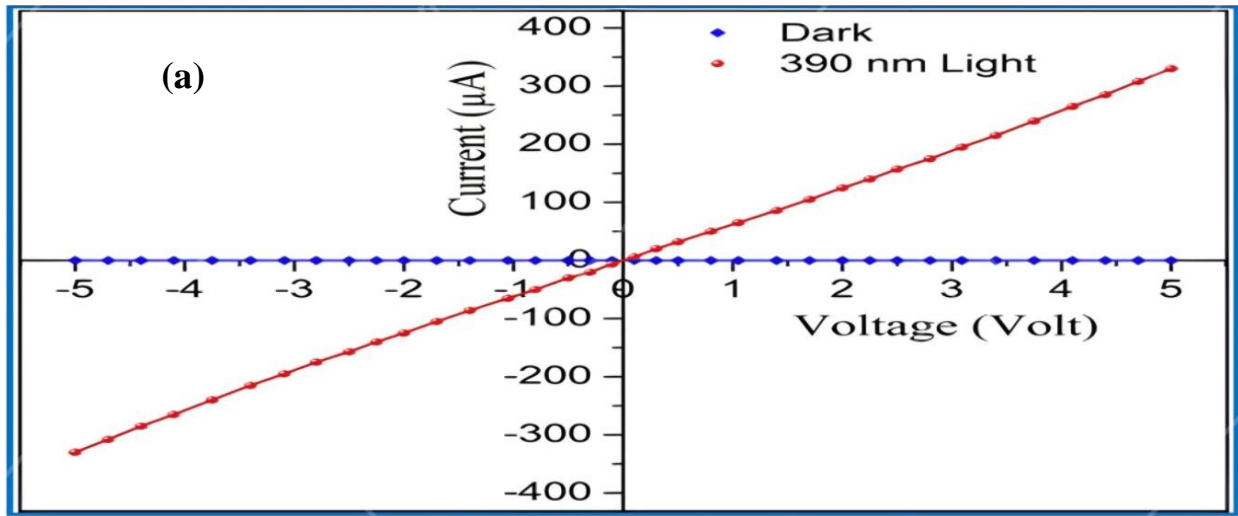
The resistivity is deduced from I (V) graph, and is plotted in Fig. 7(b) as a function of ZnO film thickness.

The resistivity decreases as the thickness increases from 14.2 nm to 42.7 nm, with a minimum value observed at $1.39 \times 10^{-2} \Omega \cdot \text{cm}$.

However, when the thickness was increased above 42.7 nm, the resistivity of the films also increased to a maximum value of $13.6 \times 10^{-2} \Omega \cdot \text{cm}$. Two behaviors can be observed: for films below 50 nm thickness, the resistivity decreased, and for the films with thickness above 50 nm, the resistivity increased with the film thickness.

This can be explained by the effect of the thickness which improves the crystallinity of ZnO and increases the ZnO crystallites. This later contributes to the increase of electron mobility and therefore it decreases the resistivity [30].

The plot of the Figure 9(b) is related to the current–voltage I (V) and is obtained by applying voltages between - 5 V and + 5 V. We can observe that under light, the linear relationship of the characteristics reveals that the contact has ohmic character.



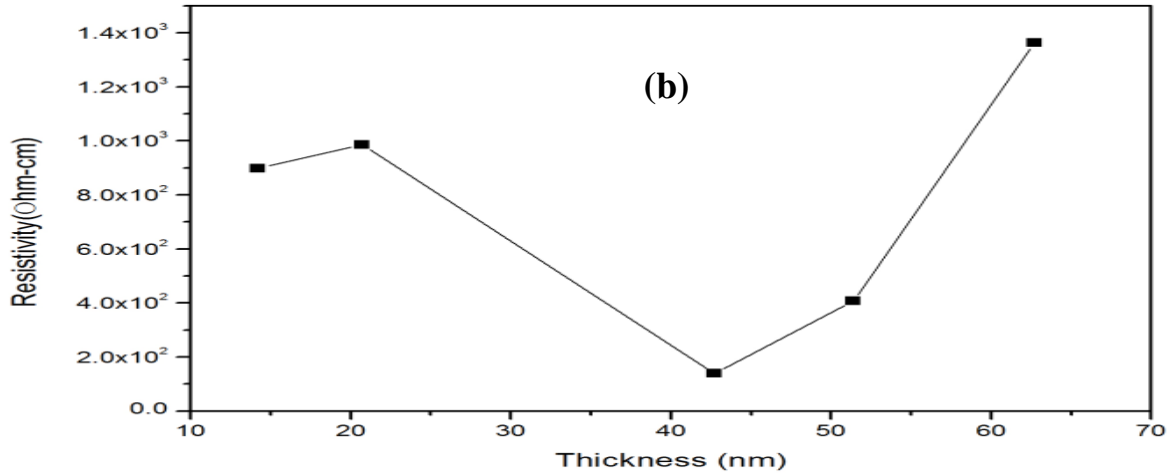


Figure 9 : the linear curve of the I(V) measurement of ZnO thin films in ambient light with voltage supply ranging from -5 to 5 V (a) and The resistivity at different film thickness (b) [29, 31]

I.IV. Fabrication of TCO in nanometric scale:

Materials science and engineering emphasizes the significance of nanoparticle preparation, which can be accomplished through diverse methods: physical, chemical and biological. The Figure 10 shows some of these methods.

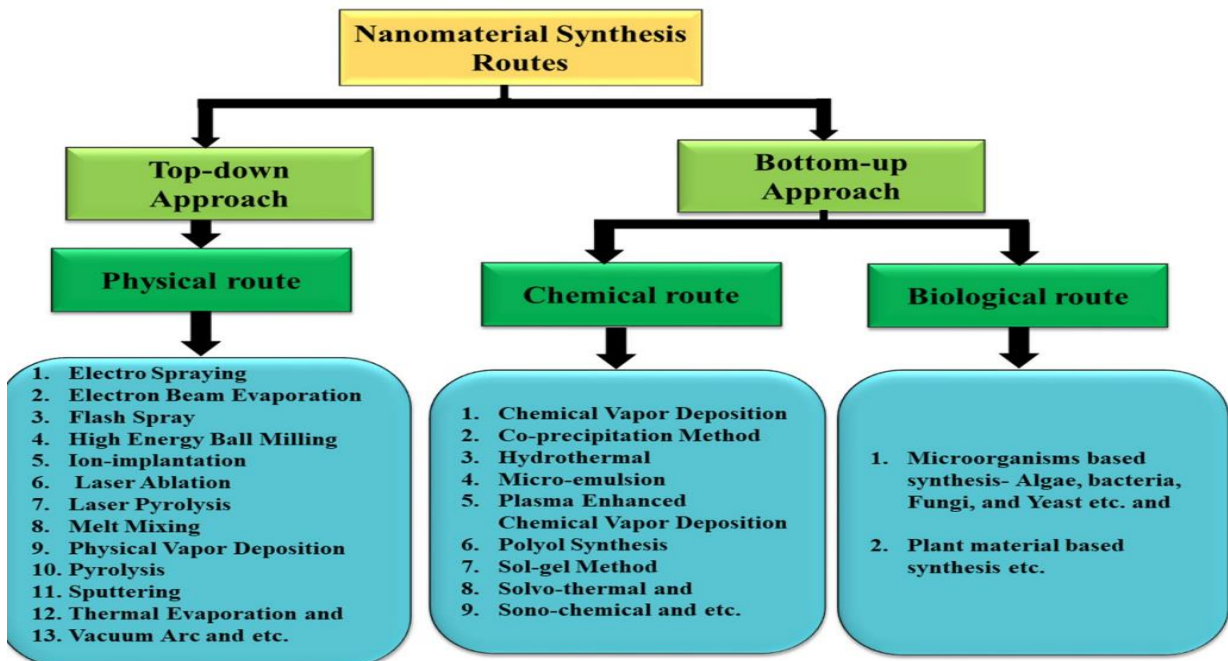


Figure 10 : Nanomaterials synthesis routes.

[32]

While certain techniques are innovative, others have been in practice for an extended period. The four key procedures for generating novel nanoparticles are gaseous phase, vapor deposition, wet chemistry, and grinding.

Several of these processes bear resemblance to established chemical production methodologies:

- i) The gas phase technique employs a variety of heating methods, including resistance heating and high-frequency induction heating, in addition to chemical reactions and sputtering processes.
- ii) The liquid phase technique involves precipitation, hydrolysis, spray, and solvent-based methods.
- iii) The solid phase technique employs thermal decomposition, solid-state reactions, spark discharge, stripping, and milling, resulting in very fine particles that can be either amorphous or crystalline in nature.

The small size of nanoparticles makes any surface coating highly influential in the overall properties of the particles [33]. The nanofilms obtained by one of these methods can be classified as follows:

The nanofilms are structured; their atoms are arranged in an organized manner in one, two, or three dimensions, forming distinct patterns at the nanometer scale.

These patterns can take the shape of nano-spheres, nanotubes, nanorods, nanowires, and nano-belts.

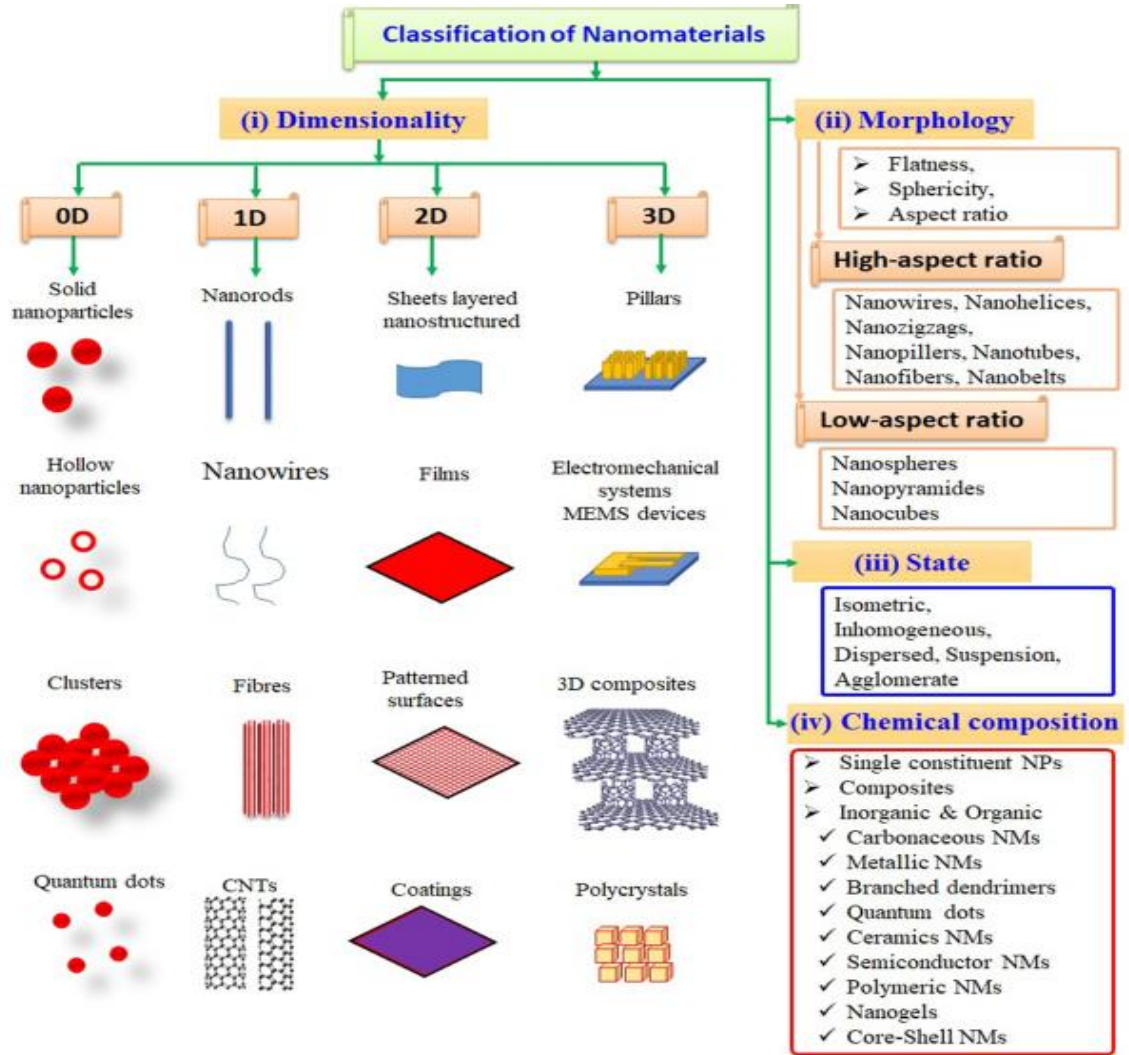


Figure 11 : A diagram depicting how nanomaterials can be classified using various criteria. [34]

Nanostructured films can be classified into four categories based on their dimensional complexity, namely zero-dimensional, one-dimensional, two-dimensional, and three-dimensional nanostructures [34]:

I.IV.1. Zero-dimensional nanofilms

In the context of 0D, measurements of all dimensions are limited to one hundred nanometers or less, encompassing single crystal, polycrystalline, and amorphous particles of varying shapes and forms.

This can be further classified into two categories: nanocrystals, where the nanoparticles are single crystalline, and quantum dots, where the nanoparticles' size is small enough to observe quantum effects.

I.IV.2. One-dimensional (1D) nanomaterial:

In the 1D, the whiskers and nanorods have a smaller length-to-thickness ratio than fibers, nanowires, and nanostructures with large aspect ratios called nanofibers. It is also called: whiskers, fibres or fibrils, nanowires, and nanorods.

I.IV.3. Two-dimensional nanomaterial:

The important nanostructure of 2D that scientists studied for almost a century is thin films [3].

I.IV.4. Three-dimensional nanomaterial:

"3D Nano systems" can refer to objects that are micrometers or millimeters in size but contain nanometric features, like confinement spaces or periodic arrangements of nano-sized units. Despite being larger than the nano scale, these systems exhibit unique molecular and bulk properties due to their nanoscale components (1-100 nm). For example, 3D nanocrystals are created from the organization of 0D spheres, and 1D rods or 2D plates can form impressive superstructures such as those found in box-shaped graphene or mesostructured platinum films [35].

At the nanoscale, a nanocrystalline with crystalline order and small size can be classified as a Quantum Well, Quantum Wire, or Quantum Dot, depending on its number of dimensions. Nanocrystalline are sometimes referred to as Quantum Dots [33].

I.V. Properties of Nanomaterials:

Nanomaterials exhibit unique physical properties distinct from bulk materials due to their size range between atomic and standard dimensions. The specific properties of nanomaterials can be attributed to various factors, such as a significant fraction of surface atoms, spatial confinement, reduced imperfections, and high surface energy.

The presence of these properties can lead to a variety of outcomes such as alterations in melting point, lattice dimensions, strength, optical characteristics, electrical conductance, magnetic behavior, and self-cleansing. These properties depend highly on the nanomaterials' size, shape, and extent of aggregation, which allows tuning their properties.

I.VI. Metal oxides nanofilms:

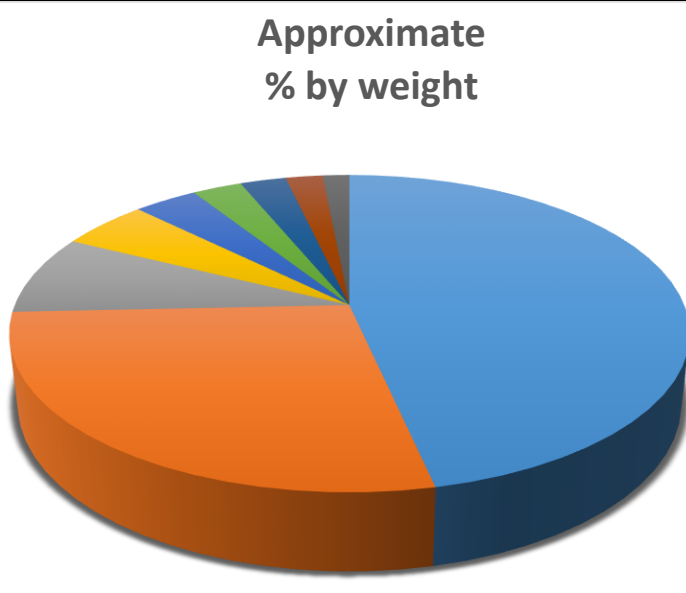
Metal oxide nanomaterials are crucial in several fields, including chemistry, physics, and materials science in nanotechnology because of their distinct properties at the nanoscale. Various oxide compounds can be formed from metal elements, resulting in a broad range of structural geometries that may possess metallic, semiconductor, or insulator traits.

These oxides are employed in the production of microelectronic circuits, piezoelectric devices, sensors, and catalysts in technology [36].

I.VI.1. Metal oxides:

The Earth's crust contains different chemical elements. In Table 1 and Figure 12, oxygen and metals are the most abundant elements

Element	Approximate % by weight
Oxygen	46.6
Silicon	27.7
Aluminum	8.1
Iron	5.0
Calcium	3.6
Sodium	2.8
Potassium	2.6
Magnesium	2.1
All others	1.5



Approximate % by weight

- Oxygen
- Silicon
- Aluminum
- Iron
- Calcium
- Sodium
- Potassium
- Magnesium
- All others

Figure 12 : Schematic Representation of the atomic percentage of elements found in the Earth's crust.

[37]

Table 1 : the quantities of various elements present in the Earth's crust.

Nanotechnology used this advantage of existence in the Earth's crust to create more exciting materials with unique properties and use them in daily human life. One of the most significant examples is phones, processors, sensors, T.V...

Metal: any class of substances characterized by ductility, high electrical, high thermal conductivity, and high light reflectivity [38].

I.VI.1.1. Oxide:

It contains at least one oxygen atom and another atom in its chemical formula. Metal oxide: A metal oxide is a type of crystalline solid that consists of a metal cation and an oxide anion. It has the ability to react with water and form bases, and with acids to form salts. Binary oxygen compounds come in three distinct types:

- (1) Oxide ions with a charge of O^{2-} are present in oxides.
- (2) Peroxide ions with a charge of O_2^{2-} are found in peroxides.
- (3) Superoxide ions with a charge of O^- are present in superoxide [39].

I.VI.1.2. Manganese:

Manganese (Mn) that we use in this work through its oxide is discovered in 1774 by Johann Gahn [40]. Mn is an element with atomic number 25. It is the tenth most plentiful element found in the Earth's crust, with an average content of about 0.1% in crustal rocks.

It is a heavy metal, second only to iron, and has a brittle nature. Manganese is prone to oxidation and difficult to melt. When in its pure form, it is highly reactive, burns in oxygen when in a powder form, dissolves in dilute acids, and reacts with water.

I.VI.1.2.1. Applications of manganese

Manganese is a crucial element in the production of iron and steel due to its ability to enhance their properties, including strength, toughness, and resistance to corrosion. It is a key component in various widely used aluminum alloys and low-cost stainless-steel formulations, making it an integral part of the manufacturing industry.

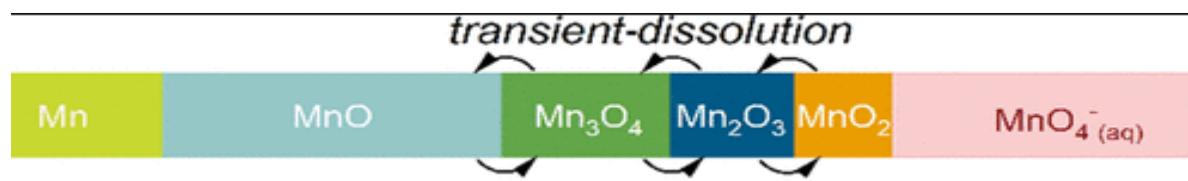
Apart from its use in the production of iron and steel, manganese is also used in other fields. It is used as a catalyst in the production of ceramics and as a micronutrient in fertilizers, it is used to decolorize glass, specifically violet-colored glass, due to its ability to remove impurities.

I.VI.1.2.2. The use of manganese in the environment:

Manganese oxide has been utilized by civilizations of the past for hundreds of years as a clarifying agent for glass and pigments. Mn metal is available in the Earth's crust and is among the most abundant metals found in soil. With an annual mining output of over five million tons, there is no doubt about its commercial importance.

I.VI.2. Manganese oxide:

Manganese is a transition metal with a versatile range of stable stoichiometric oxides. Mn oxide is present four forms: MnO₂, Mn₂O₃, Mn₃O₄, and MnO.



[41]

Figure 13 : different forms of manganese oxide

These oxides exhibit various oxidation states ranging from +4 to +2, making manganese oxide a versatile transition metal oxide. The specific oxide formed by manganese will depend on factors such as the oxygen pressure, temperature, and the ratio of manganese to oxygen during the reaction. The importance of these manganese oxides lies in their applications in a wide range of fields, including catalysis, batteries, supercapacitors, and environmental remediation [42].

I.VI.3. Trimanganese tetraoxide (Mn₃O₄):

Trimanganese tetraoxide, also known as Manganese (II, III), is a chemical compound that occurs naturally as the mineral Hausmannite.

It is a p-type semiconductor material with a wide direct band gap of 2.3 eV. This unique electronic property makes it an attractive material for various applications, including catalysis, energy storage, and electronic devices.

The crystal structure of Mn₃O₄ is similar to Hausmannite, with an attenuated gap composed of states with HOMO (highest occupied molecular orbital) predominantly having O²⁻ 2p character and LUMO (lowest unoccupied molecular orbital) with antibonding states of tetrahedral Mn³⁺.

This configuration results in a unique electronic and magnetic behavior, making it useful in spintronics and magneto-optical devices [43].

I.VI.3.1. Mn₃O₄: Trimanganese tetraoxide structural properties:

Manganese oxide is a group of chemical compounds that contain manganese and oxygen. Among them, Trimanganese tetraoxide, known under the formula Mn₃O₄, is a stable phase with a typical spinel structure.

This structure consists of a face-centered cubic lattice in which the oxygen ions occupy the corners and the Mn³⁺ and Mn²⁺ ions occupy the tetrahedral and octahedral sites, respectively. In this tetragonal form, Mn³⁺ ions occupy the octahedral sites, and Mn²⁺ ions occupy the tetrahedral sites.

The stable temperature for this transformation depends on the preparation method and the purity of the Mn₃O₄ sample.

Hausmannite is an important mineral in geological systems, and Mn₃O₄ is widely used in various applications, including catalysis, energy storage, and magnetic materials. Understanding the crystal structure and the properties of Mn₃O₄ in different forms is crucial for designing and optimizing its applications [44].

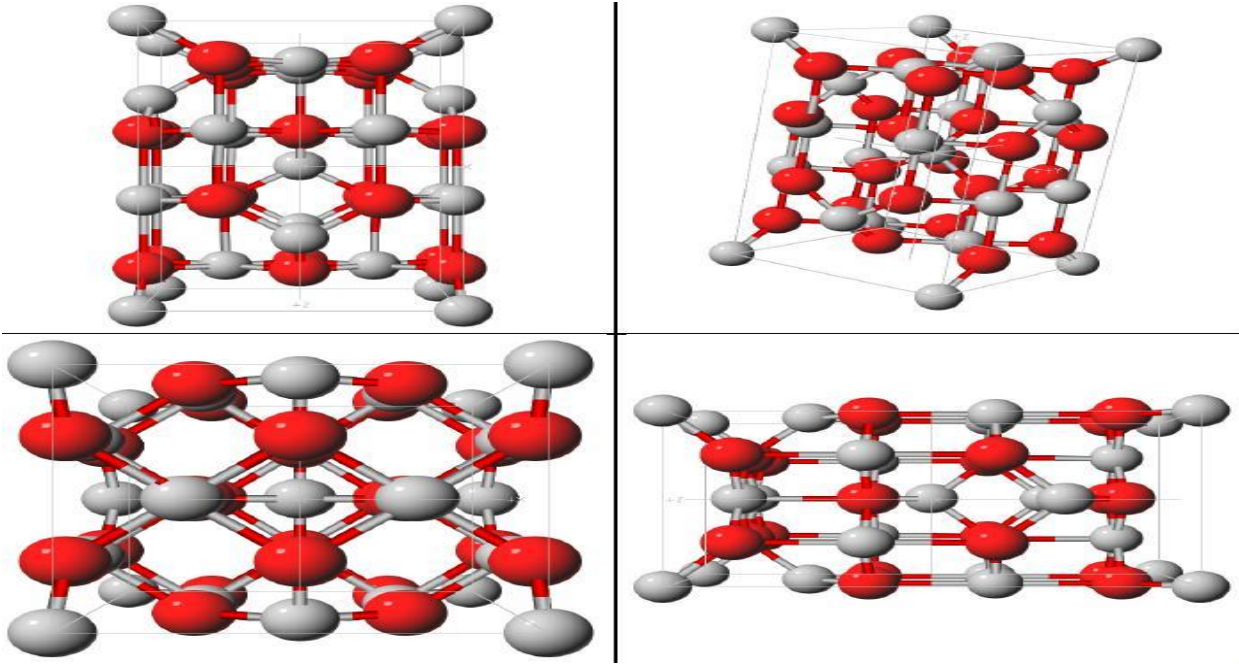


Figure 14 : A schematic of Hausmannite crystal structures of Mn₃O₄ [45]

So usually, Mn₃O₄ crystallizes in Hausmannite crystal structures where lattice constants a and b are 5.7621 Å and c is 9.4696 Å with all the angles equal to 90° according to the JCPDS card No. 024-0734.

I.VI.3.2. Electrical properties of Mn₃O₄:

The electronic structure of the Manganese, manganese ions, and oxygen is as follows:

Mn electronic structure: $1s^2 2s^2 2p^6 3s^2 3p^6 3d^5 4s^2$

Mn²⁺ electronic structure: $1s^2 2s^2 2p^6 3s^2 3p^6 3d^5$

Mn³⁺ electronic structure: $1s^2 2s^2 2p^6 3s^2 3p^6 3d^4$

O: $1s^2 2s^2 2p^4$

The investigation of electrical transport phenomena in Mn₃O₄ has gained significant attention in recent years, primarily due to its potential applications in various fields such as supercapacitors, lithium-ion batteries, sensors, and catalysts.

Mn₃O₄ is considered a highly promising material for such applications due to its low-cost production, excellent environmental compatibility, high natural abundance, and impressive

specific capacity. Supercapacitors, which are energy storage devices, require materials with high capacitance, good cycle stability, and high-power density. Mn₃O₄ has demonstrated remarkable electrochemical properties and could serve as a viable electrode material in supercapacitors.

Additionally, Mn₃O₄ is a potential candidate for use as an anode material in lithium-ion batteries due to its high theoretical capacity, low volume expansion, and good cycling performance. Mn₃O₄ also exhibits excellent sensing properties, making it suitable for use in gas and humidity sensors.

Moreover, it can serve as a highly active catalyst in various reactions, such as oxygen evolution, water splitting, and CO oxidation. Overall, the study of electrical transport phenomena in Mn₃O₄ has immense potential for applications in diverse fields due to its unique combination of low cost, environmental compatibility, abundance, and excellent electrochemical and catalytic properties [46].

The electrical conductivity of Mn₃O₄ is between 10⁻⁷ and 10⁻⁸ Ω/cm [47, 48], which is a poor conductor. Mn₃O₄ is paramagnetic in a nature at room temperature but becomes ferromagnetic below the temperature range of 41-43 K [49]. Also, it can give an excellent performance in supercapacitor electrodes. That is why new research tries to improve the efficiency of electrodes differently, like doping with other chemical species in nanoparticles [50].

I.VI.3.3. Optical properties of Mn₃O₄:

Mn₃O₄ is a material that has shown great potential as an electrochromic material for anodic coloration. One of the key reasons for this is its ability to undergo a reversible color change, transitioning from a colored state (typically brown) to a bleached state (usually yellow), making it a desirable material for use in applications such as smart windows and displays. The electrochromic behavior of Mn₃O₄ makes it an attractive candidate for use in energy-saving applications, where it can be used to regulate the amount of light and heat entering a space.

In many studies, the optical transmittance of Mn₃O₄ decreases with the increase in the annealing temperature. The index refraction of Mn₃O₄ is 2.49 [51]. The bandgap optic of Trimanganese tetraoxide is around 2.7 eV at 400°C and 2.4 at 800°C [52].

I.VI.3.4. Magnetic properties:

Mn₃O₄ is a compound that shows great promise in the field of magnetism due to its exceptional magnetic properties. This material is made up of three manganese cations and four oxygen anions, which form a unique crystal structure that exhibits remarkable magnetic behavior.

Specifically, Mn₃O₄ is a ferrimagnetic material, which means that it has two magnetic sublattices that align in opposite directions, resulting in a net magnetic moment. This property makes it an excellent candidate for use in a wide range of applications, including magnetic storage devices, spintronics, and biomedical imaging. One of the key advantages of Mn₃O₄ is that its magnetic properties are highly tunable, allowing researchers to optimize its performance for specific applications. This means that the material can be engineered to have the desired magnetic characteristics, such as strength, stability, and directionality.

Additionally, Mn₃O₄ has been found to exhibit excellent thermal stability and resistance to corrosion, which are important considerations for many practical applications. Due to its unique properties, Mn₃O₄ has become an important focus of research in the field of magnetism. Scientists are exploring new ways to synthesize and modify this material, with the aim of improving its performance and expanding its range of applications.

Some potential future applications of Mn₃O₄ include the development of high-density magnetic storage devices, more efficient spin-based electronics, and advanced biomedical imaging techniques. Overall, Mn₃O₄ represents a significant advancement in the field of magnetism, with exciting potential for future technological innovations. As research in this area continues, it is likely that we will discover new and innovative ways to harness the remarkable magnetic properties of this material.

I.VI.3.5. Catalyst properties:

Mn₃O₄ is a compound composed of three manganese and four oxygen atoms that has attracted considerable attention from researchers due to its exceptional physical and chemical properties. Its ability to catalyze various reactions, including oxidation reactions, oxygen reduction reactions, and water splitting, make it a highly promising material in the field of catalyst properties. One of the unique advantages of Mn₃O₄ is its remarkable stability and durability, which make it an excellent catalyst for long-term use. Its crystal structure allows for efficient electron transfer and catalytic activity, further contributing to its stability and durability. The most of researchers continue to explore the full potential of Mn₃O₄ in the field of catalysts.

They aim to develop new and efficient catalytic systems for various industrial and environmental applications. Some of the promising areas of research include using Mn₃O₄ as a catalyst for energy conversion and storage, such as in fuel cells and batteries, and environmental remediation, such as in removing pollutants from wastewater [49].

I.VI.3.6. Optoelectronic properties:

Mn₃O₄, also known as manganese oxide, is a versatile material that has garnered significant attention in the field of optoelectronics due to its promising properties. This compound exhibits unique electrical and optical characteristics, including high conductivity, excellent light absorption, and strong magnetism.

These features make it a potential candidate for a range of applications, such as solar cells, sensors, and spintronics. Additionally, Mn₃O₄ is relatively abundant and cost-effective, making it an attractive alternative to other materials that are more expensive or difficult to obtain. Overall, the exceptional optoelectronic properties of Mn₃O₄ make it a promising material for future technological advancements.

I.VI.3.7. Its use in Wastewater treatment:

Wastewater is a crucial process used to purify water rejected by manufactures. Thereby removing harmful contaminants and pollutants to make it safe for reintroduction into the environment. For example, Mn₃O₄ has a strong oxidation capability and quickly reacts with phenol. After the reaction, a part of Mn²⁺ ions with low valence leaches into the acid solution. Therefore, it can remove phenol in water treatment without a particular operation parameter [53].

Mn₃O₄ is used in our work to study the photo catalytical properties. Mn₃O₄ particles act on the methylene Blue (MB) and decolorize under un-irradiation. Important results are obtained qualifying it for use in wastewater treatment.

Bibliography of chapter I

1. Badeker, K., *Concerning the electricity conductivity and the thermoelectric energy of several heavy metal bonds*. Annalen der Physik, 1907. **22**: p. 749.
2. Habis, C., J. Zaraket, and M. Aillerie. *Transparent Conductive Oxides. Part I. General Review of Structural, Electrical and Optical Properties of TCOs Related to the Growth Techniques, Materials and Dopants*. in *Defect and Diffusion Forum*. 2022. Trans Tech Publ.
3. Library, U.o.M. *University of Michigan Library*. [cited 2023; Available from: <https://search.lib.umich.edu/articles>].
4. Hofmann, A.I., E. Cloutet, and G. Hadziioannou, *Materials for transparent electrodes: from metal oxides to organic alternatives*. Advanced Electronic Materials, 2018. **4**(10): p. 1700412.
5. Shchegolkov, A.V., et al., *A brief overview of electrochromic materials and related devices: A nanostructured materials perspective*. Nanomaterials, 2021. **11**(9): p. 2376.
6. Pande, G.K., et al., *Influence of ITO electrode on the electrochromic performance outcomes of viologen-functionalized polyhedral oligomeric silsesquioxanes*. RSC advances, 2022. **12**(20): p. 12746-12752.
7. Araújo, E.P.d., et al., *Improving Hazardous Gas Detection Behavior with Palladium Decorated SnO₂ Nanobelts Networks*. Sensors, 2023. **23**(10): p. 4783.
8. Castañeda, L., *Solid State Gas Sensor Devices*. Biomedical Journal of Scientific & Technical Research, 2022. **40**(5): p. 32098-32118.
9. Manoj, P., et al., *Preparation and characterization of indium-doped tin oxide thin films*. Ceramics International, 2007. **33**(2): p. 273-278.
10. Flores-Hernández, B., et al., *Optoelectronic properties of antimony doped tin oxide thin films obtained by spray pyrolysis*. Materials Research, 2022. **25**.
11. Barhoum, A., et al., *Review on natural, incidental, bioinspired, and engineered nanomaterials: history, definitions, classifications, synthesis, properties, market, toxicities, risks, and regulations*. Nanomaterials, 2022. **12**(2): p. 177.
12. Kiruthiga, G., et al., *SnO₂: Investigation of optical, structural, and electrical properties of transparent conductive oxide thin films prepared by nebulized spray*

- pyrolysis for photovoltaic applications*. Inorganic Chemistry Communications, 2022: p. 109968.
13. Filippatos, P.-P., et al., *Temperature and Ambient Band Structure Changes in SnO₂ for the Optimization of Hydrogen Response*. Inorganics, 2023. **11**(3): p. 96.
 14. Sabri, N.S., et al., *Effect of Mn doping on structural and optical properties of SnO₂ nanoparticles prepared by mechanochemical processing*. Physics Procedia, 2012. **25**: p. 233-239.
 15. Azam, A., et al., *Effect of Mn doping on the structural and optical properties of SnO₂ nanoparticles*. Journal of Alloys and Compounds, 2012. **523**: p. 83-87.
 16. Kumar, K.D.A., et al., *Nd³⁺ Doping effect on the optical and electrical properties of SnO₂ thin films prepared by nebulizer spray pyrolysis for opto-electronic application*. Materials Research Bulletin, 2018. **101**: p. 264-271.
 17. Renuga, R., et al., *Effect of dopant concentration Mn in SnO₂ nanoparticles on photocatalytic, magnetic and optical properties*. Digest Journal of Nanomaterials & Biostructures (DJNB), 2022. **17**(4).
 18. Nwanna, E.C., P.E. Imoisili, and T.-C. Jen, *Synthesis and characterization of SnO₂ thin films using metalorganic precursors*. Journal of King Saud University-Science, 2022. **34**(5): p. 102123.
 19. Rouchdi, M., et al., *Synthesis and magnetic properties of Mg doped SnO₂ thin films: experimental and Ab-initio study*. Optical and Quantum Electronics, 2017. **49**: p. 1-13.
 20. Belhamri, S. and N.-E. Hamdadou. *Concentration influence on structural and optical properties of SnO₂ thin films synthesized by the spin coating technique*. in *Journal of Physics: Conference Series*. 2016. IOP Publishing.
 21. Kamble, D.L., et al., *Characterization and NO₂ gas sensing properties of spray pyrolyzed SnO₂ thin films*. Journal of analytical and applied pyrolysis, 2017. **127**: p. 38-46.
 22. Nandi, S., S. Kumar, and A. Misra, *Zinc oxide heterostructures: Advances in devices from self-powered photodetectors to self-charging supercapacitors*. Materials Advances, 2021. **2**(21): p. 6768-6799.
 23. Mofor, A.C., *Fabrication and Characterisation of Device Quality ZnO Nanostructures*. 2007: Cuvillier Verlag.

24. Abdul Hamid, H., *Fabrication, Structural And Electrical Characteristics Of Zinc Oxide (Zno) Thin Films By Direct Current Sputtering*. 2009, Universiti Sains Malaysia.
25. Zhang, Z., et al., *Exciton-polariton light-emitting diode based on a ZnO microwire*. Optics Express, 2017. **25**(15): p. 17375-17381.
26. Chen, S., et al., *UV electroluminescence emissions from high-quality ZnO/ZnMgO multiple quantum well active layer light-emitting diodes*. RSC advances, 2021. **11**(62): p. 38949-38955.
27. Shafiqul, I.M., T. Yoshida, and Y. Fujita, *p-ZnO/n-ZnMgO Nanoparticle-Based Heterojunction UV Light-Emitting Diodes*. Materials, 2022. **15**(23): p. 8348.
28. Rahmane, S. and M.A. Djouadi, *Optoelectronic properties of ZnO thin films grown by radio frequency magnetron sputtering*. Journal of Materials Science: Materials in Electronics, 2020. **31**(20): p. 17872-17878.
29. Shariffudin, S., et al., *Effect of film thickness on structural, electrical, and optical properties of sol-gel deposited layer-by-layer ZnO nanoparticles*. Transactions on electrical and electronic materials, 2012. **13**(2): p. 102-105.
30. Bouderbala, M., et al., *Thickness dependence of structural, electrical and optical behaviour of undoped ZnO thin films*. Physica B: Condensed Matter, 2008. **403**(18): p. 3326-3330.
31. Abdulrahman, A.F., *The effect of different substrate-inclined angles on the characteristic properties of ZnO nanorods for UV photodetectors applications*. Journal of Materials Science: Materials in Electronics, 2020. **31**(17): p. 14357-14374.
32. Kumar, L., et al., *Nanomaterials for remediation of contaminants: a review*. Environmental Chemistry Letters, 2021. **19**: p. 3139-3163.
33. Kumar, N. and S. Kumbhat, *Essentials in Nanoscience and Nanotechnology*. 2016: Wiley.
34. Saleh, T.A., *Nanomaterials: Classification, properties, and environmental toxicities*. Environmental Technology & Innovation, 2020. **20**: p. 101067.
35. Ahmed, S. and W. Ali, *Green Nanomaterials: Processing, Properties, and Applications*. 2020: Springer Nature Singapore.
36. Puolamaa, M., *The appropriateness of existing methodologies to assess the potential risks associated with engineered and adventitious produc*. 2006, SCENIHR.

37. Nave, R. *Abundances of the Elements in the Earth's Crust*. [cited 2023; Available from: <http://hyperphysics.phy-astr.gsu.edu/hbase/Tables/elabund.html>].
38. Britannica, T.E.o.E., *metal*, in *Encyclopedia Britannica*. 2021.
39. Zumdahl, S.S., *oxide*, in *Encyclopedia Britannica*. 2018.
40. Cunat, P.-J., *Alloying elements in stainless steel and other chromium-containing alloys*. Euro Inox, 2004. **2004**: p. 1-24.
41. Speck, F.D., et al., *Mechanisms of manganese oxide electrocatalysts degradation during oxygen reduction and oxygen evolution reactions*. The Journal of Physical Chemistry C, 2019. **123**(41): p. 25267-25277.
42. Post, J.E., *Manganese oxide minerals: Crystal structures and economic and environmental significance*. Proceedings of the National Academy of Sciences, 1999. **96**(7): p. 3447-3454.
43. Ghosh, S.K., *Diversity in the family of manganese oxides at the nanoscale: from fundamentals to applications*. ACS omega, 2020. **5**(40): p. 25493-25504.
44. Gorbenko, O.Y., et al., *The structure and properties of Mn₃O₄ thin films grown by MOCVD*. Solid State Communications, 2002. **124**(1-2): p. 15-20.
45. Rodriguez, J.A. and F.G. Marcos, *Metal oxide nanoparticles*. 2007: p. 4.
46. Said, L.B., et al., *Electric Conduction Mechanisms Study within Zr Doped Mn₃O₄ Hausmannite Thin Films through an Oxidation Process in Air*. Applied Microscopy, 2017. **47**(3): p. 131-147.
47. Bose, V.C. and V. Biju, *Defect dependent optical, electrical and magnetic properties of nanostructured Mn₃O₄*. Superlattices and Microstructures, 2015. **88**: p. 287-298.
48. Wang, H., et al., *Mn₃O₄-graphene hybrid as a high-capacity anode material for lithium ion batteries*. Journal of the American Chemical Society, 2010. **132**(40): p. 13978-13980.
49. Sayyed, S.G., et al., *Paving the way towards Mn₃O₄ based energy storage systems*. ES Energy & Environment, 2021. **14**: p. 3-21.
50. Tamizh Selvi, K., et al., *Structural, electrical and magnetic properties of Mn₃O₄/MgO nanocomposite*. Journal of Materials Science: Materials in Electronics, 2017. **28**(3): p. 2317-2324.
51. Jain, A., et al., *Commentary: The Materials Project: A materials genome approach to accelerating materials innovation*. APL materials, 2013. **1**(1): p. 011002.

Chapter I: A general review on Transparent Conducting Oxides materials in thin and nanometric films. An example of Mn₂O₃

52. Pishdadian, S. and A.S. Ghaleno, *Influences of annealing temperature on the optical and structural properties of manganese oxide thin film by Zn doping from sol-gel technique*. Acta Phys. Pol. A, 2013. **123**: p. 471.
53. Tuser, C. *What is...wastewater treatment?* 2021; Available from: <https://www.wwdmag.com/wastewater-treatment/wastewater-treatment/article/10938537/what-is-wastewater-treatment>.

Chapter II:

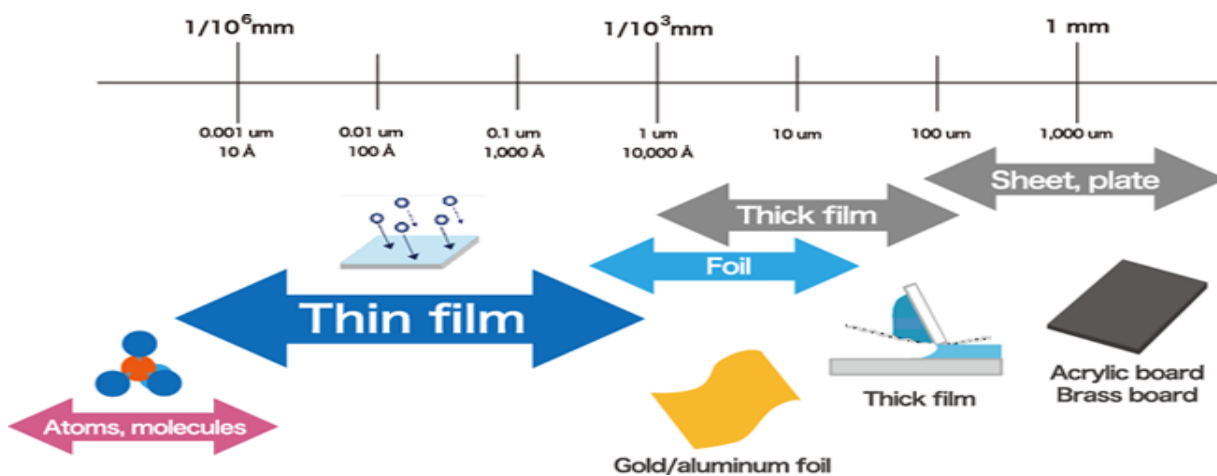
Methods of growth and synthesis of TCO films

Chapter II: Methods of growth and synthesis of TCO films

Thin film deposition for material growth or synthesis is a modern technique born from research and is used extensively in the industry. The development of vacuum technology changed the thin film deposition world and made it famous in our modern society. Growth in vacuum improves greatly the formation of thin films of semiconductors used in microelectronic devices.

II.I. Definition of thin Film:

Thin films are a superposition of many layers of material that typically have a thickness ranging from a few nanometers to a few micrometers. As shown in figure 15, unlike three-dimensional objects, thin films are restricted to two dimensions, with a thickness of less than 1 micrometer.



[1]

Figure 15 : schematic of the thin film in size range

These materials are constructed from minuscule building blocks, such as atoms, ions, or molecules, and their unique properties are a result of their nanoscale grain structure [2].

II.I.1. Thin film deposition:

Thin film deposition can be achieved through various techniques requiring vacuum and high-power conditions. It can be done through physical methods as thermal evaporation, sputtering, PLD, MBE... or by chemical methods as CVD, MOCVD, Spray pyrolysis, spin coating... Figure 16 and Figure 17 resumes these different techniques of thin films formation.

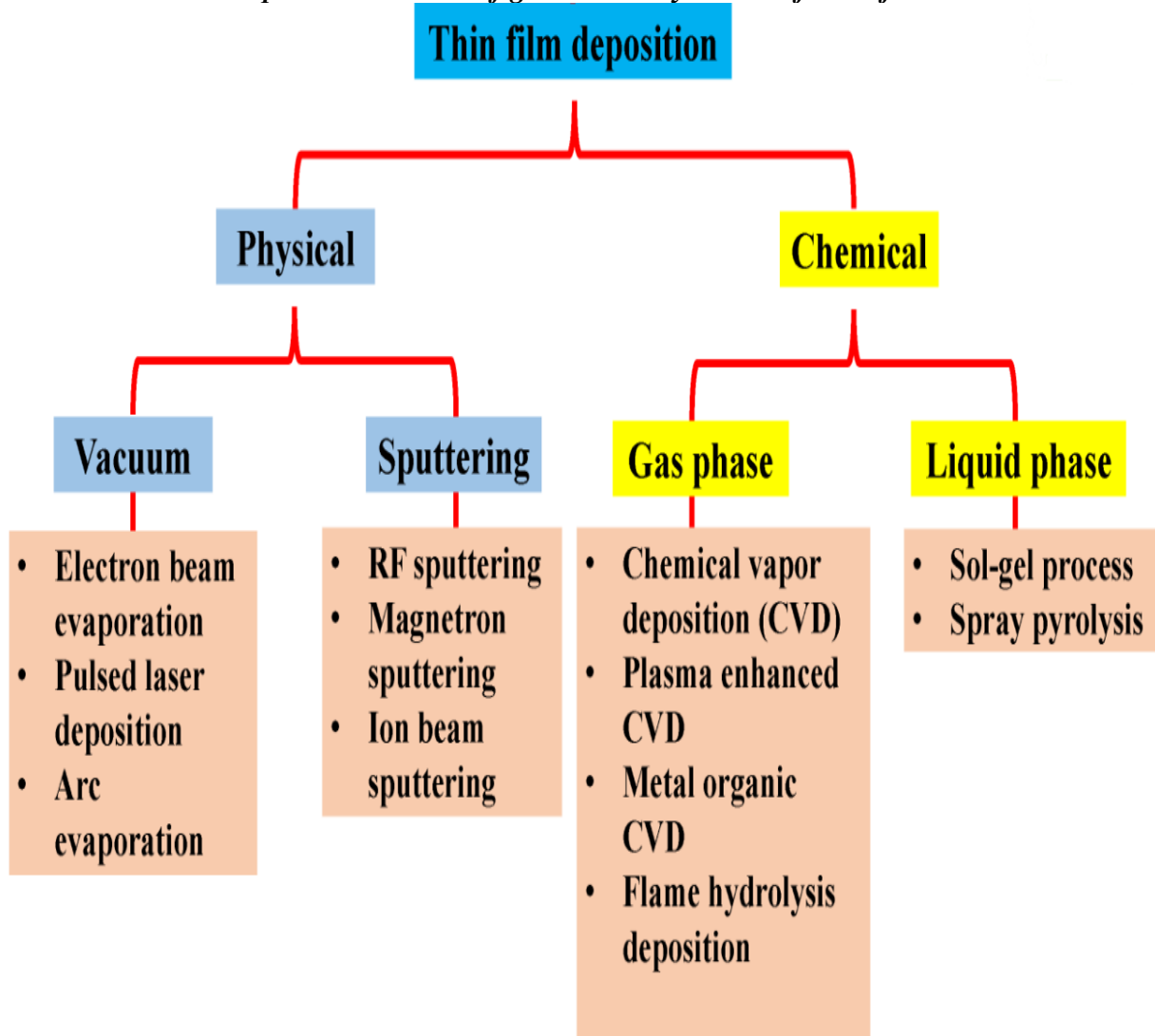
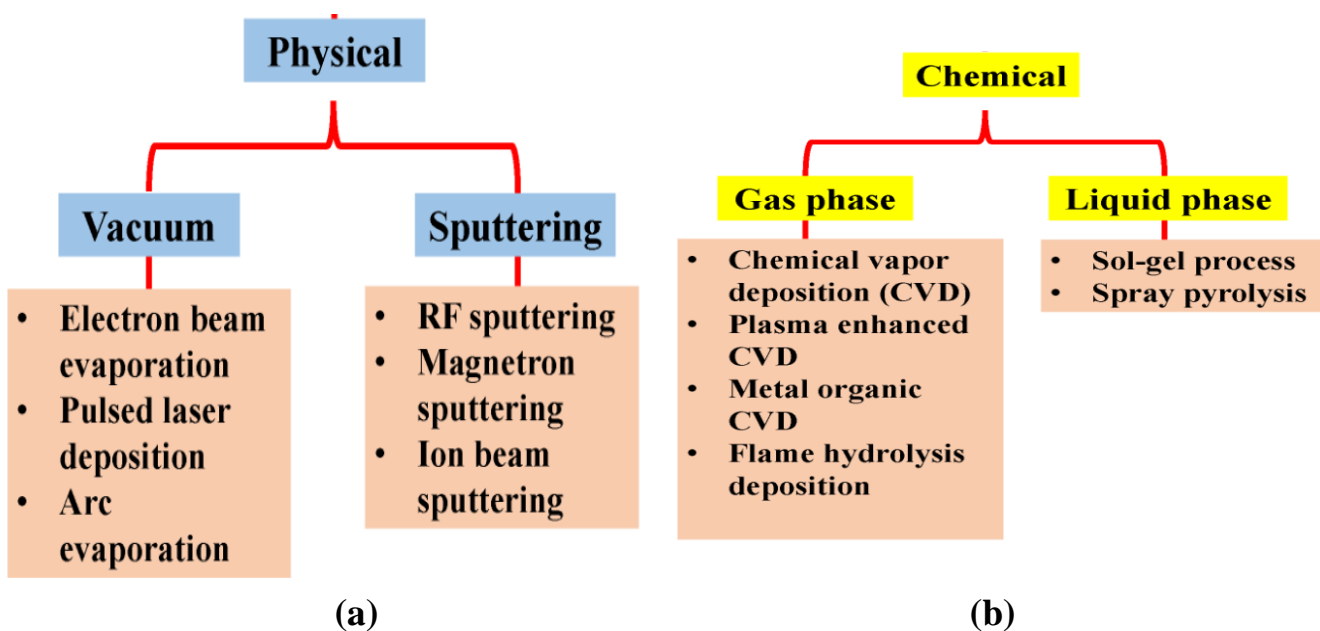


Figure 16 : Different techniques of thin films deposition

[3]



The chosen deposition method is critical in determining the resulting thin film material's purity, performance, and behavior [2].

II.I.2. The importance of thin film deposition and coating:

Traditionally, painting has been the primary method for preserving or altering the surfaces of materials and components. Similar to painting, thin film deposition and coating also play crucial roles in various ways:

- Applying thin film materials to substrates enhances their properties, such as optical, electrical, and biocompatibility.
- The deposition of thin films and coatings shields the substrate surfaces from extreme heat, humidity, and acidic or alkaline environments.
- Thin film coating can also be used for decorative purposes [2].

II.II. Thin films deposition:

It is well known that thin film materials are widely used in a variety of applications such as microelectronics, optical coatings, and energy devices. These materials can be produced using various techniques, which are classified based on the physical state of the source material employed in the deposition process. The gaseous state method involves the deposition of thin films from a gaseous precursor through techniques such as chemical vapor deposition (CVD), physical vapor deposition (PVD), and atomic layer deposition (ALD). This method is commonly used for the production of semiconductor and optical coatings.

In the solution state method, the thin film is produced by depositing a solution of the precursor material onto the substrate through techniques such as spin coating and dip coating. This method is often used for the production of thin films in organic electronics and biomaterials.

The molten or semi-molten state method involves the deposition of the thin film by melting or heating the precursor material until it reaches a semi-liquid state. Techniques such as laser ablation and pulsed laser deposition (PLD) are used for this method. This method is commonly used for the production of metallic and ceramic thin films. Gaseous state deposition techniques involve transforming the source material into a gaseous state or using material already in a gaseous form for deposition onto a substrate.

The results of these steps are forming thin films and coatings through condensation. These methods can be categorized into physical vapor deposition (PVD), Chemical vapor deposition, and Ion beam-assisted deposition.

PVD methods involve the evaporation or atomization of the target material without any chemical reactions, and examples include sputtering, thermal spray, arc vapor, ion beam, and pulsed laser deposition.

Chapter II: Methods of growth and synthesis of TCO films

On the other hand, CVD involves the formation of thin film coatings through chemical reactions between gaseous precursors.

The different types of CVD methods are classified based on their operating conditions, such as:

- Thermal,
- low pressure,
- atmospheric pressure,
- laser,
- photon,
- plasma-enhanced, and
- ALD.

Pulsed CVD/ALD/atomic layer epitaxy (ALE) is a superior CVD technology not typically included in the CVD classification due to its ability to overcome the limitations of other CVD techniques.

This method has several advantages, including the ability to form ultrathin films through surface chemical reactions, suitable for high uniformity thin film deposition, widely used for growing hybrid nanostructures, and valuable in semiconductor nanofabrication for producing defect-free thin films.

The deposition methods for thin film materials formation require the source of materials to be liquid/solution. These materials (precursors) must most commonly be in a solution state for the deposition process. Some examples of these solution-state deposition methods include chemical bath solution, sol-gel, and electrochemical deposition methods. These methods typically involve chemical reactions within the solution, forming sediments that deposit on the substrate material as thin films. So depositing thin film coating involves transforming the source material into a molten or semi-molten. This transformation is achieved through laser melting, thermal spray, and weld-based processes. The material is then atomized through high-pressure acceleration and deposited onto the surface of the substrate material [2].

II.II.1. Thin-film growth:

The field of thin-film growth has made significant progress over the last few decades. A wide range of growth methods (physical or chemical techniques) is now available, including heavy ultra-high vacuum systems and chemical deposition techniques, which have enabled the production of high-quality thin films with desirable properties that are widely used in industry.

The development of films is significantly impacted by the substrate's attributes, the film's thickness, and the method used for deposition. The formation of a thin film material is a complex process that involves three distinct phases as shown in Figure 18:

Firstly, the film's species are formed by the interaction between energy systems and precursors/reactants/target material.

Chapter II: Methods of growth and synthesis of TCO films

Secondly, the species are transported through a vacuum to the substrate surface. Finally, the species grow on the substrate surface to form the desired thin film structure [4].

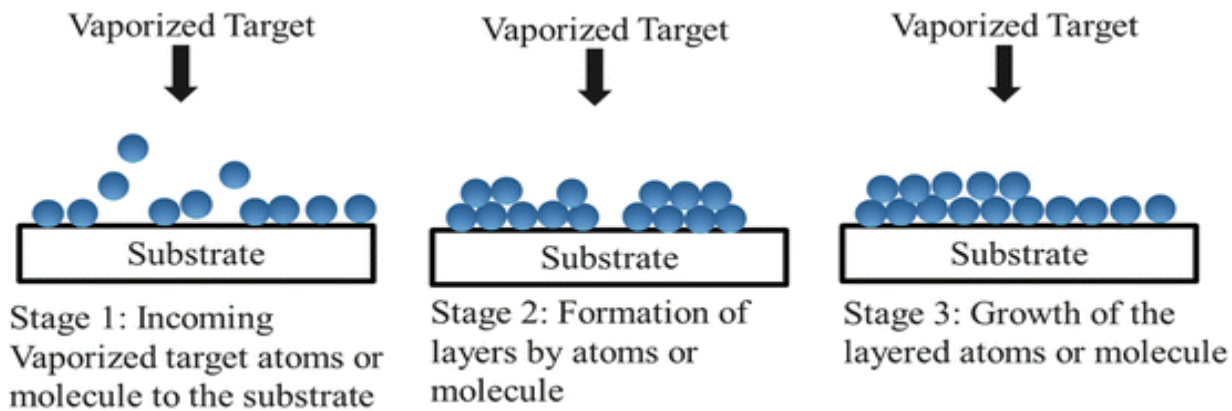


Figure 18 : Different phases of thin film growth

[4]

Several factors, including the activation energy, the binding energy between the substrate and species, and the sticking coefficient, influence the behavior of the film's species on the substrate surface [2].

The growth process of thin films is divided into:

- condensation
- diffusion
- nucleation
- grain growth
- Connection of atoms or particle clusters into thin films on substrates.

The quality and characteristics of a thin film are significantly influenced by the nucleation process, which is a crucial factor in promoting proper crystallization and microstructural development during thin film growth [5]. As explain in Figure 19, there is three fundamental modes of nucleation that exist:

- Island or Volmer-Weber growth
- Layer or Frank-van der Merwe growth
- Island-layer or Stranski-Krastonov growth

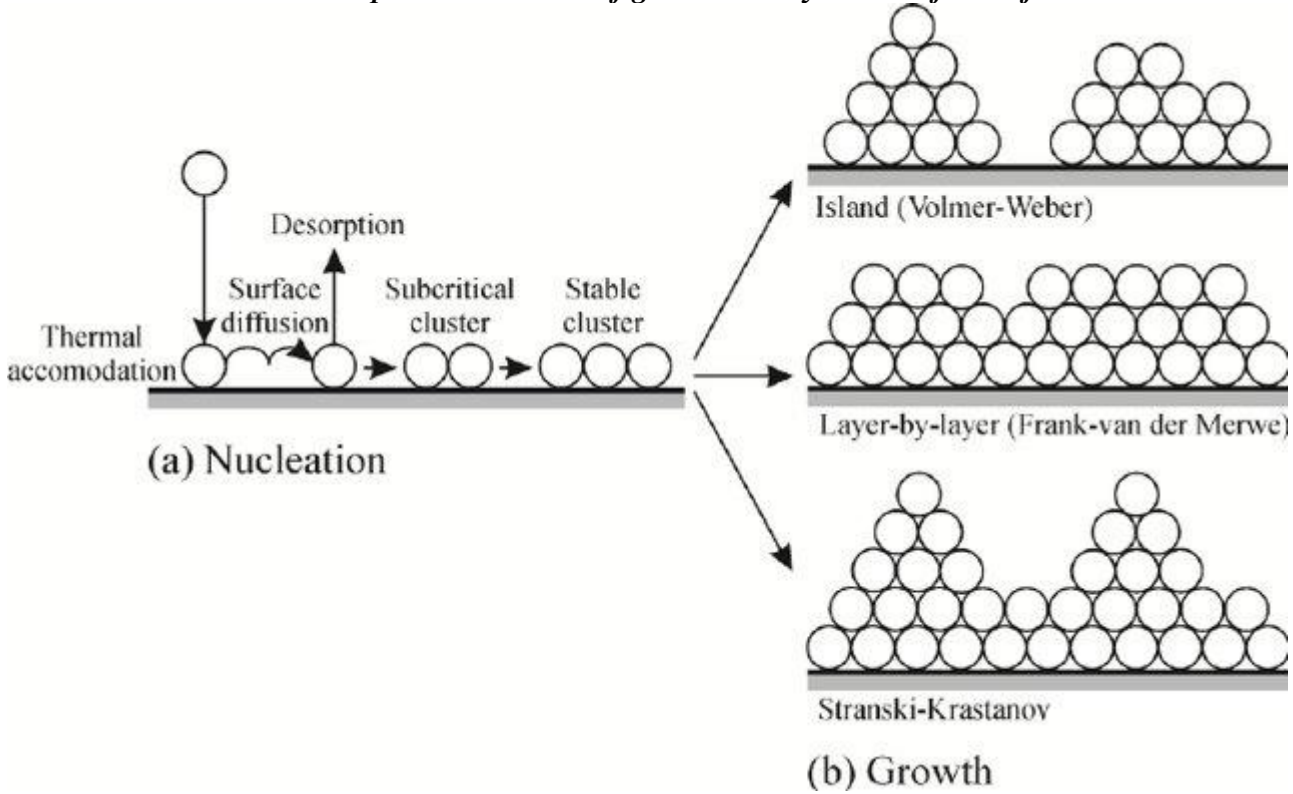


Figure 19 : The three model of growth issued from the fundamental modes of nucleation. [6]

II.II.1.1. Formation of island or Volmer-Weber mode:

In the Volmer-Weber growth mode, the species that contribute to the growth exhibit stronger bonding with each other compared to the substrate, resulting in the formation of clusters or 3D islands. This nucleation process is commonly observed during the early stages of film deposition in metals on insulator substrates, as well as graphite and mica substrates. This mode of growth is particularly crucial in the formation of low-dimensional structures like quantum dots, where precise control over island distribution, density, and size is necessary.

II.II.1.2. Layer by layer growth, Frank-van der Merwe mode:

When atoms are adsorbed onto a surface, their likelihood of bonding to the substrate is higher compared to bonding with each other. This results in the formation of a first monolayer before subsequent layers can grow. The epitaxial growth of single-crystal layers is a prominent example of this mode. In the growth of topological insulators such as bismuth chalcogenide compounds, the Frank-van der Merwe mode plays a crucial role as it helps to minimize structural defects during the formation of epitaxial layers. Therefore, this mode is necessary for achieving high-quality epitaxial layers and ensuring the desired electronic properties of topological insulators.

II.II.1.3. Island-layer growth, Stranski-Krastonov mode:

This mode of growth is an intermediate state in which atoms are gradually adsorbed layer-by-layer, combining aspects of both preceding modes. As the layer thickness reaches a critical point, the accumulated elastic energy dissipates, resulting in the formation of clusters or islands. This mechanism is indicative of a transitional stage in the growth process [7]. Every growth mode plays a crucial role as they are tailored to specific applications.

II.II.2. Parameters influencing thin film depositions:

There are many parameters that impact thin film growth. These parameters can be classified into three categories:

- a- material properties,
- b- equipment parameters,
- c- other external factors.

The deposited material can also be influenced by various factors, including both the material properties and deposition equipment parameters. The material properties parameters encompass:

- The chemical composition and properties of the target/precursor and substrate materials,
- The surface roughness of the substrate
- The binding energy of atoms in the target materials.

Improving the understanding of how these parameters affect the deposition process can help in designing materials with desired properties, as well as improving the efficiency and quality of the deposition process. Thin film deposition may be impacted by external factors such as the operator's level of expertise, the chemical composition of catalysts utilized, and the characteristics of doping materials employed. Deposition processes are impacted by multiple factors, making the selection of the optimal process parameters for producing high-quality thin films a complex task. The effect of each parameter on specific deposition techniques is not straightforward and requires multiple experiments and designs to determine the ideal combination for forming high-quality thin films [2].

II.II.3. Properties of nanofilms:

Thin films can be growth in nanostructured films and exhibit distinct properties compared to their bulk counterparts. Some of the critical features of thin films include:

- Exceptional mechanical properties include high yield strength, resistance to high residual stress, and attractive elastic and plastic characteristics.
- Superior optical properties like reflectivity and absorption across different energies.
- Improved electrical properties are influenced by: film thickness, lattice dimensions, and surface roughness.
- Structural stability in various conditions, such as high temperatures and low temperatures.

Chapter II: Methods of growth and synthesis of TCO films

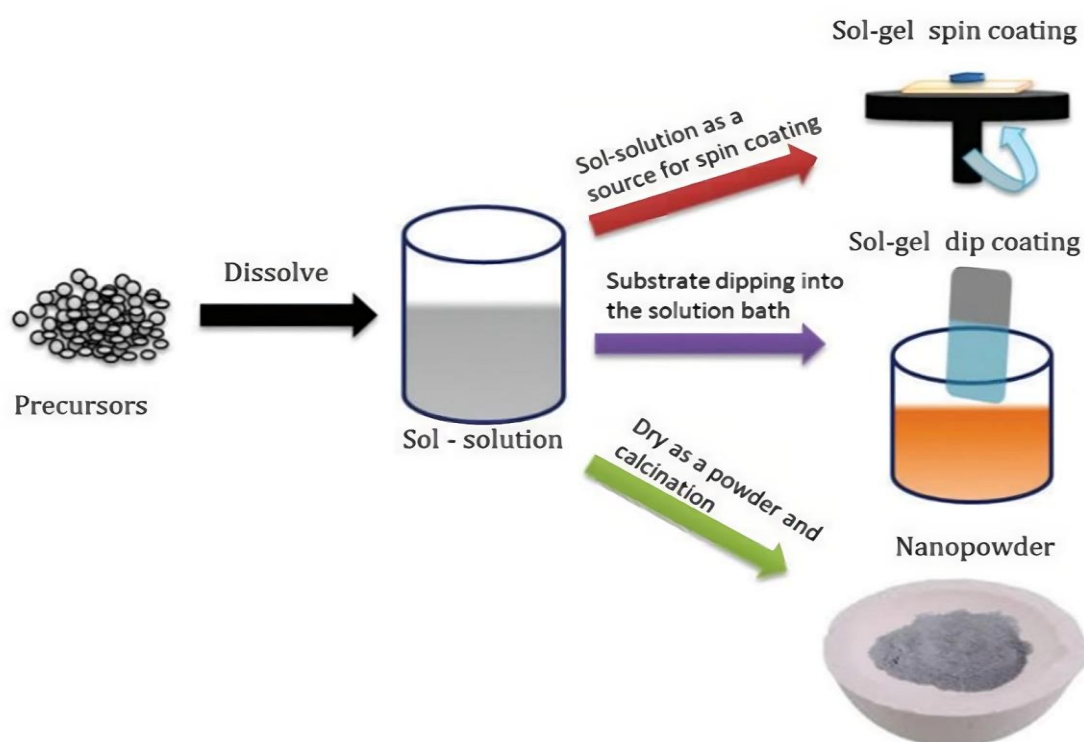
- Low surface roughness and precise film thickness influence the material's surface protection and functional characteristics.
- Controlled chemical composition during the deposition process enhances the material's chemical behavior.
- Excellent wear and corrosion resistance properties make the thin film suitable for protecting various surfaces [2].

II.III. The used synthesis methods in this work

In this work, we used soft chemistry synthesis methods. They are low cost methods, very simple to set and require only small materials compared to physical methods. We have used spin coating method and spray pyrolysis techniques but the presented results are obtained from spray pyrolysis. We describe in the following paragraphs the basic operating principles of these two methods

II.III.1. Spin coating method

Spin coating is a procedure used to deposit uniform thin films onto flat substrates as glass substrates. As shown in Figure 20, the substrate covered by the solution is then rotated at high speeds to spread the deposited solution by centrifugal force. The solution prepared previously by dissolution of a precursor in liquid medium (distilled water or alcohols), is a form of colloid that comprises solid particles that are uniformly dispersed in a liquid medium. During rotation, the solution spins off the edges of the substrate, until the desired thickness of the film is achieved.



II.III.2. Spray pyrolysis:

Spray pyrolysis is one of the best methods of producing transparent oxide films. Spray pyrolysis is a process in which a thin film is deposited by spraying a solution on a heated substrate where the solution reacts to form a chemical compound. The experimental system is presented in Figure 21. Spray pyrolysis technique offers considerable preparative parameters to control airflow, spray rate, adherence of substrates, solution concentration, droplet size, volume, gap between the substrate, and spray gun. This technique is particularly useful for the deposition of different oxides. It is gradually updated to improve the quality of the films.

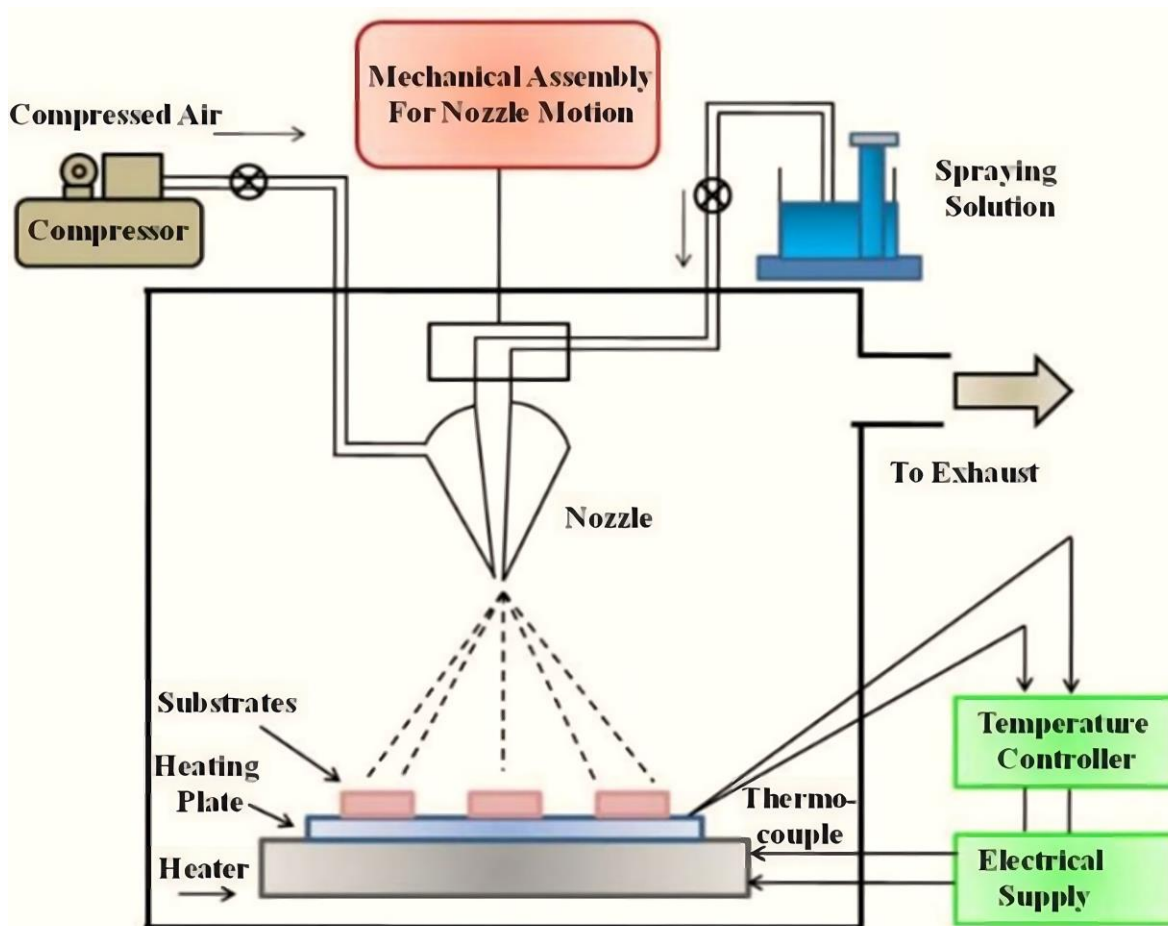


Figure 21 : Schematic experimental system of spray pyrolysis process. [9]

Spray pyrolysis requires a precursor solution, for example, Zinc acetate dehydrate ($\text{Zn}(\text{CH}_3\text{COO})_2 \cdot 2\text{H}_2\text{O}$) for ZnO films, copper nitrate hydrate ($\text{Cu}(\text{NO}_3)_2 \cdot \text{H}_2\text{O}$) for CuO deposit, nickel nitrate hexahydrate ($\text{Ni}(\text{NO}_3)_2 \cdot 6(\text{H}_2\text{O})$) for NiO films... and a heated substrate. In this process, the solution is atomized in small drops and these droplets are transferred to the heated substrate due to compressed air that generates thin films formation.

II.III.3. Advantages of Spray pyrolysis:

The major advantages of spray pyrolysis are principally its low cost and its high production rates but it has other advantages over other methods:

- Open atmosphere process
- It allows simple doping of films by adding desired elements into the spray solution in specific proportions
- It can operate at moderate temperatures and develop films on various substrate materials.
- It uses a large surface area deposition can be reproducibly achieved
- Its Ability to observe the deposition process in progress
- Not necessary to use high-quality reagents as precursors.
- High surface area allows for adjustment of crystal size
- The Product comprise homogeneous compositions
- Ease to dope the thin films

II.III.4. Application Domain of spray pyrolysis technique:

The spray pyrolysis method has yielded TCO films that find application in diverse devices in particular in optoelectronic. One of the most common and interesting applications for TCO materials is in the solar cell field as transparent contacts.

The properties of TCO films are very suitable for applications as transparent ohmic contacts in thin film solar cells as well as an active and antireflection electrode in the design of efficient surface-barrier semiconductor photodetectors. Recently, the quite important optoelectronic application of this method for the fabrication of efficient silicon solar cells and modules has been reported. TCO materials of the ZnO and SnO₂ have shown high conversion efficiencies.

The CdTe and CIGS (copper indium gallium selenide) solar cells are both constructed from a number of different materials with different properties. The CdTe and CIGS cells are built-up as shown in Figure 22. In the CIGS cell, the TCO material is deposited in the last step and requires a low deposition temperature, preferably below 200 °C, to avoid degrading of the CIGS/CdS interface. In the CdTe cell, the TCO material is deposited first, which makes it possible to use higher deposition temperatures [10].

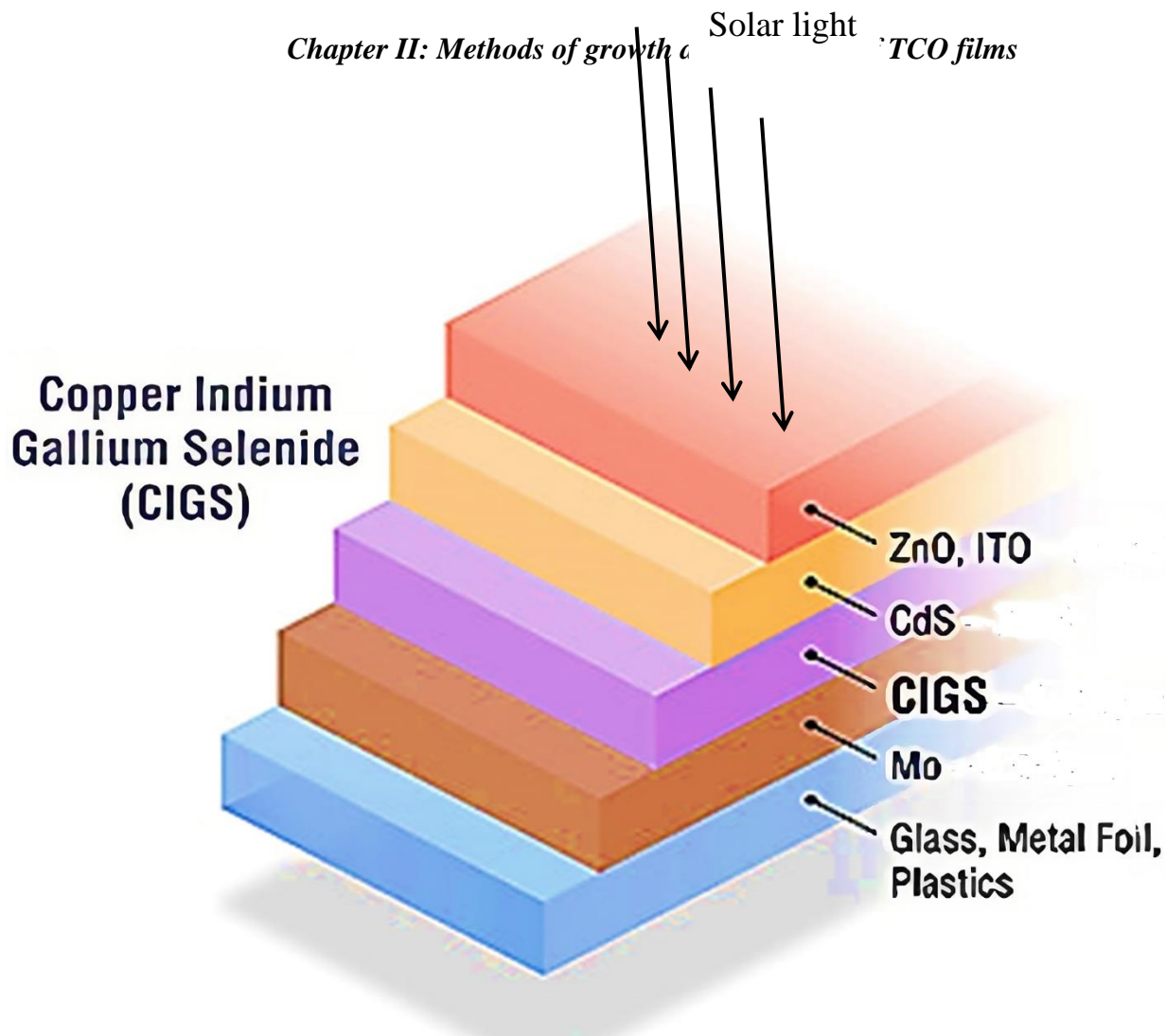


Figure 22 : The multi-layer build-up of photovoltaic CIGS Solar cell [11]

II.IV. Synthesis of pure and doped MnO

We have used in this work spray pyrolysis technique to synthesis pure and Mg-doped MnO. Manganese oxides in nanometric films are intriguing compounds possessing excellent electrochemical activity allowing it to be used in electrochemistry applications. Due to the three Mn^{2+} , Mn^{3+} and Mn^{4+} different oxidative states of manganese, the manganese oxide compound exists in four structures (MnO , Mn_2O_3 , MnO_2 and Mn_3O_4) [12], which all present interesting physical and chemical properties as important as those of the metal oxides materials (ZnO , SnO_2 , NiO , CuO , ...) belonging to the transparent conducting oxides (TCO) family. Manganese oxide thin films are well suited for various applications such as in optoelectronic applications for their use in solar energy conversion [13, 14].

Experimentally, pure and doped manganese oxide thin films were deposited onto heated glass substrates using the spray pyrolysis technique. The primary solution permitting to obtain pure manganese oxide was prepared with 0.1 M manganese chloride ($MnCl_2 \cdot 6H_2O$) in 100 ml deionized water. A secondary solution prepared from magnesium chloride hexahydrate ($MgCl_2 \cdot 6H_2O$) was added for the Mg-doping to the primary solution at various concentrations ((Mg/Mn) ratio: 3%, 5%, 7% and 9%). These solutions were sprayed onto heated

Chapter II: Methods of growth and synthesis of TCO films

glass substrates maintained at 350 °C during the deposit time. Important results are obtained, they are shown, interpreted and commented in chapter 4.

Bibliography of chapter II

1. Breeding, S. and W.E. Johnson. *Optimization of Thin-Film Solar Cells for Lunar Surface Operations*. in *Thermal Fluids Analysis Workshop (TFAW) 2018*. 2018.
2. Mwema, F.M., T.-C. Jen, and L. Zhu, *Thin Film Coatings: Properties, Deposition, and Applications*. 2022: CRC Press.
3. Butt, M.A., et al., *Optical thin films fabrication techniques—Towards a low-cost solution for the integrated photonic platform: A review of the current status*. *Materials*, 2022. **15**(13): p. 4591.
4. Arunkumar, P., S.K. Kuanr, and K.S. Babu, *Thin film: deposition, growth aspects, and characterization*. *Thin Film Structures in Energy Applications*, 2015: p. 1-49.

Chapter II: Methods of growth and synthesis of TCO films

5. Barbier, A., *Single and heterostructure multiferroic thin films*, in *Magnetic, Ferroelectric, and Multiferroic Metal Oxides*. 2018, Elsevier. p. 487-514.
6. Mühlbacher, M., *High-resolution characterization of TiN diffusion barrier layers*. 2015, Linköping University Electronic Press.
7. Fornari, C.I., et al., *Monte Carlo simulation of epitaxial growth*. Epitaxy; Zhong, M., Ed.; BoD–Books on Demand: Norderstedt, Germany, 2018: p. 113.
8. Chandra, U., *Recent Applications in Sol-Gel Synthesis*. 2017: IntechOpen.
9. Hmar, J.J.L., *Growth And Characterization Of Semiconductor Nanostructure For Device Applications*. 2023: BFC Publications.
10. Johansson, S., *Solution based methods for synthesis of tin and zinc; wires and thin films*. 2012.
11. Bagher, A.M., M.M.A. Vahid, and M. Mohsen, *Types of solar cells and application*. American Journal of optics and Photonics, 2015. **3**(5): p. 94-113.
12. Ghosh, S.K., *Diversity in the family of manganese oxides at the nanoscale: from fundamentals to applications*. ACS omega, 2020. **5**(40): p. 25493-25504.
13. Thirumalairajan, S., et al., *Structural and optical investigation of manganese oxide thin films by spray pyrolysis technique*. Optoelectron. Adv. Mater. Rapid Commun, 2008. **2**(12): p. 779-781.
14. Chahshouri, F., et al., *Nano-Structural Characteristics and Optical and Electrical Properties of Obliquely Deposited Manganese Oxide Thin Films*. SRPH Journal of Fundamental Sciences and Technology, 2021. **3**(4): p. 1-12.

Chapter III:

Techniques of Characterization

The nanofilms are largely determined by their size, shape, composition, and surface properties, making their characterization crucial for their design and optimization and require experimental means of characterization sensitive to their properties. Characterization techniques allow us to understand the properties of nanomaterials at the nanoscale, providing insight into their behavior and interactions with their environment.

This chapter aims to provide an overview of the techniques of characterization used in this work. These techniques are essential for understanding and optimizing their properties and applications. We will discuss some methods used to determine the size, shape, composition, and surface properties of nanomaterials, including microscopy, spectroscopy, and scattering techniques. These methods allow us to study the structural, optical, and electrical properties of nanomaterials and provide valuable information on their behavior and interactions with their environment. As shown in Figure 23, we reported the essential techniques used for study some properties as: structural, optical and morphological properties.

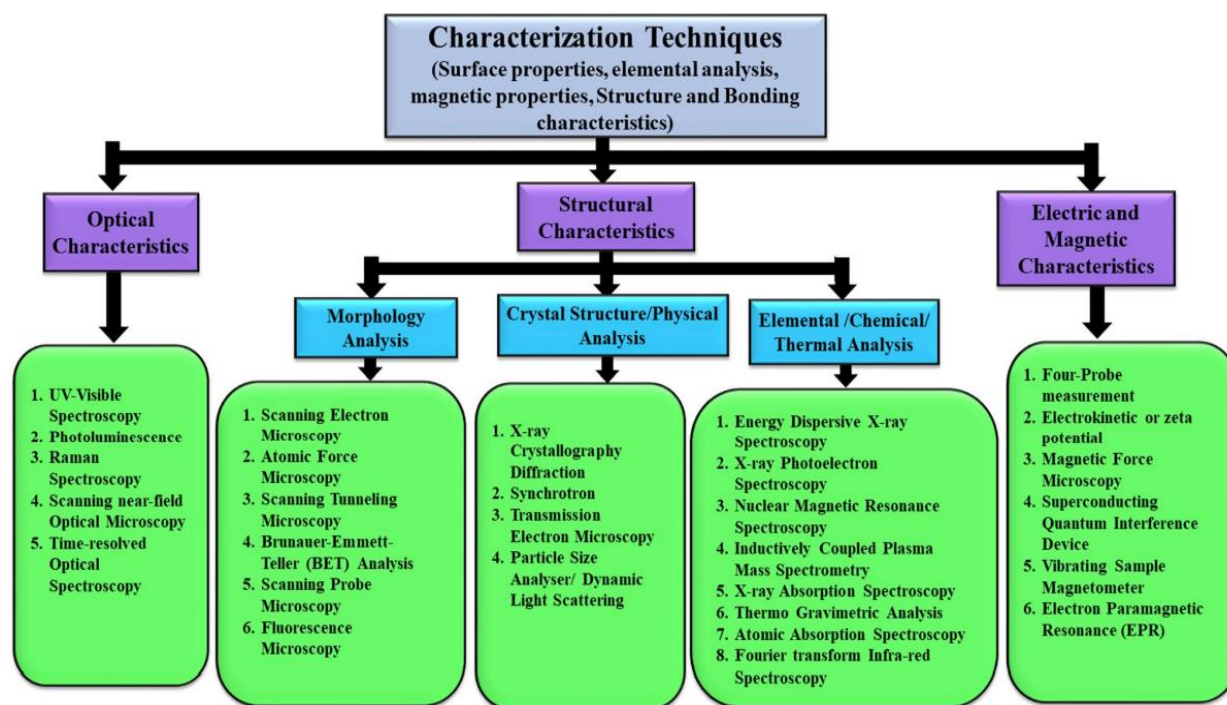


Figure 23 : Some characterization techniques adapted to nanomaterials properties [1] study.

We focus this work on three steps: the first step concerns the structural techniques, which are used to determine the size, shape, and composition of nanomaterials. Structural techniques include microscopy

Chapter III: Techniques of Characterization

techniques such as scanning electron microscopy (SEM), which provide high-resolution images of nanomaterials. Other techniques such as X-ray diffraction (XRD), X-ray photoelectron spectroscopy (XPS), Atomic force microscopy (AFM) are presented and discussed.

In second step, we are interested in the study of the optical techniques, which are used to study the optical properties of nanomaterials such as their absorption, scattering, and emission properties. Optical techniques include UV-Vis spectroscopy, Raman spectroscopy, and Photoluminescence spectroscopy, which allow us to study the optical properties of nanomaterials.

The third and last step of this chapter will be focused on the electronic properties of nanomaterials, which are important for their applications in electronics and energetical properties determined from the conductivity, mobility, and density of states of nanomaterials. Structural Characterization:

III.1.1. X-Ray Diffraction (XRD):

XRD technique based on the elastic scattering of X-rays from structures that have long range order is diffraction of light means the bending of light around the corner of an obstacle. It is a fact that for diffraction to occur. The size of the obstacle should be equal to the wavelength of X-ray. It should be a few angstroms which is approximately the wavelength of X-rays. This technique is commonly used to provide valuable information about the structure and properties of crystalline and nanocrystalline materials. We have used this technique to investigate the formation of polycrystalline phases of pure and doped MnO films.

III.1.1.1. Principle of X-ray powder diffraction:

X-ray diffraction (XRD) is a powerful method for determining the crystal structure and lattice parameters of a material, which have a significant impact on some properties as optical or electrical properties. By analyzing the width of lines in the XRD pattern, the average size of crystallites in a powder sample can also be determined, as long as their size is below 2000 Å. However, the method's limit is reached when the particle diameter is between 20 and 100 Å. Beyond the study of simple crystalline materials, XRD can also be applied to investigate complex substances, such as DNA, using a Bragg spectrometer.

X-ray diffraction is based on constructive interference of monochromatic X-rays and a crystalline sample. In XRD technique, we usually used a monochromatic X-ray beam. When this monochromatic x-ray beam

Chapter III: Techniques of Characterization

interacts on a crystal, the atomic electrons in the crystal are sent into vibration movement with the same frequency as that of the frequency of x-ray beam. The electrons movement emits in all directions.

In order to explain the diffraction of x rays , Bragg [2] considered the X-ray diffraction from a crystal as a reflection of X-rays from the atomic planes of the crystal. The X-rays scattered by the atoms in the crystal lattice create a series of parallel reflecting surfaces, which result in a reflected beam that reaches maximum intensity at a specific angle according to Bragg's law.

Bragg's law in equation (5) deduced from Figure 24, describes the relationship between the wavelengths of the X-ray, the distance between the reflecting planes, and the angle at which the beam is detected. This relationship can be expressed as follows:

$$n\lambda = 2d \sin\theta \quad \text{Eq. 5}$$

Where: d represents the interplanar spacing and θ represents the diffraction angle.

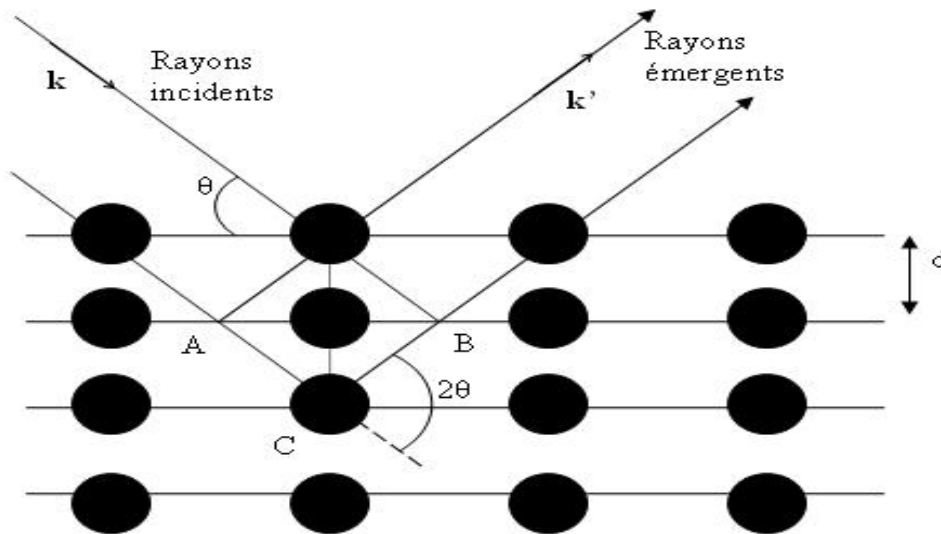


Figure 24 : Basic schema explaining the diffraction Bragg's law

The positions of the intensity maxima are based on the Bragg relation based on the path difference $d = AC + CB$ of the two parallel incident X- rays. If the path difference d is an integral multiple of λ , there will be constructive interference and a maximum will be observed. This path difference is given by the so-called relation from Braag in relationship (1).

Chapter III: Techniques of Characterization

From the experimental, XRD technique is an X-ray diffractometer composed of a goniometer, an X-ray tube, in general, an X source coming from the $K\alpha$ line of copper ($\lambda = 1.54 \text{ \AA}$), a sample holder and an X-ray detector. Figure 25 gives a simplified schema of XRD technique.

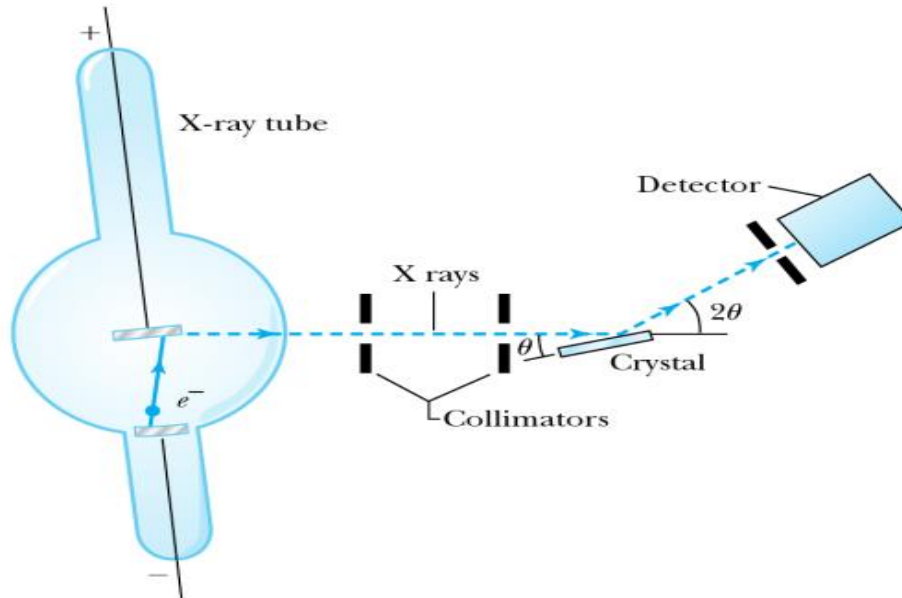


Figure 25 : schematic representation of XRD diffraction

[3]

We therefore obtain from XRD technique a diffraction diagrams called diffractograms which represent the intensity of diffracted photons as a function of 2θ . Thus, using the tables that exist in the databases (ASTM sheets – American Society for Testing Materials), it is possible to identify the crystallinity of phases and their lattice parameters.

III.I.1.2. Determination of lattice parameters using XRD spectrum

Some information may be determined from XRD patterns as lattice parameters, crystallite sizes, strains some density of defects.

i. Determination of cubic crystals from XRD plots (example)

Chapter III: Techniques of Characterization

Recalling Bragg's law:

$$2. d. \sin\theta = \lambda \text{ (with } n = 1) \quad \text{Eq. 6}$$

$$\lambda^2 = 4d^2 \sin^2\theta \quad \text{Eq. 7}$$

$$\sin^2\theta = \frac{\lambda^2}{4d^2} \quad \text{Eq. 8}$$

For cubic crystal, we obtain interplanar spacing, d_{hkl} , from the plane spacing equation:

$$\frac{1}{d_{hkl}^2} = \frac{h^2 + k^2 + l^2}{a^2} = \frac{4 \sin^2\theta}{\lambda^2} \quad \text{Eq. 9}$$

$\frac{4 \sin^2\theta}{\lambda^2}$ is constant and $h^2 + k^2 + l^2$ is an integer related to indices of diffracting planes as θ increases, planes with higher order Miller indices will diffract.

Following this reasoning, we can calculate the lattice parameters for other crystals as face-centered cubic or hexagonal.

ii. Measurement of Crystallite size:

The terms "crystallite size" or «grain size" are commonly used to describe the size of individual crystals in a crystalline powder sample. It's important to note that a powder sample typically consists of many small units known as "crystallites," which can be considered as a single crystal. Therefore, it's essential not to confuse the grain size of a crystalline powder sample with the size of crystallites, as they are fundamentally different physical quantities, even though they may be the same in some cases.

During X-ray diffraction analysis, the size of a crystal is usually referred to as the "size of crystallites," which affects the diffraction peak broadening. When the diameter of crystallites becomes too small (less than 0.1 μm), the diffraction peak broadens, which is known as "peak broadening."

This broadening occurs because of the limited periodic region in the atomic arrangements that produce the same diffraction peak profile. Additionally, non-uniform strain can be introduced into a sample through mechanical grinding, which can cause the lattice planes to become distorted, changing the spacing of any particular set from one grain to another. To perform a structural analysis on a sample using the

Chapter III: Techniques of Characterization

measured diffraction peak profile, it's necessary to consider these two factors. The Bragg law is a generalized equation that can be used to calculate the wavelength of incident X-rays, plane spacing, and Bragg angle.

Scherrer's equation is a commonly used method for determining the size of crystallites from the measured diffraction peak profiles.

This equation (10) employs the $\beta^{1/2}$ of FWHM (full width at half its maximum intensity) for the calculation, rather than using the integral width for the corresponding peak:

$$D = \frac{0.9 \times \lambda}{\beta \times \cos(\theta_B)} \quad \text{Eq. 10}$$

Where:

- λ , which represents the wavelength of the X-rays employed,
- β , which indicates the full width at half maxima (FWHM) in radians,
- θ , which denotes the Bragg diffraction angle.
- D is used to represent the diameter of crystallites that are oriented perpendicular to the plane of measurement [4].

Figure 26 explains how we calculate β

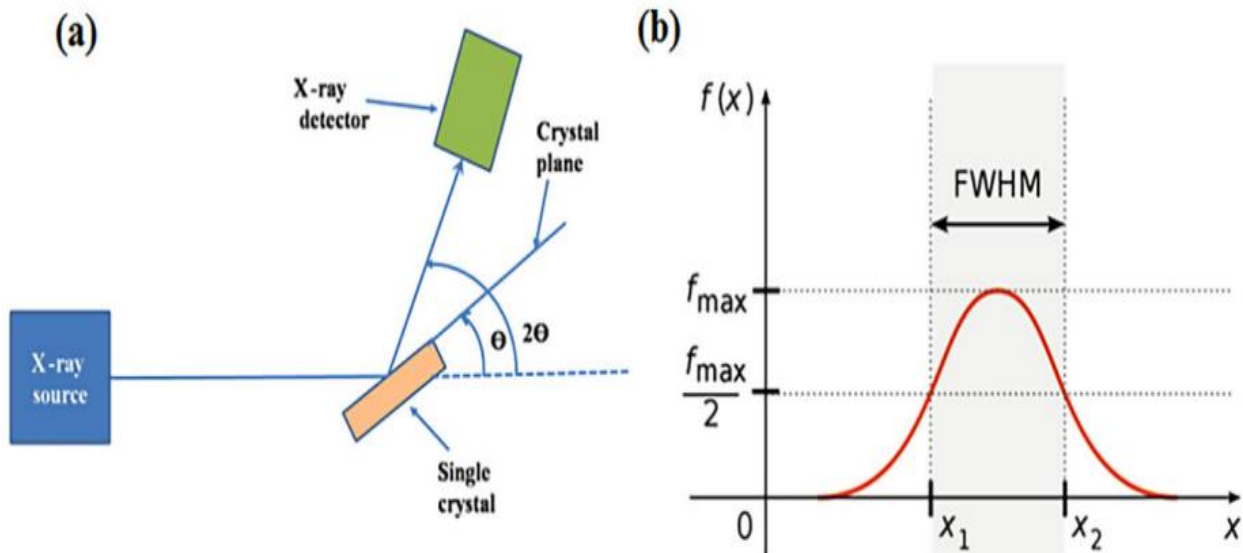


Figure 26 : schematic diagram of an: a) X-ray diffractometer b) full width at half maxima FWHM. [5]

III.II. Chemical Composition:

III.II.1. X-ray Photoelectron Spectroscopy (XPS):

X-ray photoelectron spectroscopy is a technique sensitive to surface composition. Its development is based on the photoelectric effect, which may detect the element existing within a material or covering its surface.

III.II.1.1. Principle of XPS

X-ray photoelectron spectroscopy (XPS) uses soft X-ray beam of energy around 1500 eV which interact with the top few nanometers of the material. The photon penetrates the surface to a depth of approximately 1µm. When a photon interacts with a sample atom, the photon’s energy ionizes core electrons, causing some electrons to be excited and ejected from the surface. Within the bulk of the sample, the mean free path of the ejected electrons is very small due to interaction with the surrounding atoms. But, electrons expelled from atoms in the sample’s top 5nm layer have a high chance of leaving without further interaction. Figure 27 shows the principle of photon electron emission.

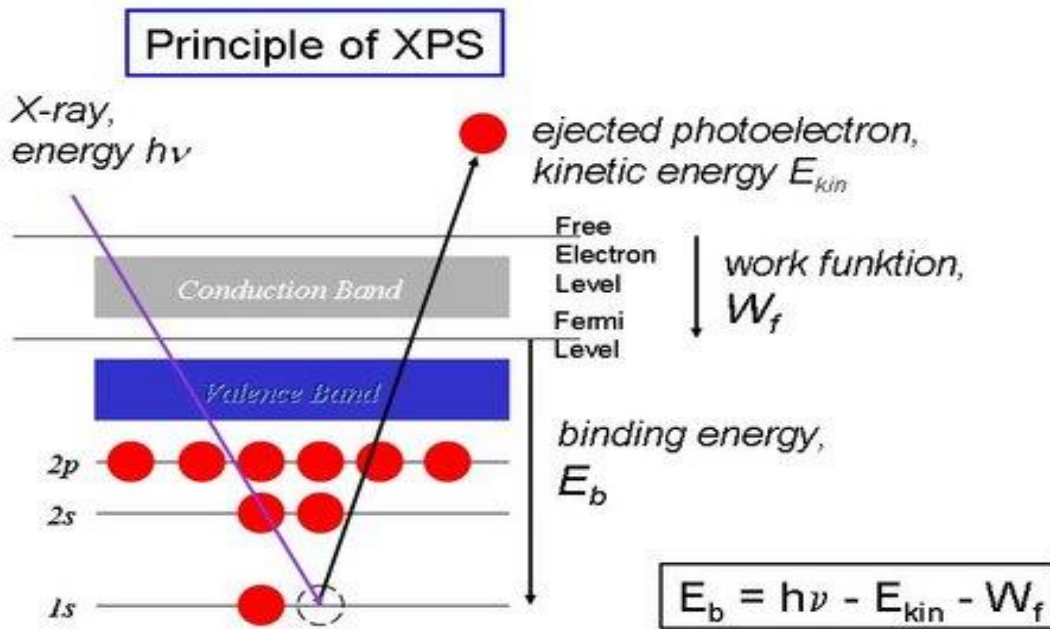


Figure 27 : Principal schema of photoelectron emission in XPS

Chapter III: Techniques of Characterization

The emitted electrons, known as photoelectrons, are then detected. By knowing the energy of the x-rays and measuring the kinetic energy of the emitted photo-electrons with an analyzer, the binding energy of the material can be determined using the equation:

$$E_B = h\nu - E_k - W_f \quad \text{Eq. 11}$$

W_f denotes the work function of a material

The changes in the binding energies reveal important chemical information, such as the element's oxidation state. Experimentally, XPS equipment (Figure 28) is composed of various elements and requires an ultra high vacuum (UHV).

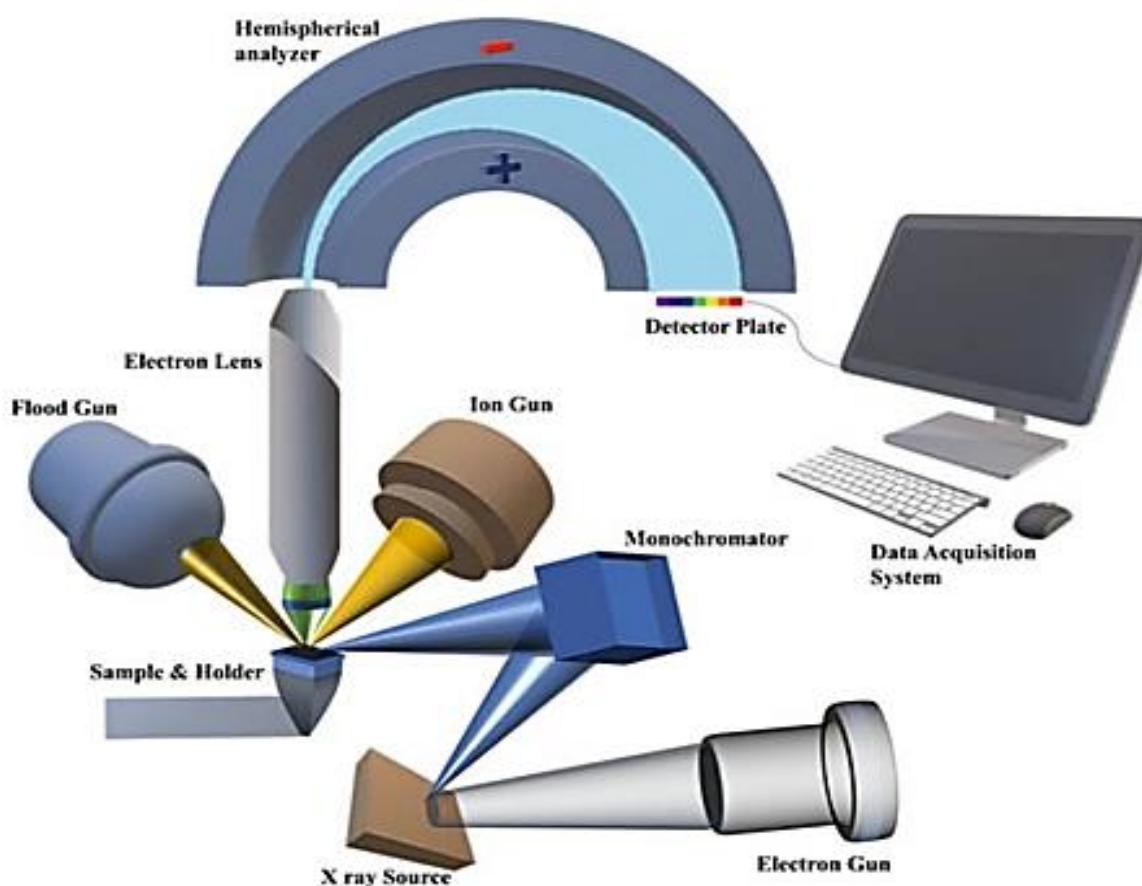


Figure 28 : Schematic representation of XPS Instrument.

[6]

A typical XPS spectrum is composed of many peaks reflecting the chemical elements present in the surface. Figure 29 gives an example of XPS spectrum of SiO₂.

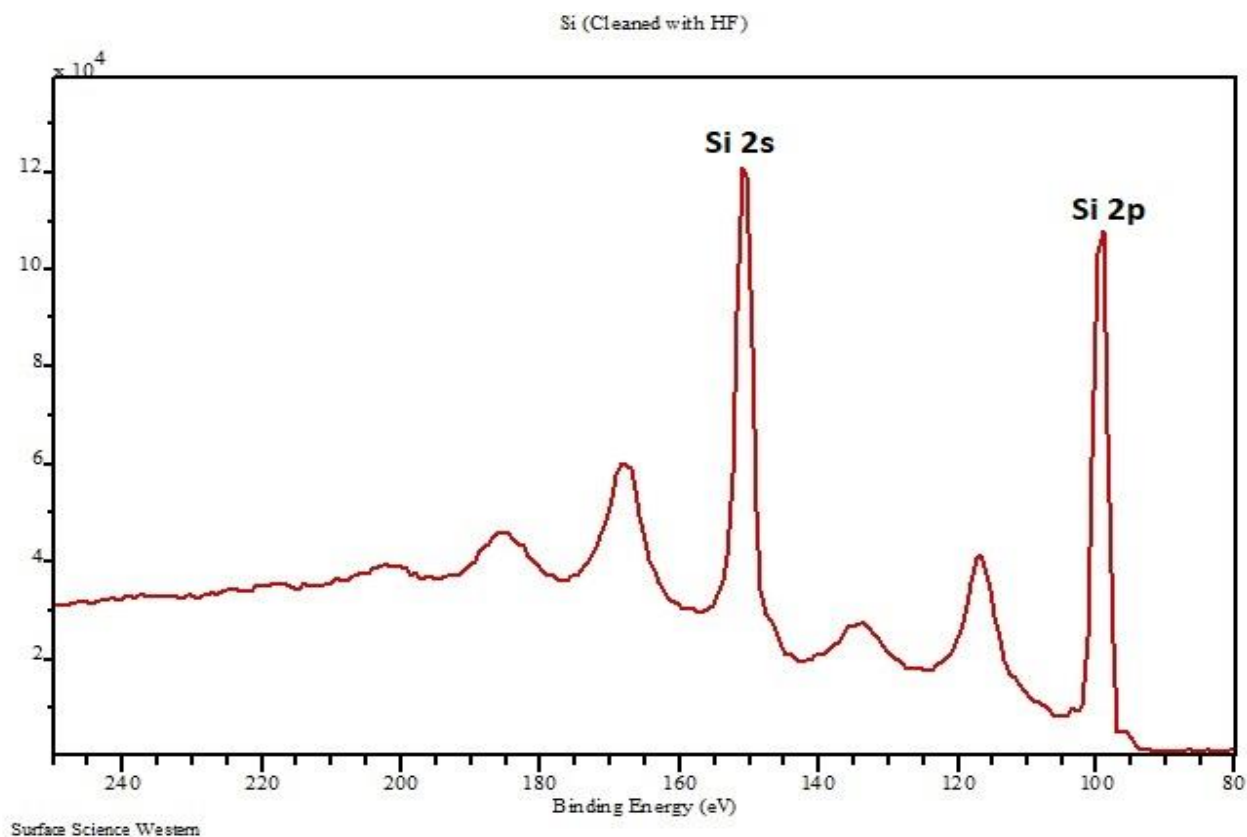


Figure 29 : Typical XPS spectrum of silicon detected from SiO₂ sample [7]

III.III. Morphology study:

III.III.1. Scanning Electron Microscopy (SEM):

Scanning Electron Microscope (SEM) is a tool that is extensively used to investigate surface phenomena of materials. It functions by projecting a high-energy electron onto a sample, generating outgoing electrons/X-rays that is examined. Through this process, it provides significant insights into the surface topography, morphology, composition, grain orientation, crystallographic properties, and other attributes of the material. Morphology pertains to the structure and dimensions of the material, whereas topography refers to the surface qualities like texture, smoothness, or roughness. Composition deals with the components of the material, while crystallography involves the organization of atoms in the material.

The SEM is a highly advanced instrument that offers exceptional spatial resolution of up to 1 nm and can magnify particles up to 300,000 times. While its capability is limited to surface imaging and does not provide internal information, it remains a valuable tool for evaluating a sample's crystallographic,

Chapter III: Techniques of Characterization

magnetic, and electrical properties. Furthermore, the SEM can detect any morphological changes occurring on a particle's surface upon the application of other molecules.

In summary, the SEM is a versatile instrument that enables high-resolution characterization and analysis of materials. It offers critical qualitative insights into the topography, morphology, composition, and crystallographic features of the specimen, including surface properties, dimensions, particle arrangement, chemical components, and atomic order in single crystal particles [8].

III.III.1.1. Working principle of SEM

Scanning electron microscope is a powerful imaging tool that can reveal intricate details of materials at high magnifications with exceptional clarity and depth of focus. The SEM consists of two main components: an electron optical column and a display and operating unit.

The electron optical column includes the electron gun, electromagnetic lenses, and specimen chamber. There are two types of electron guns used in SEM: a thermionic electron gun and a field emission gun. The former utilizes a heated cathode, while the latter has a pointed cathode made of single-crystal tungsten tip.

The potential of the electron gun can be varied from less than 1 kV to 40 kV, allowing for various beam powers and electron penetration depths in the material. The field emission gun has a higher brightness and a smaller energy spread than the thermionic gun, resulting in a smaller probe size for a given beam current. This can be as small as 20 Å for a beam current of 10-11 A or less, and the field emission source has a service life exceeding 1000 hours.

Two condensers and one objective electromagnetic lens create a fine electron beam that is directed towards the specimen surface. The electron probe size can be reduced to 50 Å or 30 Å with a tungsten thermionic or LaB6 filament in emissive mode, while a field emission electron source can produce a probe size of 20 Å or smaller. The beam is deflected by scanning coils, resulting in a square raster scan pattern on the specimen surface.

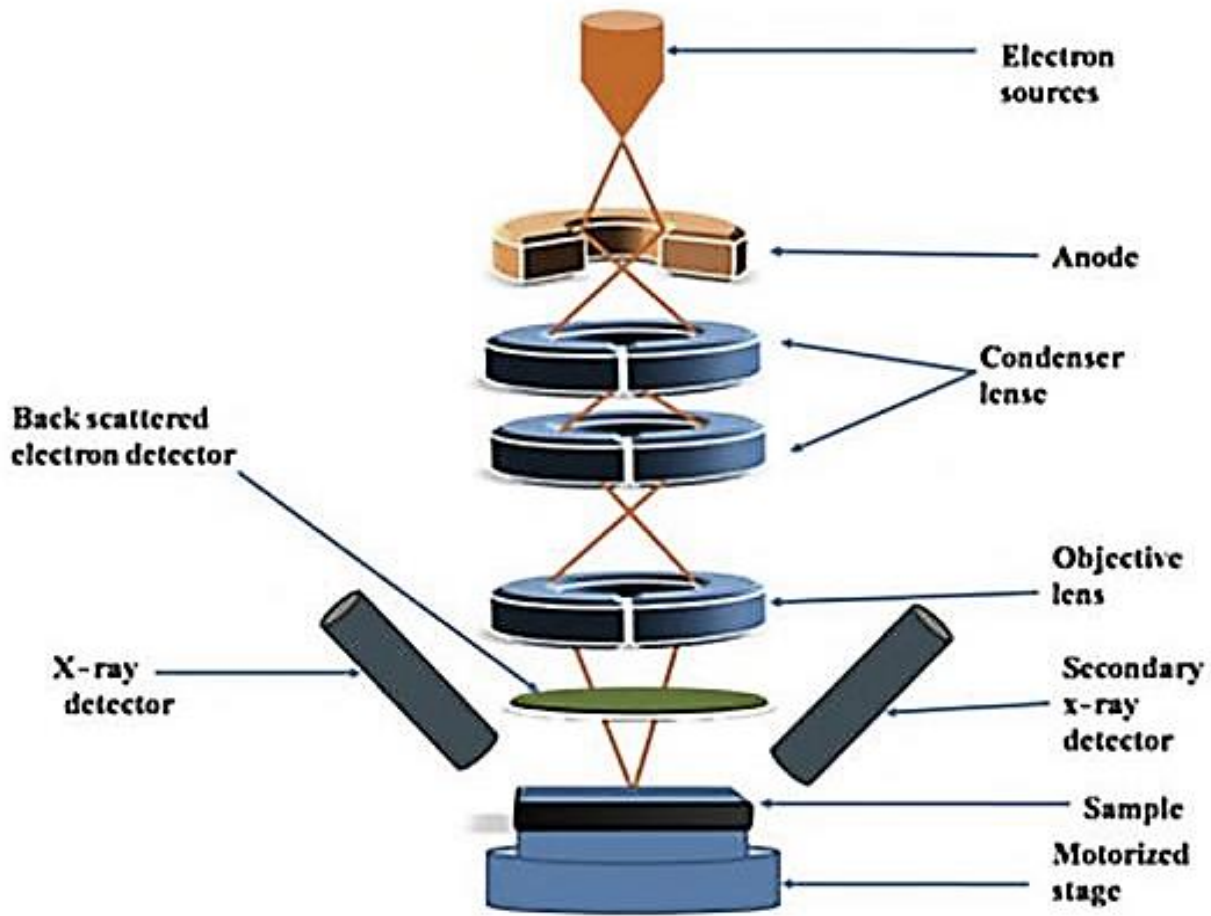


Figure 30: Schematic representation of SEM.

[5]

When the electron beam interacts with the sample, it generates diverse signals that can be captured and converted into an electrical signal by a compatible detector or transducer. Overall, the SEM is an essential tool for researchers and scientists to visualize the detailed structure and composition of materials at a high resolution [9].

III.III.1.2. Applications of SEM:

SEM, or scanning electron microscopy, is an incredibly versatile analytical tool that can be utilized to measure and analyze a vast array of parameters. These parameters include, but are not limited to, film and thin coating thickness, surface morphology and appearance, particle size and distribution, particle shape and dispersion in composites, blends and nanomaterials, dimensions of nanometer-sized materials, cell

Chapter III: Techniques of Characterization

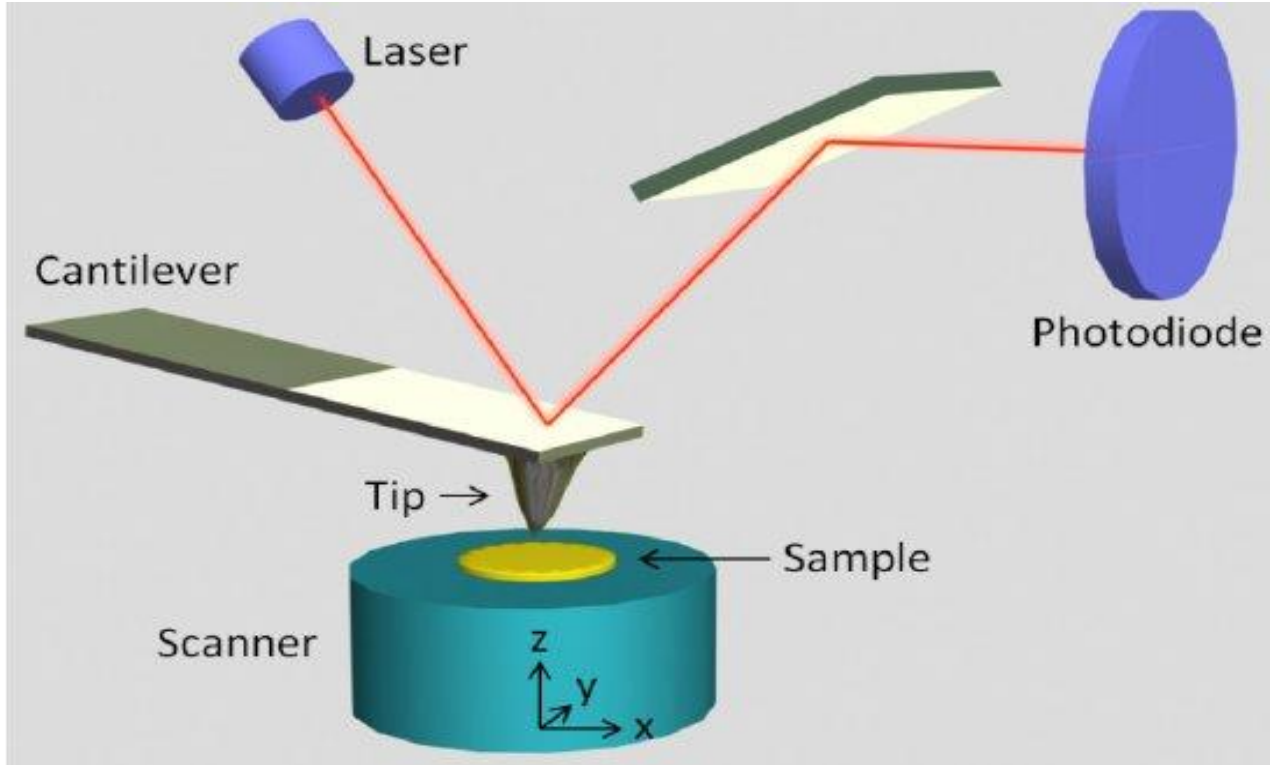
size and distribution in foam materials, chemical composition and elemental analysis of micro and nano materials, as well as structural defect and fracture analysis. With its wide range of applications, SEM has become an indispensable tool for researchers and scientists seeking to understand and optimize materials and structures at the micro- and nanoscale.

III.III.2. Atomic Force Microscopy (AFM)

Atomic Force Microscope (AFM) is a powerful tool which operates on the principle of surface sensing using an extremely sharp tip on a micromachined silicon probe by detecting the force between a sharp probe and the surface being scanned. This tip is used to image a sample by raster scanning across the surface line by line, although the method varies dramatically between distinct operating modes. The AFM can produce high-resolution images of a sample's surface, as well as measure surface roughness and other physical properties. It is suitable for all materials including metals, semiconductors, polymers, and biological. However, the first practical AFM which is a derivative of scanning tunneling microscope, was developed by Gerd Binnig and Calvin Quate at IBM, another led by Christopher Gerber and Art Heinrich at Stanford University, and a third led by Alain Marti and Michel Orrit at Leiden University.

III.III.2.1. How AFM Works

An AFM uses a cantilever with a very sharp tip to scan over a sample surface (Figure 31). As the tip approaches the surface, the close-range, attractive force between the surface and the tip cause the cantilever to deflect towards the surface. However, as the cantilever is brought even closer to the surface, such that the tip makes contact with it, increasingly repulsive force takes over and causes the cantilever to deflect away from the surface.



[10]

Figure 31 : Schematic representation of AFM.

An optical detection system is used to identify the deflection of the cantilever, which is then translated into a force between the tip and sample using the cantilever's spring constant. In the case of a rectangular lever, the spring constant can be determined by:

$$K = \frac{Et^3w}{4l^3} \quad \text{Eq. 12}$$

The Young's modulus (E) of the cantilever material is a crucial factor in determining its mechanical behavior, and it is influenced by its dimensions, such as thickness (t), width (w), and length (l), which are typically measured in microns. The cantilever material is usually made of silicon or silicon nitride. In atomic force microscopy (AFM), the cantilever's spring constant plays a vital role in the quality of the obtained images. The spring constants of most cantilevers used in AFM are in the range from 0.01 to 100 N/m. To obtain high-quality images of the surfaces being studied, the AFM scans the surface line by line. The surface contours are then traced, and they are displayed on a false-color scale, allowing for easy visualization of surface features [11].

Chapter III: Techniques of Characterization

In AFM, the interaction between the sample and the tip surface is often modeled as the interaction between a sphere, representing the tip, and an infinite plane, representing the sample surface:

$$F_v = \frac{H \cdot R}{6z^2} \quad \text{Eq. 13}$$

The Hamaker constant, denoted by H, is a crucial parameter that quantifies the interaction strength between the tip and sample materials. Meanwhile, the distance between the sphere and plane is denoted by z, which directly affects the magnitude of the interaction energy between them.

The force of electrostatics can be represented as the capacitive force between the sample and the tip:

$$F_{el} = \frac{1}{2} \frac{dC}{dz} V^2 \quad \text{Eq. 14}$$

Where C is the capacitance, and the total voltage is represented by V.

AFM imaging at the atomic scale is influenced by chemical forces, which produce contrast in AFM imaging. When conducting experiments on a larger scale using noncontact AFM (nc-AFM) with a tip-sample distance greater than 5 Å, the impact of chemical forces can be ignored. In such cases, topography imaging is mainly influenced by long-range van der Waals forces and, in some cases, electrostatic forces may also play a role [12].

III.III.2.2. Different operating modes of AFM:

i. Contact mode:

In contact-AFM mode (Figure 32), the AFM tip is in a soft physical contact with the surface and is attached to a cantilever with a lower spring constant than the effective spring constant of the sample's atoms. The tip is able to move above the surface with a specific height or under a constant force. The movement is strongly influenced by frictional and adhesive forces that can cause damage to the sample. When the spring constant of cantilever is less than surface, the cantilever bends and the force on the tip is repulsive. By maintaining a constant cantilever deflection (using the feedback loops) the force between the probe and the sample remains constant and an image of the surface is obtained. This ensures that when the tip gently scans across the sample, the cantilever adjusts to change in topography, preventing tip atoms from getting too close to sample atoms. However, a stiff cantilever can be useful for nanopatterning surfaces by causing sample surface deformation during contact.

Contact mode

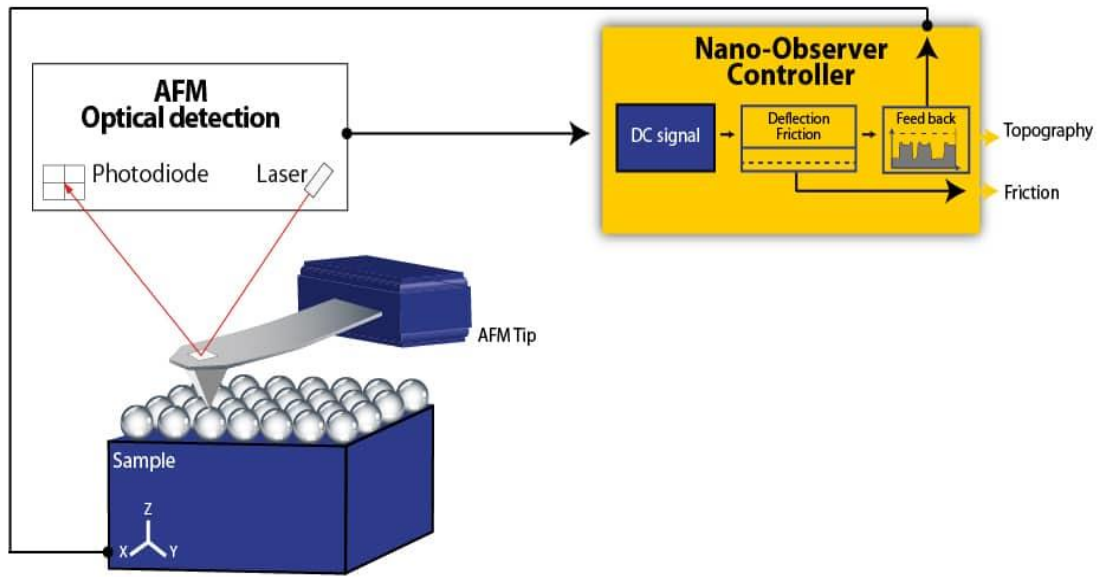


Figure 32 : law Contact mode in AFM

ii. Tapping mode:

Tapping mode (Figure 33(a)) is a dynamic AFM technique that images the sample topography by scanning the surface with an oscillating cantilever. In this mode, the sharp probe tip is not scanned across the sample surface while in constant contact. Instead, the cantilever is vibrated near its resonance frequency causing the tip to oscillate up and down. Tapping mode uses the amplitude of cantilever oscillation to detect changes in the tip-sample interaction forces and thereby the sample topography. The amplitude is used as topography feedback, while the phase lag between drive and detected signal contains information about material-specific mechanical properties. This mode may be explained by Figure 33(b) of the force derived from Lennard-Jones potential (relationship (11)) which is used as approximation for the tip-sample interaction. As indicated in Figure 34, at short distances between the atoms, the interaction is governed by short-ranged repulsive forces, mainly due to the Pauli repulsion, which prohibits the overlap of electron clouds of tip and sample. Above a certain threshold, attractive van der Waals forces dominate the interaction. Van der Waals forces originate from dipole-dipole interactions

$$U(r) = 4U_0 \times \left[\left(\frac{r_0}{r} \right)^{12} - \left(\frac{r_0}{r} \right)^6 \right] \quad \text{Eq. 15}$$

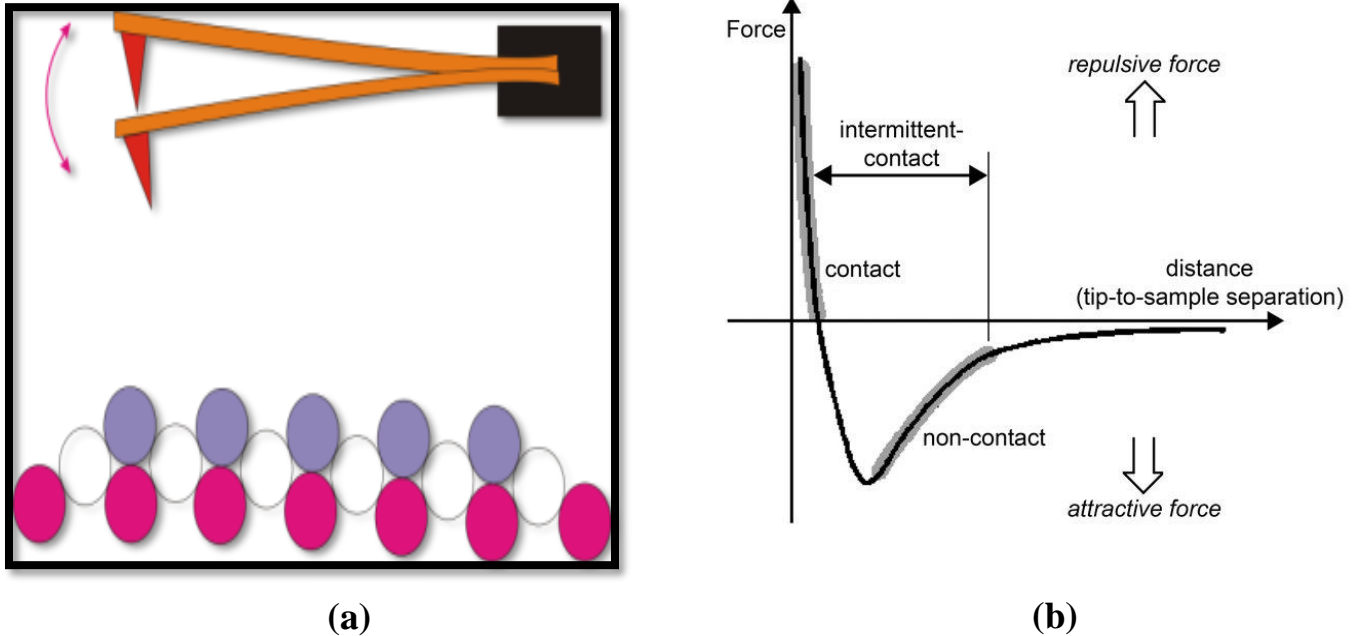


Figure 33 : Tapping mode in AFM (a): schematic tip interaction, (b): Mode contact from Lennard-Jones potential

The tapping mode is the most used mode because it does not damage the tip. We used it in this work.

III.III.3. AFM of laboratory:

All our AFM characterization was made by broker microscope AFM dimension Edge working in various modes. We have chosen tapping mode to characterize AFM images of pure and doped MnO. Figure 34 shows AFM of LSMC laboratory.



Figure 34 : AFM Dimension Edge Model of LSMC Laboratory

III.IV. Optical Analysis:

III.IV.1. UV-visible spectroscopy

The Principle of UV-Visible Spectroscopy is based on the absorption of ultraviolet light or visible light by chemical compounds, which results in the production of distinct spectra. Spectroscopy is based on the interaction between light and matter. The technique utilizes a spectrophotometer as an instrument that measures the extent of light absorption by a sample based on the Beer-Lambert law. When the matter absorbs the light, it undergoes excitation and de-excitation, resulting in the production of a spectrum.

The principle of this technique is based on the interaction of radiation with matter that produces reflection, scattering, absorbance, fluorescence/luminescence, and photochemical reactions. In UV-visible spectroscopy, the focus is on absorbance, where molecules absorb light and increase their energy content. UV photon absorption by molecules can cause transitions between electronic energy levels, leading to narrow absorbance bands at specific wavelengths. This technique can be utilized for quantitative analysis based on the Beer-Bouguer-Lambert law, which indicates that the amount of UV light absorbed by a material is proportional to the number of absorbing molecules:

$$T = \frac{I}{I_0} = e^{-k.B.C} \quad \text{Eq. 16}$$

Where transmittance is represented by the symbol (T), the concentration of the absorbing species (c), incident intensity (I₀), transmitted intensity (I), the base of natural logarithms (e), a constant (k), and path length (b), typically measured in centimeters.

This equation can be converted into a linear equation, resulting in the equation below, which is commonly referred to as Beer's law:

$$A = -\log T = -\log \left(\frac{I}{I_0} \right) = \log \left(\frac{I_0}{I} \right) = \epsilon \times b \times c \quad \text{Eq. 18}$$

The extinction coefficient (ε) of a substance is determined by various factors like: wavelength, solvent, and the instrument used., it's recommended to calibrate or create a working curve using standard solutions with known concentrations of the analyte before analyzing the substance To ensure accuracy [13]. The Figure 35 illustrates a schematic of the uv-visible spectroscopy.

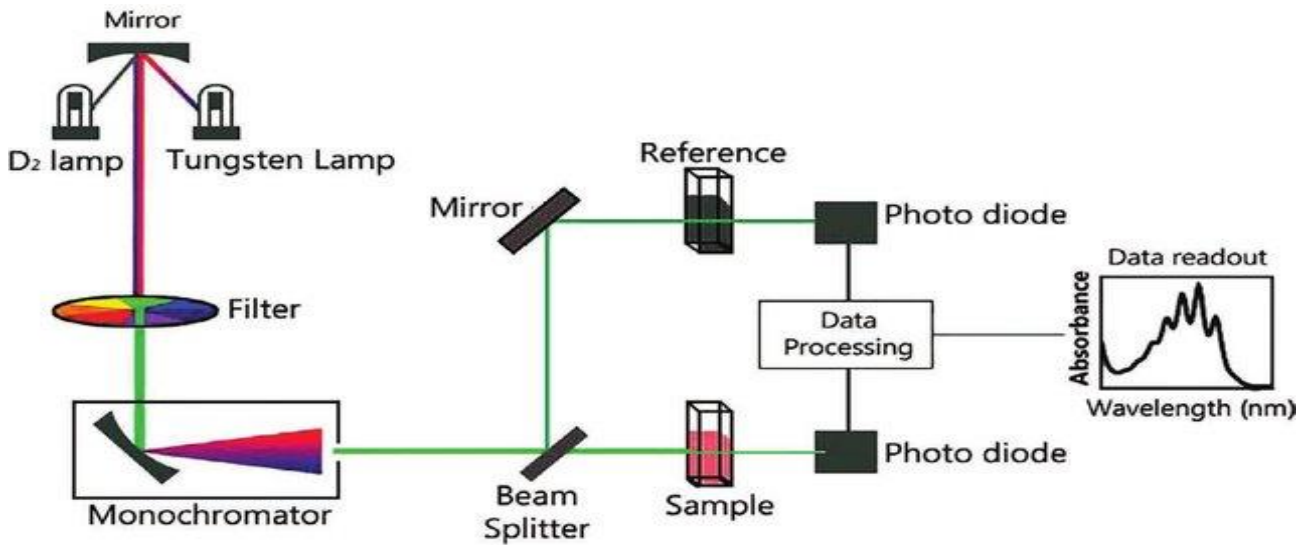


Figure 35 : A simplified Schema of Uv-visible spectroscopy [14]

We have used uv-visible spectroscopy in this work to characterize the transparent properties of pure and doped MnO films by plotting the transmittance curves and deducing the bandgap of the films.

III.IV.1.1. The instrument UV–visible spectroscopy of the laboratory

Figure 36 shows the uv-visible apparatus of the LSMC laboratory which is a specord 50.



Figure 36 : Uv-visible spectrometer of LSMC laboratory

III.IV.2. Photo-Luminescence (PL):

Photoluminescence (PL) spectroscopy is when light energy, or photons, stimulate the emission of a photon from any matter. It is a non-contact, nondestructive method of probing materials. In PL, light is directed onto a sample, where it is absorbed and where a process called photo-excitation can occur. The photo-excitation causes the material to jump to a higher electronic state, and will then release energy, (photons) as it relaxes and returns to back to a lower energy level. The

Chapter III: Techniques of Characterization

emission of light or luminescence through this process is photoluminescence, PL. we have used this technique to study the defects in MnO films.

Bibliography

Chapter III: Techniques of Characterization

1. Kumar, L., et al., *Nanomaterials for remediation of contaminants: a review*. Environmental Chemistry Letters, 2021. **19**: p. 3139-3163.
2. Bragg, W.H. and W.L. Bragg, *The reflection of X-rays by crystals*. Proceedings of the Royal Society of London. Series A, Containing Papers of a Mathematical and Physical Character, 1913. **88**(605): p. 428-438.
3. Thornton, S.T. and A. Rex, *Modern Physics for Scientists and Engineers*. 2012: Cengage Learning.
4. Waseda, Y., E. Matsubara, and K. Shinoda, *X-Ray Diffraction Crystallography: Introduction, Examples and Solved Problems*. 2011: Springer Berlin Heidelberg.
5. Walia, R.S., et al., *Surface Engineering: Methods and Applications*. 2022: CRC Press.
6. Toor, I., *Recent Developments in Analytical Techniques for Corrosion Research*. 2022: Springer International Publishing.
7. Beamson, G. and D.R. Briggs. *High Resolution XPS of Organic Polymers: The Scienta ESCA300 Database*. 1992.
8. Sharma, S.K., et al., *Handbook of Materials Characterization*. 2018: Springer International Publishing.
9. Yacobi, B.G. and D.B. Holt, *Cathodoluminescence Microscopy of Inorganic Solids*. 2013: Springer US.
10. Zeng, G., et al., *Nanomechanics of amyloid materials studied by atomic force microscopy*. Atomic Force Microscopy Investigations into Biology-From Cell to Protein, 2012.
11. Bhushan, B., *Encyclopedia of Nanotechnology*. 2016: Springer Netherlands.
12. Abou-Ras, D., T. Kirchartz, and U. Rau, *Advanced Characterization Techniques for Thin Film Solar Cells*. 2016: Wiley.
13. Akpan, E.I. and S.O. Adeosun, *Sustainable Lignin for Carbon Fibers: Principles, Techniques, and Applications*. 2019: Springer International Publishing.
14. Soni, R.A., R. Rana, and S. Godara, *Characterization Tools and Techniques for Nanomaterials and Nanocomposites*, in *Nanomaterials and Nanocomposites*. 2021, CRC Press. p. 61-83.

Chapter IV:

Experimental results, interpretation and discussion

In this chapter, the experimental results regarding MnO films characterization, will be presented and discussed. It concerns the following points:

1- Analysis of the chemical composition of Mn-O thin films: This part aims to identify and verify the chemical composition of Mn-O thin films.

1- Structural characterization of Mn-O thin films: it is a prerequisite to have a good knowledge of the structure (from the atomic/molecule to the crystal)

2- Morphological characterization of Mn-O thin films: is used to investigate the morphology, size, and dimensions of the metal oxide at the nanoscale

3- Optical characterization of Mn-O thin films: it helps to measure how much the MnO absorbs light, determine the band gap optic, and find the semiconductor type.

IV.I. Compositional analysis of Mn-O thin films:

XPS is a powerful tool for a better characterization of thin film materials. We have used this technique to characterize the chemical composition of synthesized MnO films. XPS results of pure and Mg-doped MnO films were carried out at LISE laboratory of Notre Dame de Namur University Dame de using a K-alpha spectrometer.

IV.I.1. XPS results

In Figure 37, we present the survey XPS spectra of pure and Mg-doped MnO films. This analysis enables us to explore the chemical composition and valence states of manganese and

oxygen in both pure and Mg-doped manganese oxide films.

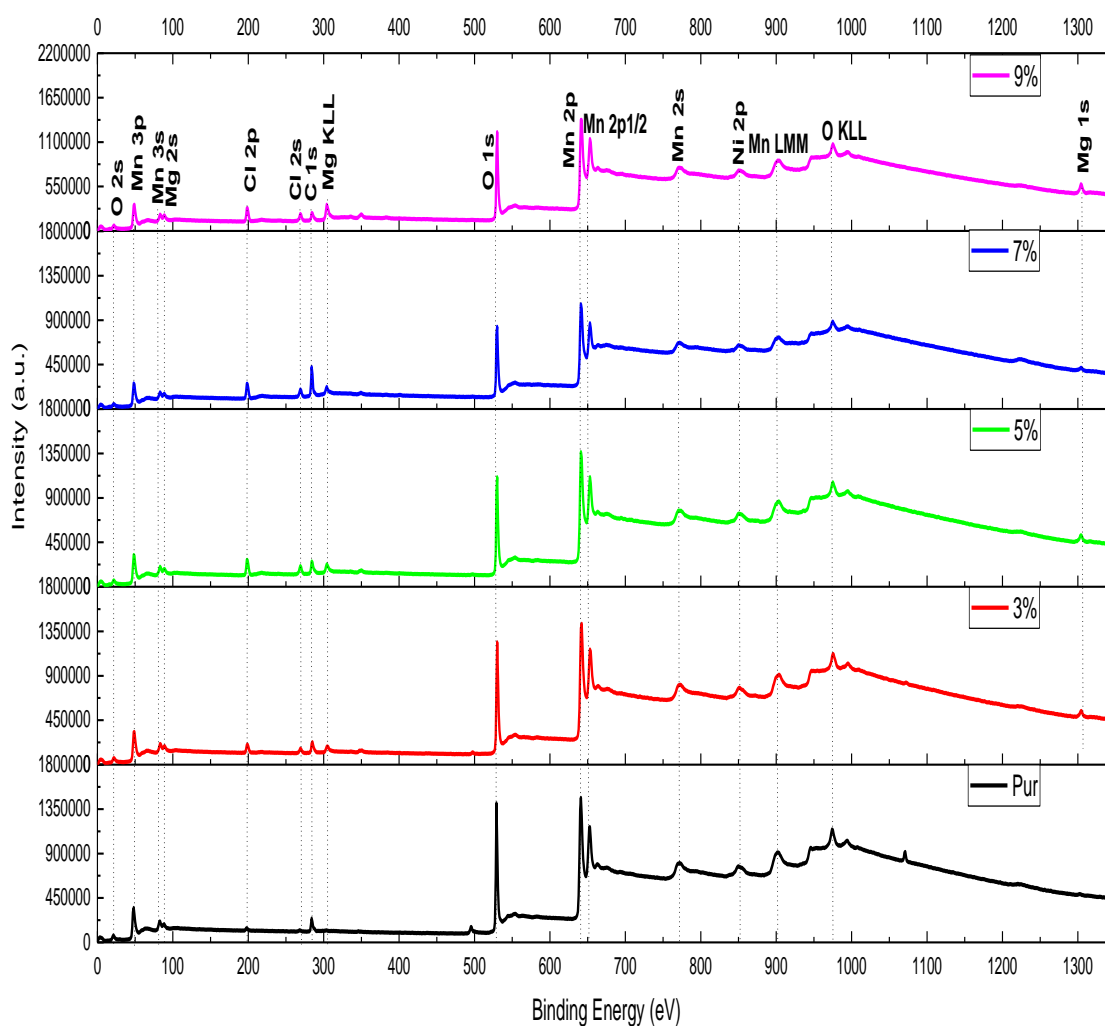


Figure 37 : Survey XPS Spectra of pure and Mg doped Manganese oxide thin films.

From Figure 37, the spectra are dominated by the presence of Mn, O₂ and Mg which shows that we have the formation of the compound Mn-O but we can also observe that MnO surface films are mainly contaminated with carbon (C 1s transition) and with slight traces of nickel (Ni 2p transition). The carbon comes probably from contamination since the deposits are made under air. Nickel is an impurity that the used precursor must contain. At low energies between 0 and 100 eV, we detected three transitions, two of Mn (Mn3s, Mn 3p) and one of Mg (Mg 2s) due to Auger mechanism; they are attributed to the interstitial Mn and Mg thus creating intrinsic defects in the Mn-O lattice. The most significant peaks observed remain Mn (2p_{3/2}), (2p_{1/2}), and O (1s), which

correspond to the most common manganese oxide species. The presence of Mg-KLL transition reveals the presence of Mg at the core level, arising from the doping.

The observed shifts (Figure 38) in the binding energies of the Mn (2p) and O (1s) peaks exhibit an average half-eV oscillation, which may be attributed to the formation of different chemical states of manganese and the creation of composite oxides such as MnO and Mn₃O₄.

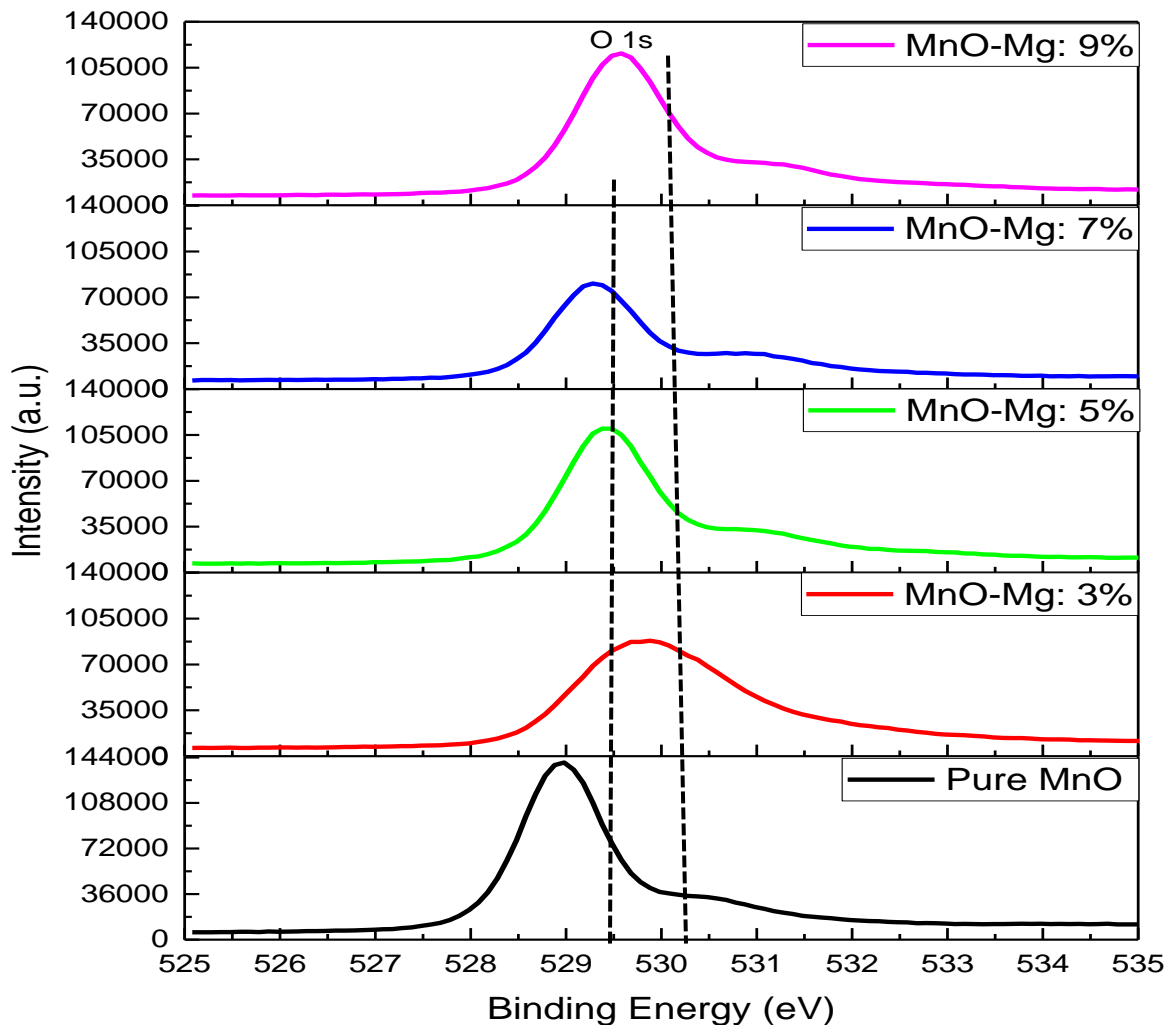


Figure 38 : XPS shifts of the most intense core levels peaks of oxygen O (1s) of pure and Mg- doped MnO

Mn2p and Mn 2p_{1/2} transitions also shift (Figure 39) indicating the variation in the stoichiometry of Mn-O films. MnO pure films exhibit binding energies at 640.4 eV, whereas the binding energies

of Mg-doped films are ranging from 641.0 to 641.5 eV. This observation is related to the insertion of Mg in the Mn-O lattice modifying its stoichiometry. Some published paper on Mn-O [1-3] suggest the formation of Trimanganese tetraoxide is associated with Mg-doped films.

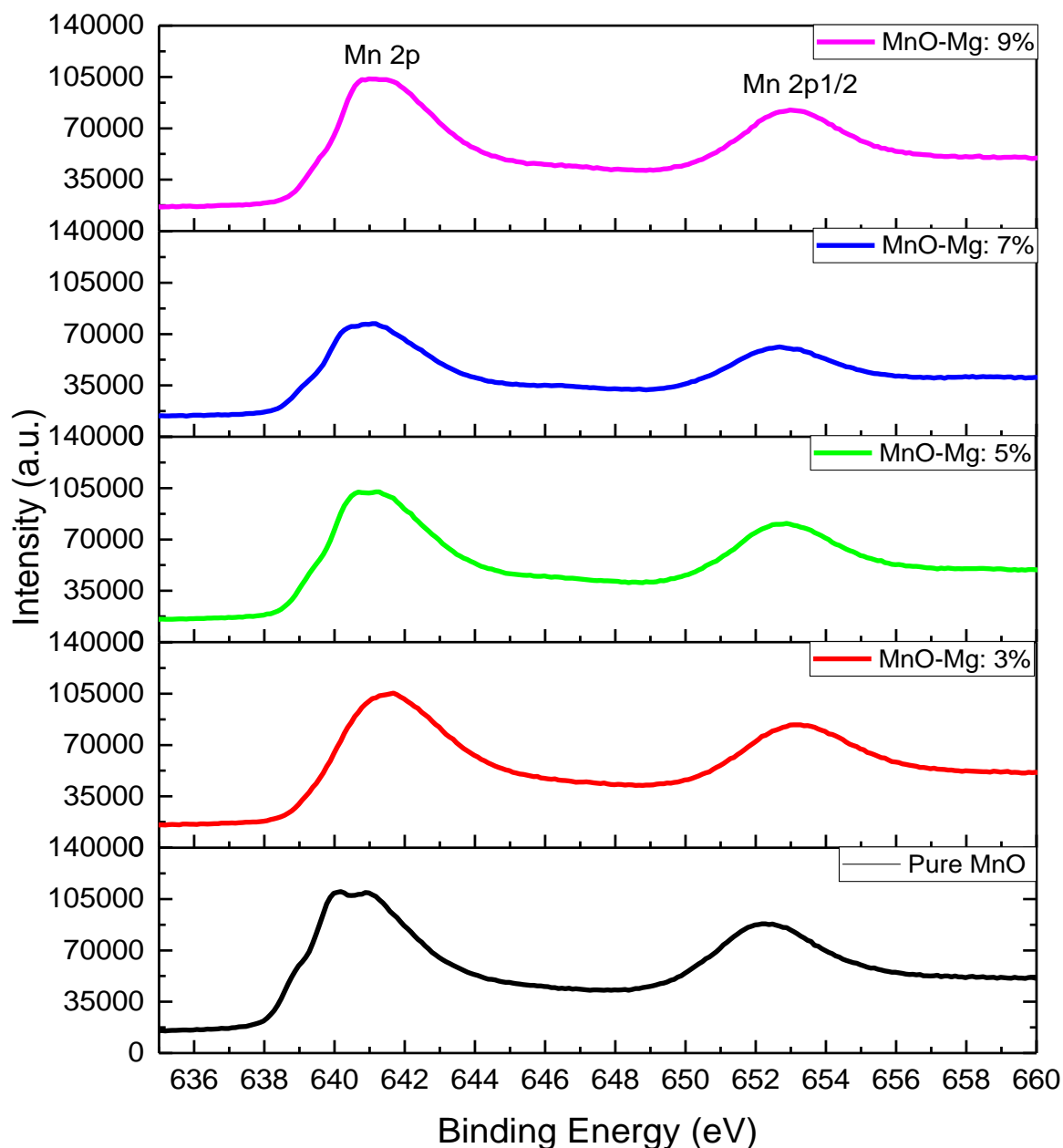


Figure 39 : Shift of Mn2p and Mn 2p_{1/2} transitions highlighting the formation of a non-stoichiometric MnO oxide

IV.I.2. Fitting of Oxygen and Mn transitions:

In Figure 40, we present the fitting of oxygen (O 1s) peak which reveals the presence of two distinct components:

The first component arises from Mn-O bonds and is observed at 529 eV. The second component is a less intense oxygen peak observed at 530.6 eV, which can be attributed to the presence of contaminant molecules (as CO, CO₂) that are loosely bound to the surface.

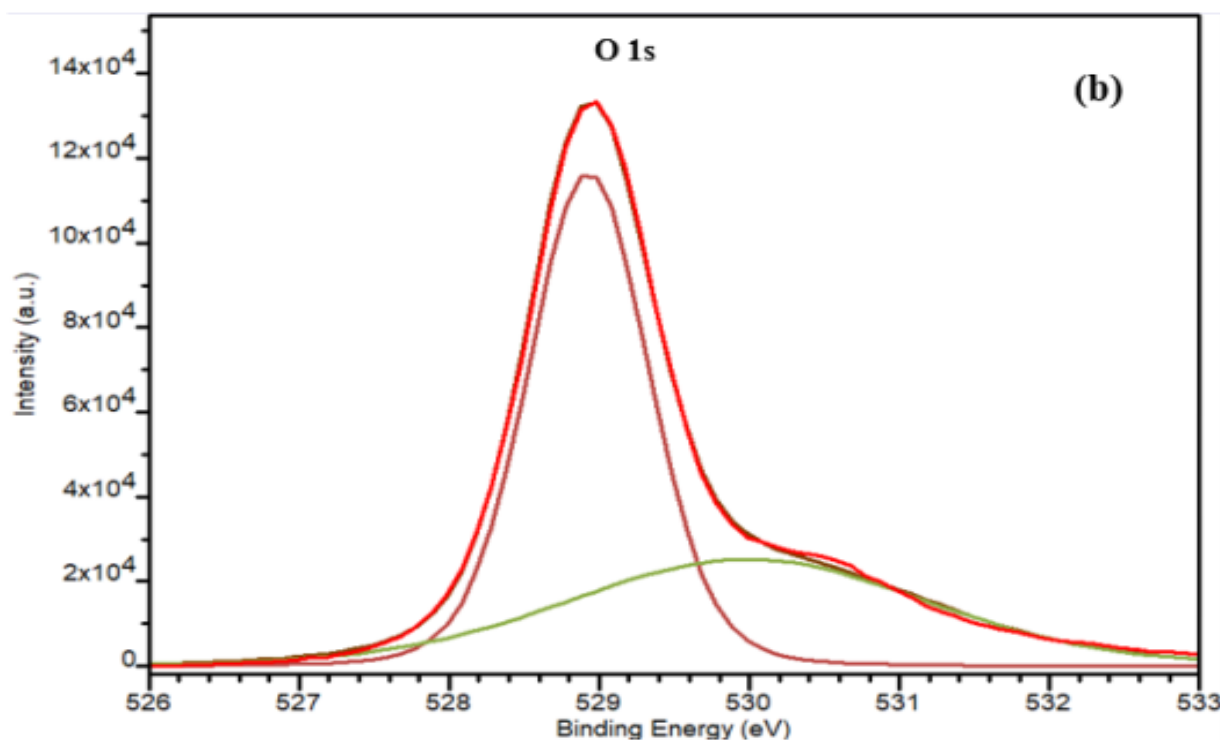


Figure 40 : XPS spectra of O (1s) transition and its fitting

The curve-fitted of XPS transitions of Mn (2p_{3/2}) core levels of Figure 41, reveals the apparition of three Gaussian peaks:

- 1- The first part: at 639.5 eV related to the presence of Mn²⁺.
- 2- The second part: at 641.5 eV, there is the presence of Mn³⁺.
- 3- The third part: at 644.4 eV related to the presence of Mn⁴⁺.

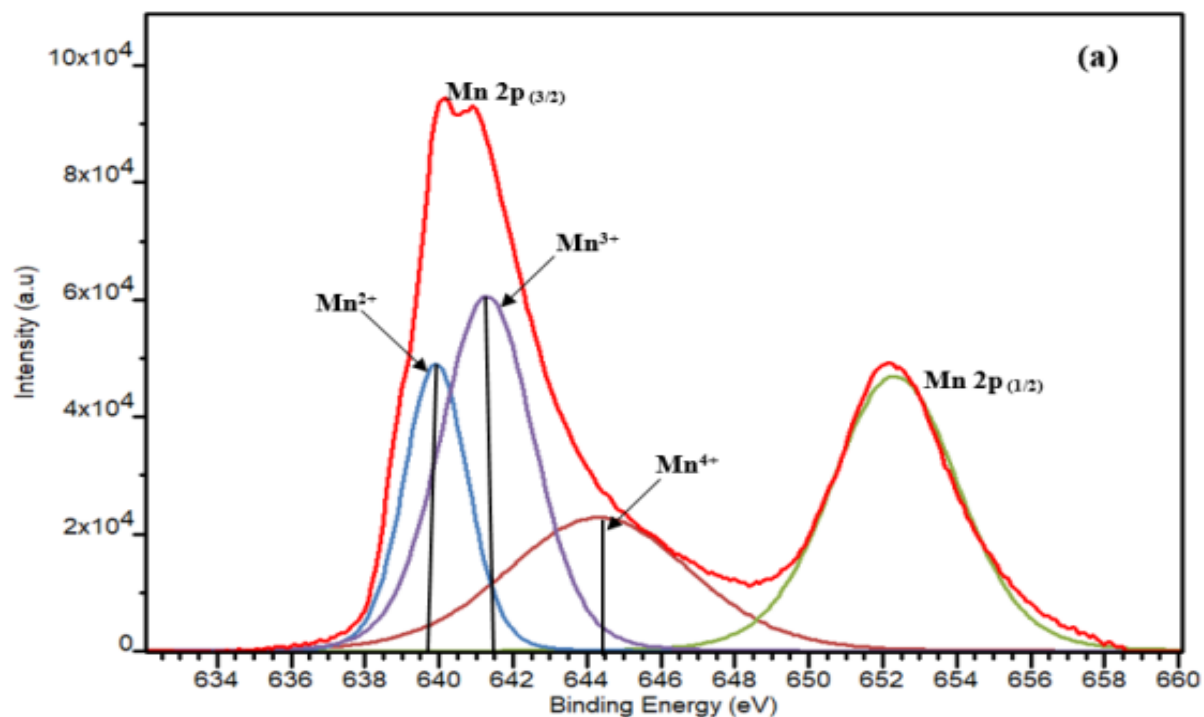


Figure 41 : Curve-fitted XPS spectra of Mn ($2p_{1/2}$) and Mn ($2p_{3/2}$) core level

These transitions of XPS spectra results can strongly depend on the manganese valence (Mn^{2+} , Mn^{3+} , Mn^{4+} which contribute to the formation of divers Mn-O oxides.

IV.II. Structural properties of Mn-O thin films:

IV.II.1. Mn-O films structure

The X-ray spectra of pure and Mg-doped manganese oxide were obtained by using XRD-X'Pert PRO from PANalytical diffractometer with the copper anode ($\lambda_{Cu} = 1.54\text{\AA}$). Figure 42 shows the diffraction spectra of Mn-O films deposited at glass substrates heated at 400°C . Several XRD patterns are detected. All these peaks can be assigned to the tetragonal Trimanganese tetraoxide phase in accordance with the JCPDS cards reference No. 00-024-0734, which confirm the presence of the tetragonal Trimanganese tetraoxide phase. There is no evidence of any other crystalline phase due to the presence of Mg doping which suggests that Mg is incorporated in the crystal lattice of Mn-O instead of forming its own oxide.

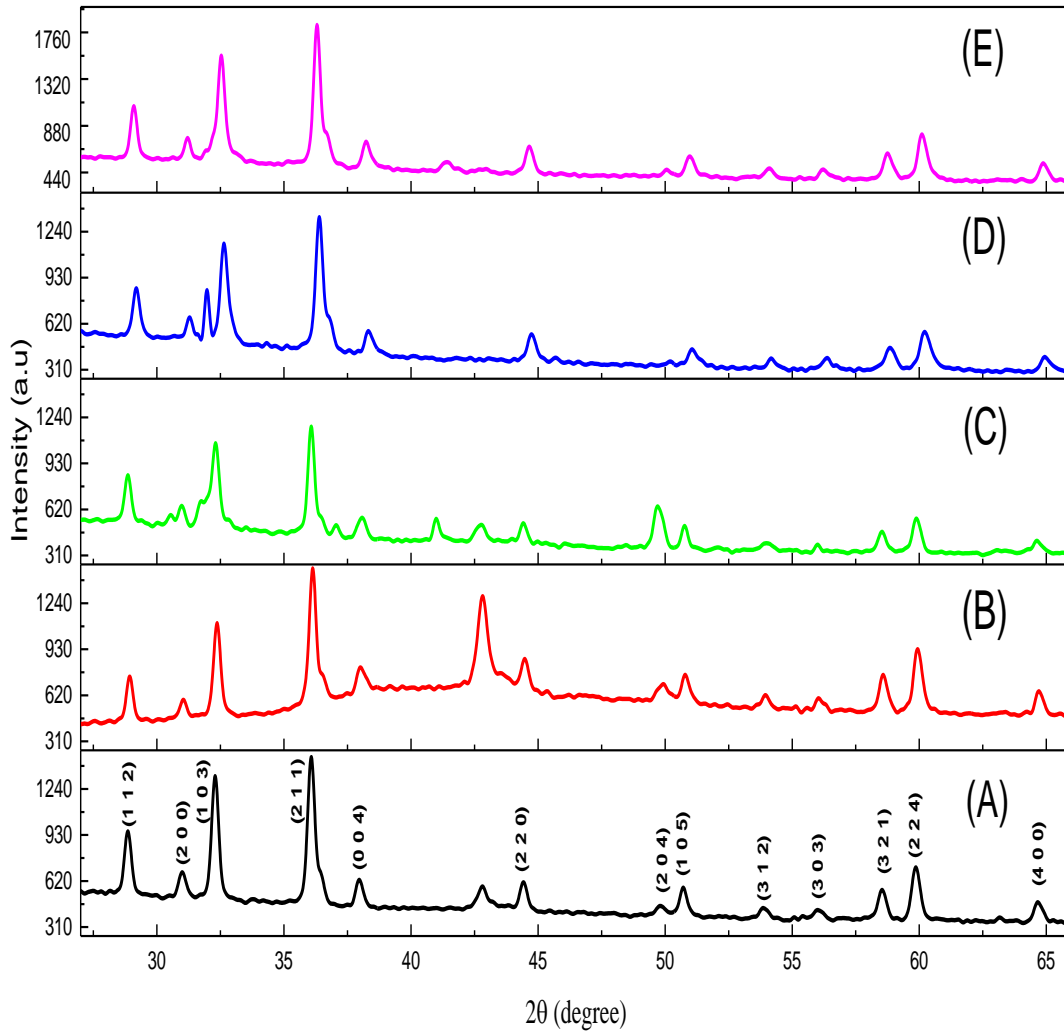


Figure 42 : X-ray diffraction spectra of pure and Mg-doped Mn-O thin films. (A); (B); (C); (D); (E) represent: MnO pur; 3% Mg-doped MnO; 5% Mg-doped MnO; 7% Mg-doped MnO; 9% Mg-doped MnO respectively.

The (112) at $2\theta = 28^\circ$, (103) at $2\theta = 32.5^\circ$, and (211) at $2\theta = 36.5^\circ$ dominate the XRD spectra of pure and Mg-doped Mn-O. As Mg doping levels increases, the intensity of the (211) plane's principal peak increases noticeably, especially at 7% and 9%, leading to observation shift in diffraction peaks.

These changes in the primary peak's intensity and position provide strong evidence of the enhanced crystallization of the thin films caused by Magnesium doping. However, the peak (220)

at approximately $2\theta = 43^\circ$ exhibits heightened diffraction that does not appear in other spectra, which may be due to instrumental error corresponding to improper sample placement during XRD analysis.

Furthermore, the XRD peaks display instability and oscillate to the left and right. As observed in XPS results, these fluctuations are attributed to the presence of both Mn^{2+} and Mn^{3+} ions, indicating the formation of a mixed oxide MnO and Mn_3O_4 .

The difference in atomic radii shown below is expected to destabilize the structure of the manganese oxide films because the radii of Mn^{2+} ions are enormous than others (the ratio between Mn^{2+} and Mg^{2+} is 1.77, which can help to explain the observed perturbations and shift of the peaks.

- Mn^{2+} with a radius of 1.17 Å
- Mn^{3+} with a radius of 0.66 Å
- Mn^{4+} with a radius of 0.60 Å
- Mg^{2+} with a radius of 0.66 Å.

We show in 7 that the position of (221) XRD pattern is unstable and shifts to the left and to the right, as observed on XPS spectra. These oscillations are attributed to the presence of two types of Mn valence Mn^{2+} and Mn^{3+} confirming the formation of a mixed oxide ($\text{MnO}/\text{Mn}_3\text{O}_4$). Similar behaviors were observed in a previous work on the XRD spectra of Sr doped-ZnO [4] and were attributed to a size effect between Zn^{2+} and Sr^{2+} ions. If we compare the ionic radii of the Mn^{2+} (1.17Å), Mn^{3+} (0.66 Å) and Mn^{4+} (0.60 Å) ions and of Mg^{2+} (0.66), it is only the Mn^{2+} ion that can explain the shift of the XPS and XRD peaks. The void resulting from the ratio $r_{\text{Mn}^{2+}}/r_{\text{Mg}^{2+}} = 1.77$ is expected to destabilize the crystallographic structure of the Mn-O film, which would cause the observed perturbations of the peak intensities (positions) in the XRD (and XPS) measurements.

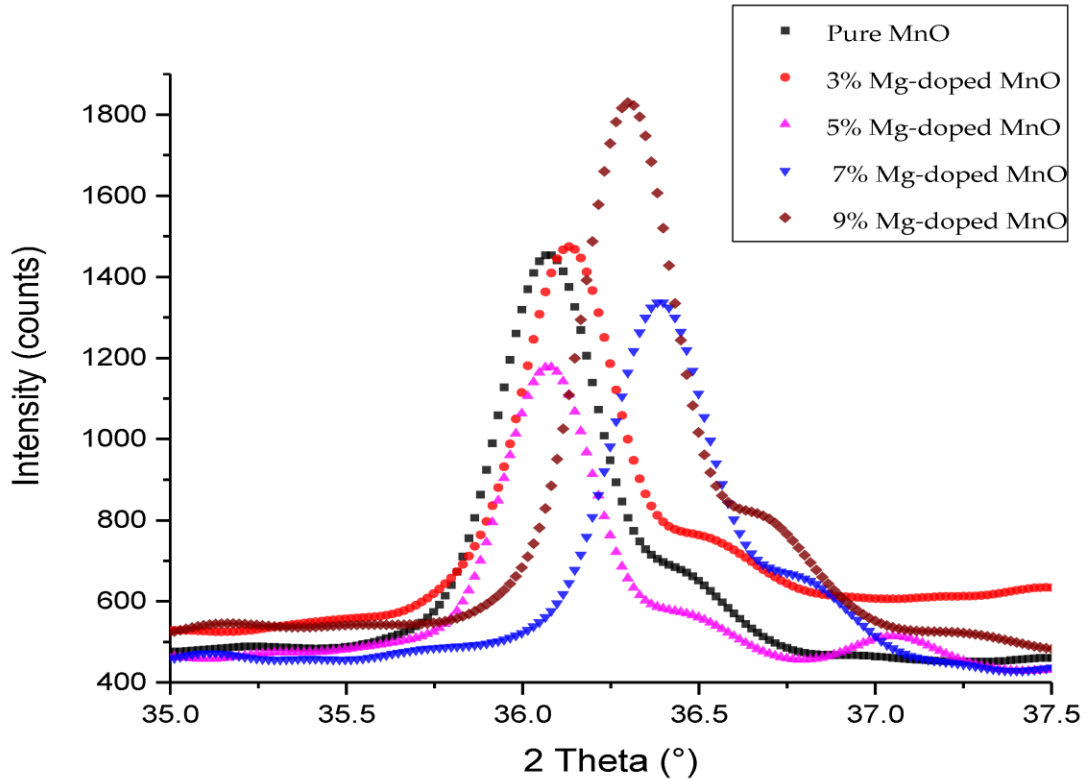


Figure 43 : Shift of the XRD peak (211).

IV.II.2. Exploitation of XRD spectra

i) Determination of Lattice parameters:

We have exploited XRD spectra for determining the lattice parameters of Mn-O films structure. As the dominant phases crystallize in tetragonal structure with the parameter:

$$a = b \neq c \quad \text{Eq. 19}$$

The interplanar spacing, denoted by ' d ', is determined by the values of ' a ', ' b ', and ' c ', as well as the indexed diffraction peaks (hkl). This relation can be expressed as follows:

$$\frac{1}{d^2} = \frac{(h^2 + k^2)}{a^2} + \frac{l^2}{c^2} \quad \text{Eq. 20}$$

d may be determined from Bragg's law:

$$2 \cdot d \cdot \sin\theta = n \cdot \lambda \quad \text{Eq. 21}$$

where:

1. d represents the distance between adjacent crystal planes,
2. θ is the Bragg diffraction angle,
3. n is an integer designing the order of diffraction, which is usually 1
4. λ denotes the wavelength of X-rays.

lattice parameters $a = b$ and c , obtained by combining equations (20) and (21) and applied to the most intense peaks (211) and (103) are listed in the following table:

Sample	$2\theta(^{\circ})$	(hkl)	$d(\text{\AA})$	$a=b (\text{\AA})$	$c (\text{\AA})$
Pure MnO	32.29	103	2.770	5.7643	9.4757
	36.08	211	2.488		
3% Mg-doped MnO	32.36	103	2.763	5.7565	9.4517
	36.13	211	2.488		
5% Mg-doped MnO	32.29	103	2.770	5.7647	9.4766
	36.07	211	2.487		
7% Mg-doped MnO	32.65	103	2.740	5.7166	9.3677
	36.39	211	2.466		
9% Mg-doped MnO	32.53	103	2.751	5.7302	9.4041
	36.31	211	2.472		

Table 2 determination of lattice parameters for the different Mg-doped manganese

ii) Determination of average size of the crystallites

Using the Debye-Scherer formula [5], the average size of the crystallites corresponding to the (211) peak D has been calculated from the diffraction peak widths. Equation (22) can be utilized to estimate the average Mn-O crystallite size, as demonstrated below:

$$D = \frac{0,9.\lambda}{\beta.2\theta.\cos\theta} \quad \text{Eq. 22}$$

Where:

- λ , the wavelength of X-rays
- θ , the Bragg diffraction angle
- β , the broadening of the diffraction peak at half its maximum intensity

The sizes reported in table 2 are the average size of the crystallites perpendicular to the substrate surface.

iii) Estimation of the density of defects in MnO films

From crystallites size, we can estimate the density of defects created in synthesized Mn-O films. These defects are in general dislocations line length per unit volume of the crystal. The density of dislocations is determined the following equation (23):

$$\delta = \frac{1}{D^2} \quad \text{Eq. 23}$$

Where D is average crystallite size of Mn-O determined from equation (2).

The values of δ are presented in the table below:

Sample	$2\theta_{(211)}$ (°)	d (Å)	B (°)	D (nm)	δ (10^{-3})
Pur MnO	36.08	2.488	0.3354	24.9075	1.6119
3% Mg-doped MnO	36.13	2.484	0.3088	27.0534	1.3663
5% Mg-doped MnO	36.07	2.487	0.2844	29.3722	1.1591
7% Mg-doped MnO	36.39	2.466	0.3624	23.0756	1.8779
9% Mg-doped MnO	36.31	2.472	0.3095	27.0081	1.3709

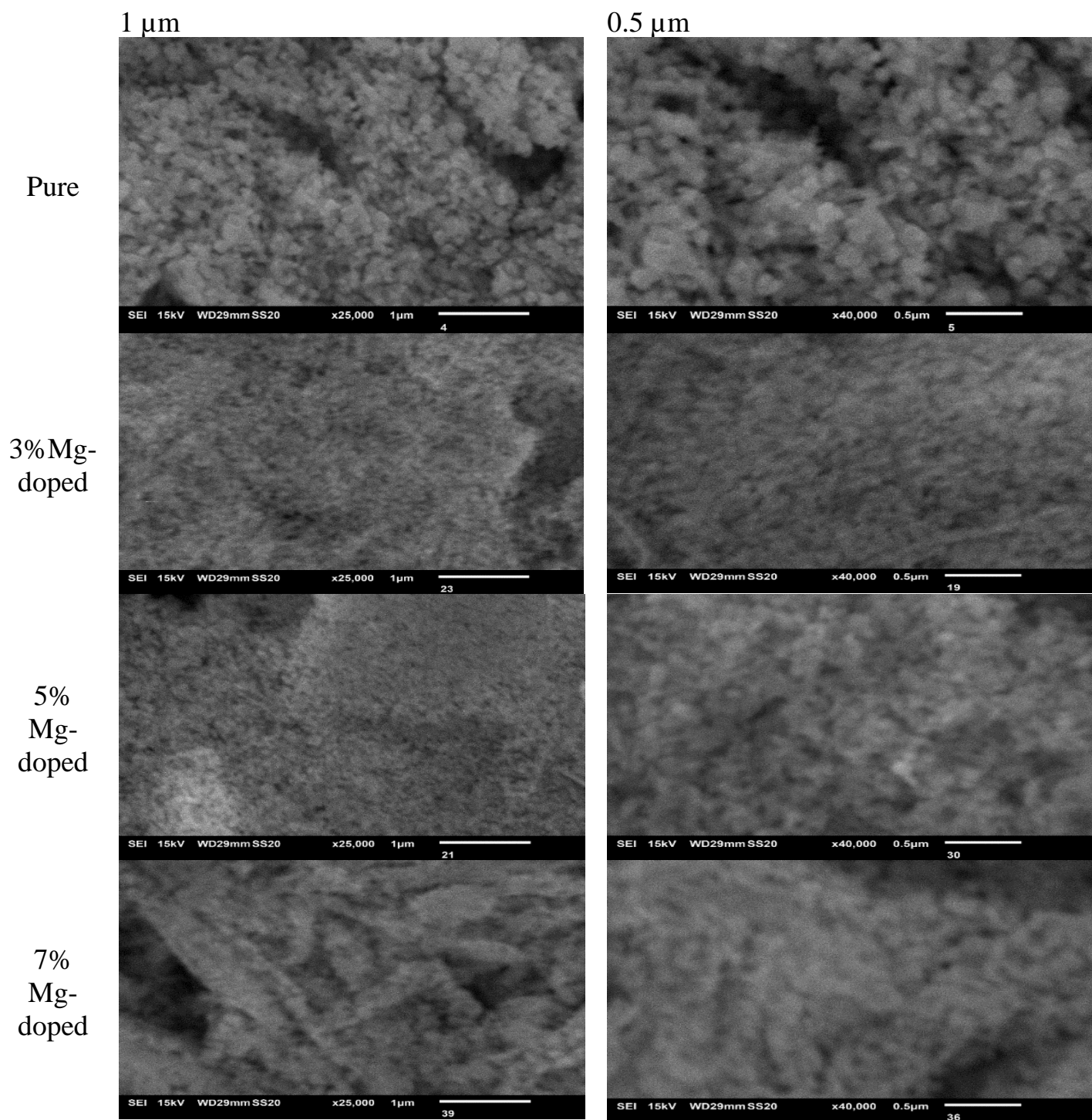
Table 3: The average size of crystallites (D) and the density of defects in thin films of MnO doped with various amounts of pur and Mg

IV.III. Morphological properties of Mn-O thin films:

IV.III.1. Scanning Electron Microscopy (SEM)

Scanning Electron Microscopy SEM was used to study the surface morphology of the pure and Mg-doped MnO films. Figure 44 shows SEM images with different magnifications which demonstrate a textured surface composed of crystallites of Mn-O depending on concentration of Mg-doping. Mg-doping appears to have an effect on the surface roughness with the pure MnO surface composed of larger grains, appearing rougher than other Mg-doped surfaces. The grain size increase follows the trend given by crystallite size determined from the XRD patterns where the pure MnO surface displays larger grains and appears rougher than the surfaces doped with Mg.

These findings suggest that Mg-doping influences the surface roughness of MnO and improves the surface morphology.



9%
Mg-
doped

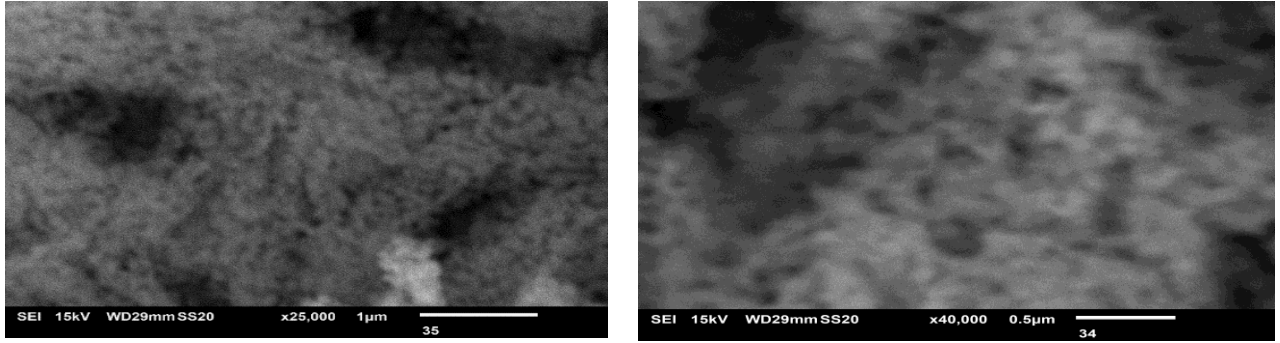
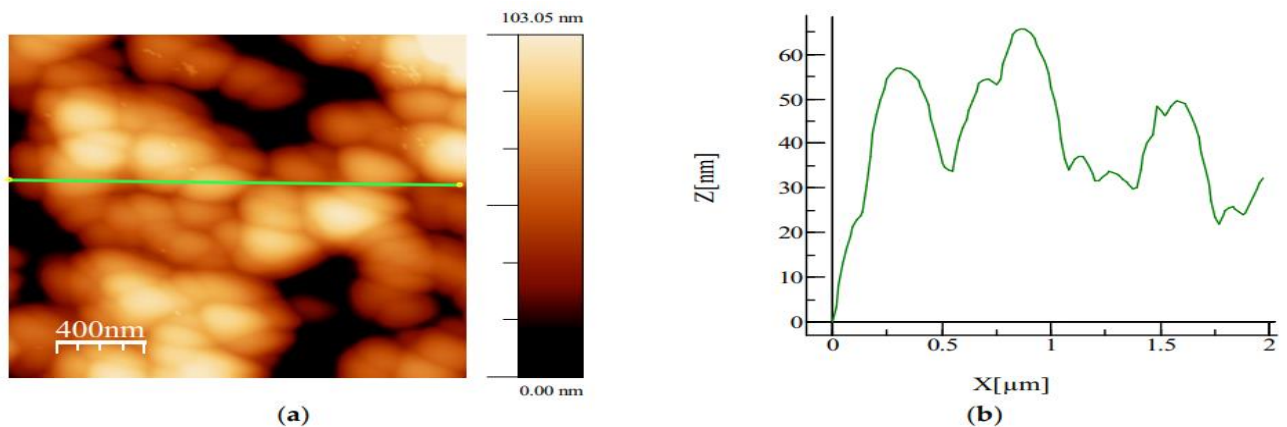


Figure 44 : SEM images of pure and Mg-doped Mn-O oxide recorded at different magnification

IV.III.2. Atomic force microscope (AFM) analysis

In Figure 45, we report AFM images obtained from pure and Mg-doped MnO in tapping mode by scanning $2\mu\text{m} \times 2\mu\text{m}$ scan areas. All AFM images were treated by WsXM software [6]. As shown in SEM images, Mg doping influences the surface structure. It is observed that the surface of pure MnO films is not homogeneous but it is formed by grains aggregated in “egg” shaped forms. The black areas represent the glass substrate showing the formation of MnO porous nanoflakes. As shown by the profiles taken on a horizontal line on each image, the aggregation of the grains increases with the increase of the Mg-doping. The calculated average rms roughness along this line is 50 nm for the pure MnO, 80 nm for 3% Mg doped-MnO and 130 nm for the 5%–7% Mg doped-MnO

..



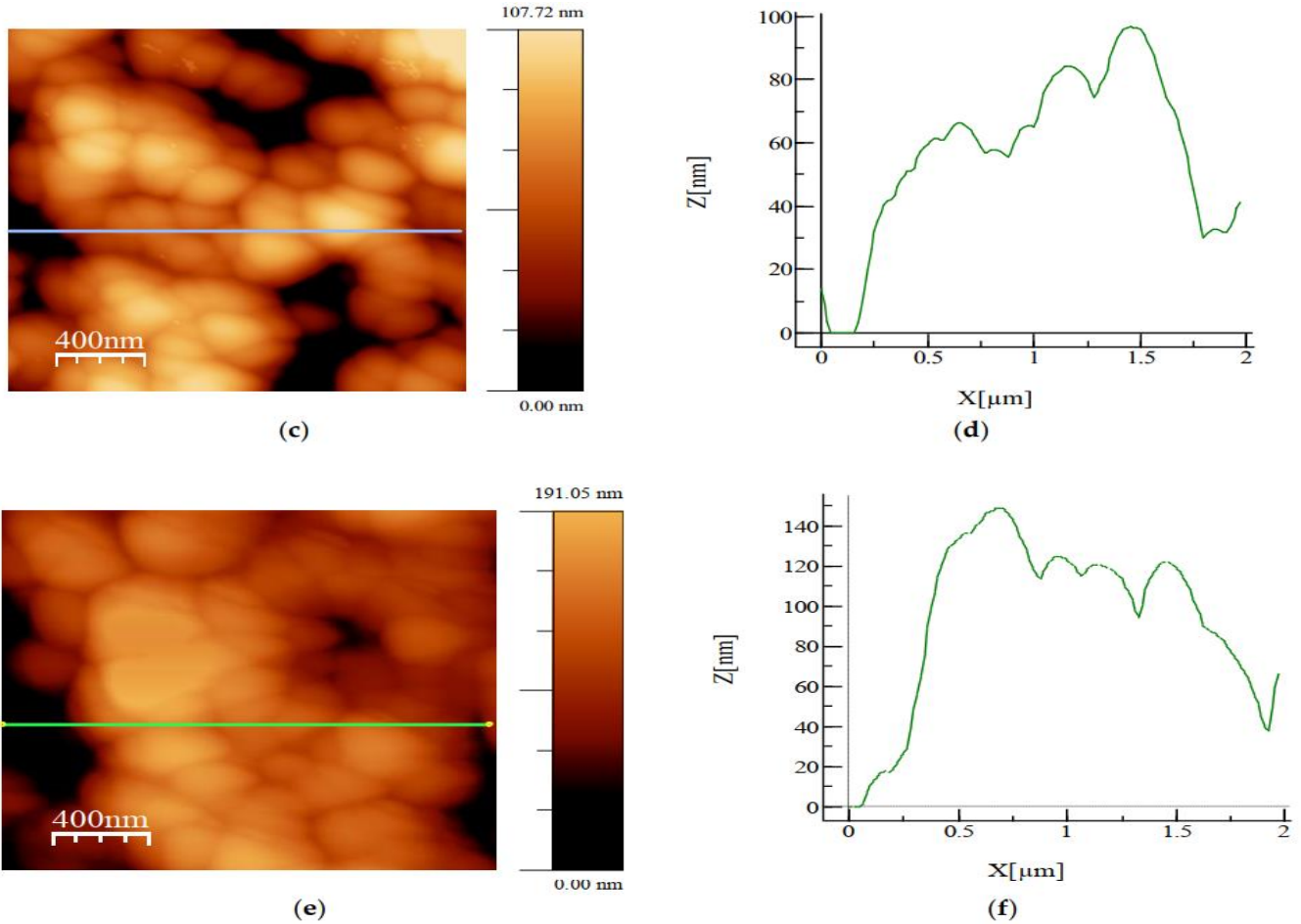
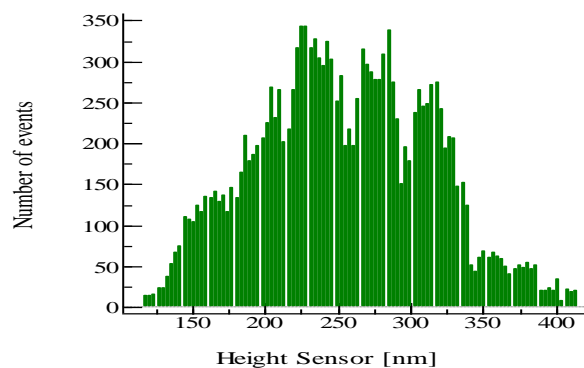
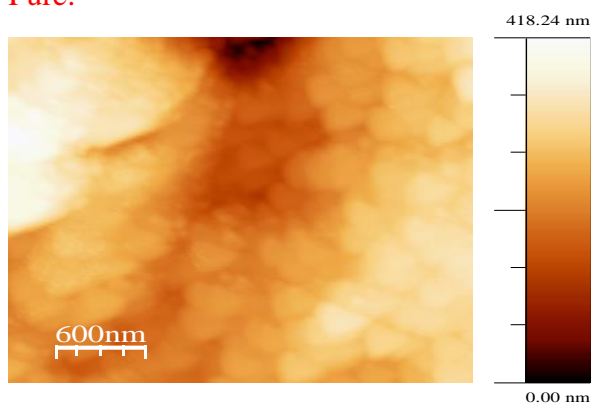


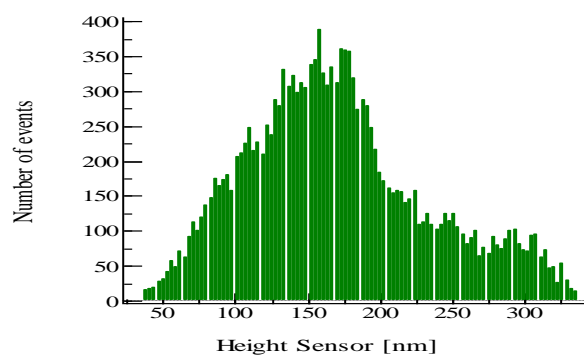
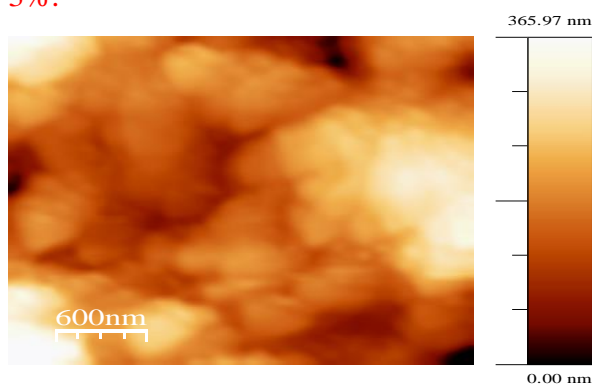
Figure 45 : AFM images of $2 \mu\text{m} \times 2 \mu\text{m}$ scan areas of Mg-doped Mn-O oxide (in left) with the profile of the horizontal line of each image (3%: a and b; 5%: c and e; 7%: e and f)(in right)

In Figure 46, we show that the morphology and roughness surface change with the scan areas. The histogram of roughness taken on all the scanned surface is depending on surface state and on the presence or no of doping as Mg.

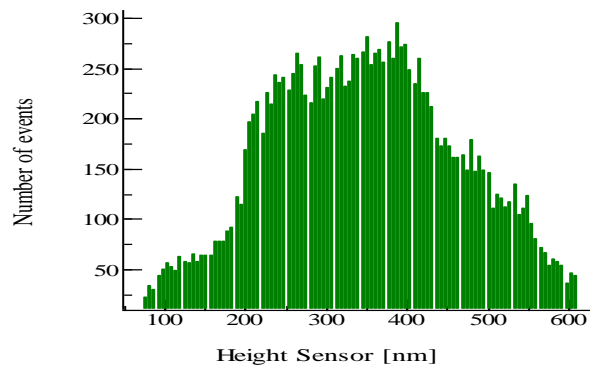
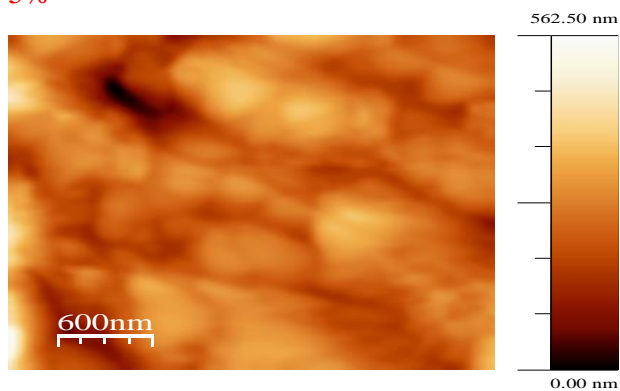
Pure:



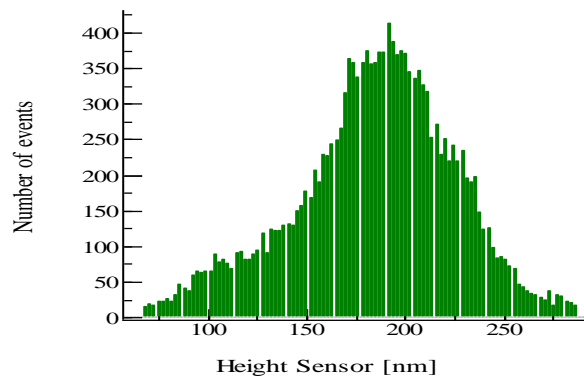
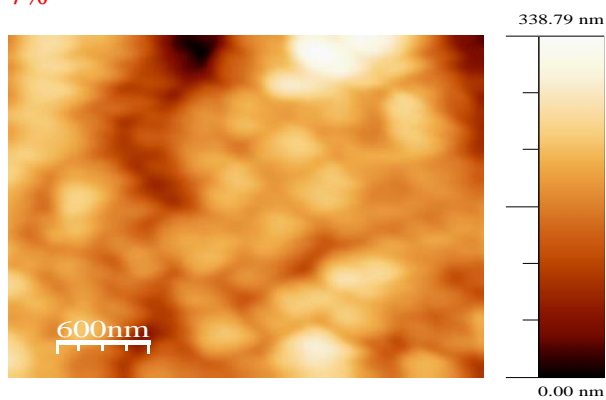
3%:



5%



7%



9 %

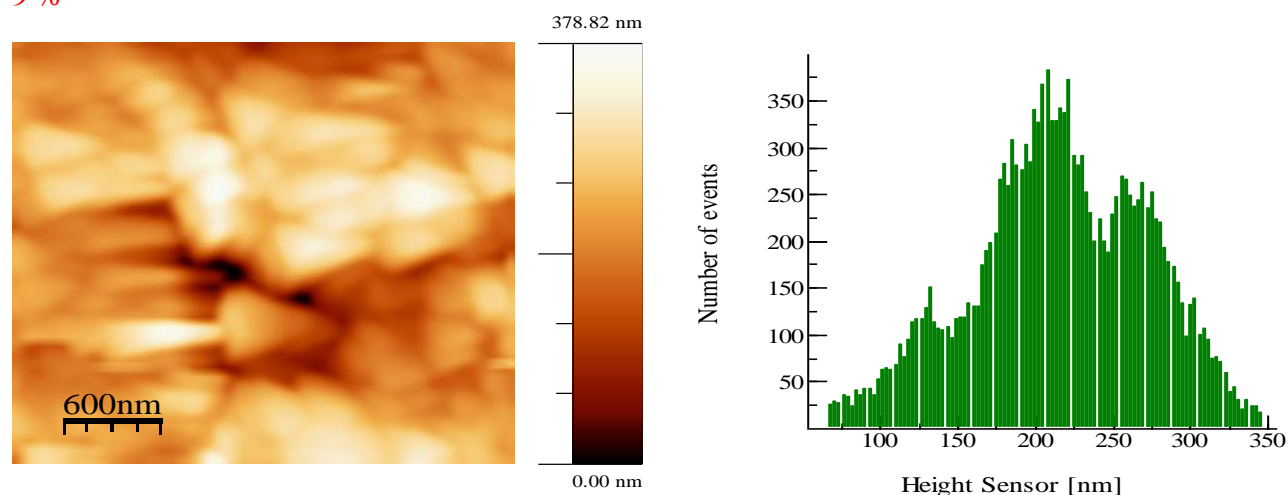


Figure 46 : AFM images of pure and Mg-doped Manganese oxide recorded in $3 \mu\text{m} \times 3 \mu\text{m}$ scan areas

IV.IV. Optical properties of Mn-O thin films:

IV.IV.1. Transmittance of deposited Mn-O films:

Figure 47 showed the transmittance (T) and absorbance (α) spectra of Mn-O films recorded in the 200–900 nm range. They are obtained by Uv-Vis spectrometer measurement using a double-beam spectrophotometer. The transmittance yield of Mn-O films relatively high (around 50%) indicates that pure and Mg-doped Mn-O films have good probability for transparent conducting oxide (TCO) layer application. The transmittance value of Mn-O thin films decreases slightly with increasing in Mg-doping concentration.

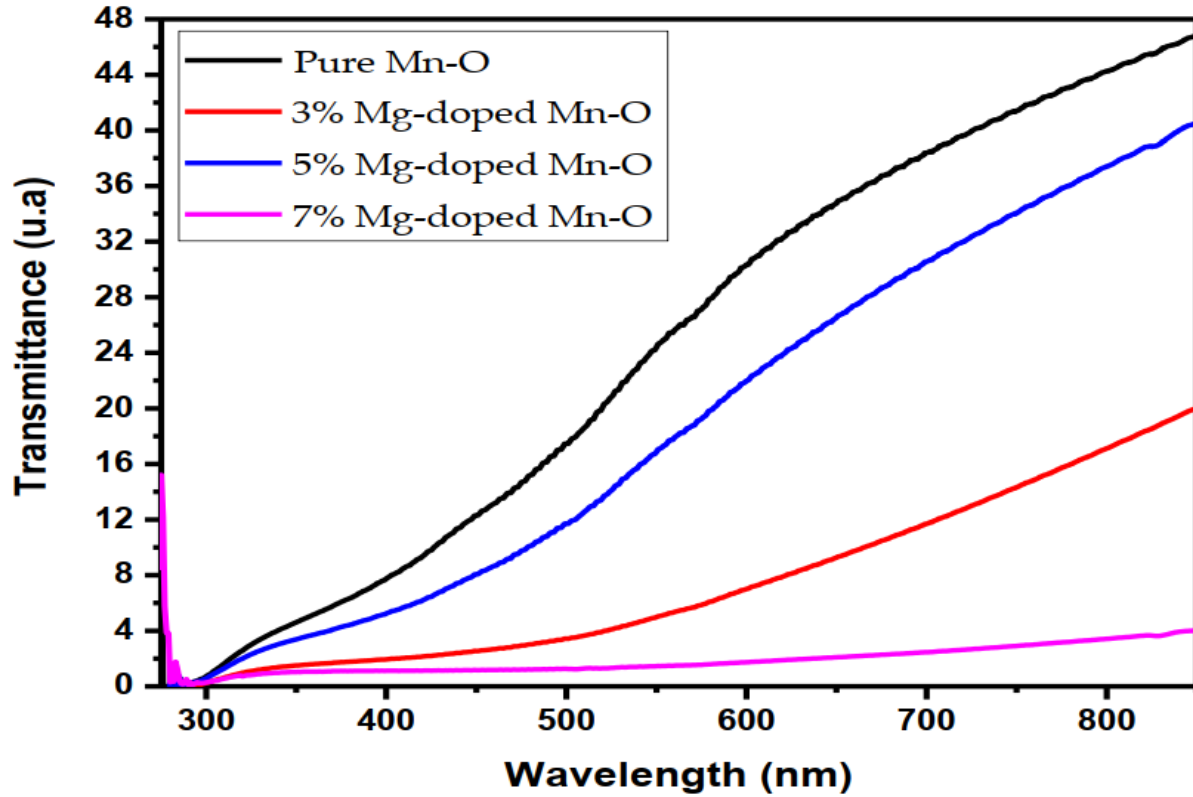


Figure 47 : The transmittance spectra of pure and Mg-doped Manganese oxide

Based on the data obtained from the samples, it can be observed that the transmittance levels are consistently below 50%, indicating that the synthesized films lack the desired level of transparency. The root cause of this issue has been identified as the inhomogeneity of the deposit, which has been confirmed by the AFM analysis.

The transmittance is varying from 50% to 15% for pure manganese oxide and to 9% for the Mg-doped Mn-O films; thus, the Mg doping reduces greatly the samples transparency.

IV.IV.2. Extraction of the band gap of Mn-O:

The MnO energy gap value can be calculated using Tauc's plot [7, 8], which involves combination of transmittance and absorption data. The calculation is done through the equation:

$$(\alpha h\nu)^2 = A(h\nu - E_g) \quad \text{Eq. 24}$$

where α represents the absorption yield, $h\nu$ is the photon energy, A is a constant = 1, and E_g denotes the band gap energy.

The graph in Figure 48 demonstrates a typical representation of $(\alpha h\nu)^2$ plotted versus $(h\nu)$ according to the relation (6).

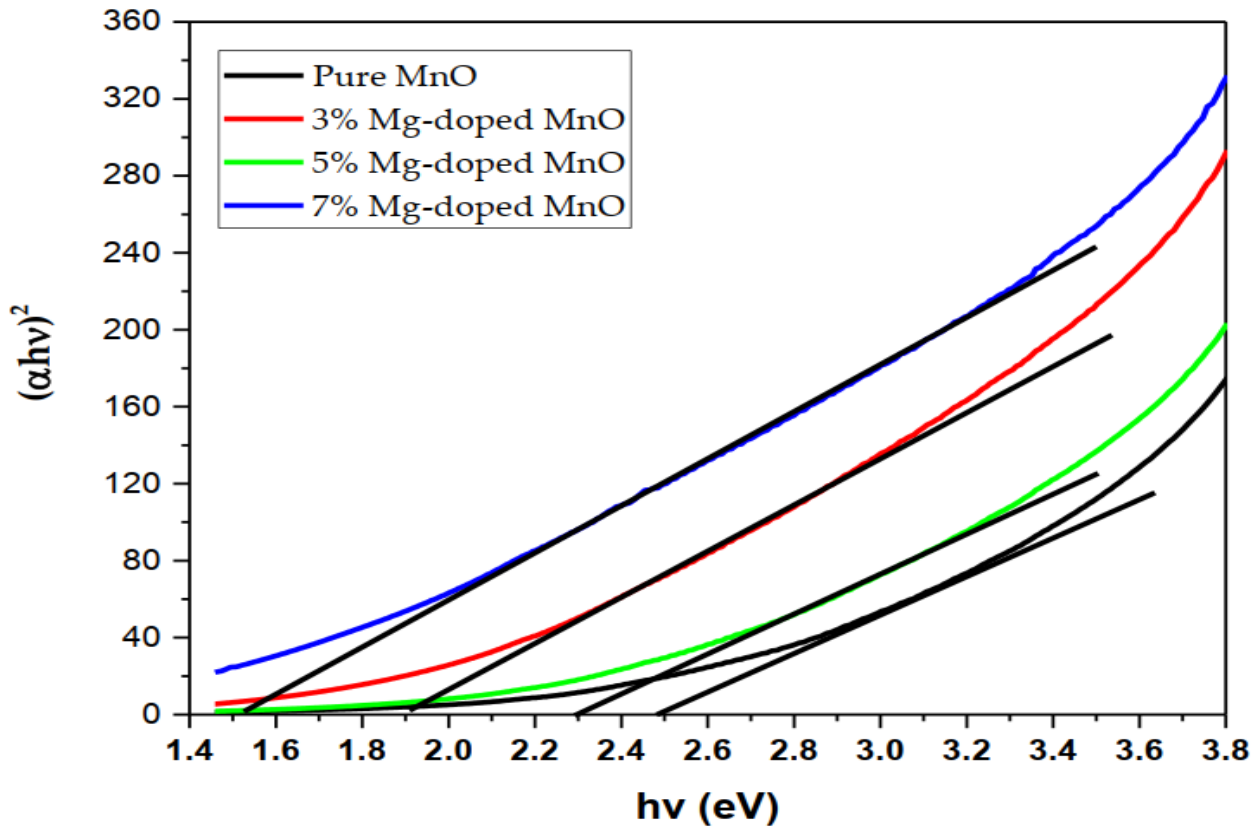


Figure 48 : The plot of $(\alpha h\nu)^2$ versus $(h\nu)$ according to Tauc's relation

The band gap values listed in the table below were obtained by extrapolating the linear portion of the curve in the Figure to $(\alpha h\nu)^2 = 0$, using the equation. The intersection of the linear portion with the $h\nu$ axis gives approximately the values of E_g .

These values of the band gap determined graphically are reported in table 3

Sample	Optic gap obtained (eV)	Optic gap (eV)
Pure MnO	2.5	1-2 [9] 2.23 [10] ; 2.6-2.8 [3] ;
3% Mg-doped MnO	1.9	
5% Mg-doped MnO	2.3	

<i>7% Mg-doped MnO</i>	1.5	
------------------------	-----	--

Table 4: Values of E_g determined graphically using Tauc's relationship

Although the values agree with those given in the literature, the obtained values of E_g are decreasing with the increase of Mg-doping. As interpreted in earlier paragraphs, this may be due to the greater ionic radius of Mg^{2+} ions compared to the Mn^{2+} . The insertion of Mg^{2+} in the Mn^{2+} sites create defects resulting from the distortion in the MnO lattice. The decrease in band gap with doping can be also linked to the presence of voids formed by the magnesium ions substituting the manganese ones in the host lattice. Similar results have been observed in Mg and Ga co-doped ZnO and in molybdenum-doped indium oxide thin films [11, 12]. In general, the band gap values obtained in this study for pure and Mg-doped samples are in the range of those reported in the literature [3, 10, 13, 14].

Bibliography of chapter IV

1. Shunmugapriya, B., et al., *Effect of cobalt doping on the electrochemical performance of trimanganese tetraoxide*. Nanotechnology, 2020. **31**(28): p. 285401.
2. Zhao, G., et al., *Mn₃O₄ doped with highly dispersed Zr species: a new non-noble metal oxide with enhanced activity for three-way catalysis*. New Journal of Chemistry, 2016. **40**(12): p. 10108-10115.
3. Sheikhshoaie, I., S. Ramezanzpour, and M. Khatamian, *Synthesis and characterization of thallium doped Mn₃O₄ as superior sunlight photocatalysts*. Journal of Molecular Liquids, 2017. **238**: p. 248-253.
4. Ouhaibi, A., et al., *The effect of strontium doping on structural and morphological properties of ZnO nanofilms synthesized by ultrasonic spray pyrolysis method*. Journal of Science: Advanced Materials and Devices, 2018. **3**(1): p. 29-36.
5. Taylor, A. and H. Sinclair, *On the determination of lattice parameters by the Debye-Scherrer method*. Proceedings of the Physical Society, 1945. **57**(2): p. 126.
6. Horcas, I., et al., *WSXM: A software for scanning probe microscopy and a tool for nanotechnology*. Review of scientific instruments, 2007. **78**(1): p. 013705.
7. Tauc, J., *Optical properties and electronic structure of amorphous Ge and Si*. Materials research bulletin, 1968. **3**(1): p. 37-46.
8. Makuła, P., M. Pacia, and W. Macyk, *How to correctly determine the band gap energy of modified semiconductor photocatalysts based on UV-Vis spectra*. 2018, ACS Publications. p. 6814-6817.
9. Sumantha, H., et al., *Green synthesis and characterization of Mn₃O₄ nanoparticles for photocatalytic and supercapacitors*. Ionics, 2023. **29**(2): p. 733-749.
10. Amara, M., et al., *Microstructural, optical and ethanol sensing properties of sprayed Li-doped Mn₃O₄ thin films*. Materials Research Bulletin, 2016. **75**: p. 217-223.
11. Tauc, J. and A. Menth, *States in the gap*. Journal of non-crystalline solids, 1972. **8**: p. 569-585.

12. Parthiban, S., et al., *High near-infrared transparent molybdenum-doped indium oxide thin films for nanocrystalline silicon solar cell applications*. Solar Energy Materials and Solar Cells, 2009. **93**(1): p. 92-97.
13. Zhou, W., et al., *Micro structural, electrical and optical properties of highly (2 2 0) oriented spinel Mn–Co–Ni–O film grown by radio frequency magnetron sputtering*. Applied surface science, 2014. **311**: p. 443-447.
14. Kovendhan, M., et al., *Prototype electrochromic device and dye sensitized solar cell using spray deposited undoped and 'Li'doped V2O5 thin film electrodes*. Current Applied Physics, 2015. **15**(5): p. 622-631.

General conclusion

General conclusion

The aim of this work is to offer some understanding on the properties of TCO films synthesized by soft chemical method. Thin films of pure manganese oxide (Mn-O) and magnesium (Mg) doped manganese oxide films have been deposited on substrate surface using spray pyrolysis technique. Manganese oxide (Mn-O) is considered as a transparent conducting oxide (TCO) which possesses potential applications used in a wide range domain as in: transparent electrodes for photovoltaic cells, touch panels, flat panel displays (FPDs), low emissivity windows, light emitting diodes, organic light emissive devices (OLEDs)... Transparent Conducting Oxide (TCO) materials exhibit optical transparency along with electrical conductivity where the nature of electrical conductivity arises from either excess electrons in the conduction band (n-type) or holes in the valence band (p-type) and is improved by doping without degrading their optical transmission. Coexistence of optical transparency and electrical conductivity in TCO materials depends on the nature, number and atomic arrangements of metal cations in oxides and on the presence of intrinsic defects.

Pure Mn-O and Mg-doped Mn-Oxide were synthesized on heated glass substrates by preparing an aqueous solution obtained from manganese chloride ($\text{MnCl}_2, 6\text{H}_2\text{O}$) with 0.1 M concentration. To obtain Mg-doped Mn-O oxide films, we add a second aqueous solution by dissolving in distilled water the precursor magnesium chloride hexahydrate ($\text{MgCl}_2, 6\text{H}_2\text{O}$). 3%, 5%, 7% and 9% Mg-doped Mn-O were used. The sprayed pure and Mg-doped Mn-O films were characterized using different experimental techniques such as:

XRD for structural study, X-ray photoelectron spectroscopy (XPS) elemental composition and oxidation state determinations, SEM and AFM for morphology and roughness analysis and uv-visible spectroscopy for transparent study of Mn-O films.

XRD characterization reveals spectra related to polycrystalline phases corresponding to a mixture of oxides as MnO, Mn_3O_4 , Mn_2O_3 and MnO_2 . One of these structures was confirmed in XPS analysis. The exploitation of the XRD spectra allowed us to determine the lattice parameters, the Mn-O particle size as well as the density of the defects.

XPS study confirms the presence of chemical species of Manganese (Mn) and Oxygen (O_2) which are the basic element in the formation of Mn-O films. As reported in XRD results, XPS is also sensitive the oxidation degree. The observed shifts in the binding energies of the Mn (2p) and O (1s) peaks show an average half-eV oscillation, which we attribute to the formation

of different chemical states of manganese observable in the composite oxides of MnO and Mn₃O₄.

At first, SEM and AFM analysis show textured and rough surface Mn-O films. which gradually changes with Mg-doping. Then, it is observed that a change in morphology of the Mn-O films as Mg-dopant concentration was increased. This tendency can be caused by incorporating Mg on the growing surface. From AFM images, we show that Mn-O surface is inhomogeneous where the grains are irregular shape aggregating in “egg” forms in pure MnO films with a maximum RMS roughness (50 nm), which can be explained by the coalescence of the crystallites having a small crystallite size.

As the Mg dopant increased from 3 to 7 %, the distribution of the crystallites on the surface morphology becomes homogeneous. Mg dopant has an effect of improving the morphology of Mn-O surface.

The optical properties of pure and Mg-doped Mn-O were determined from the transmission measurement in the range of 200–1000 nm. It is observed that the transmittance decreases slightly in the visible region ranges with the increase of Mg²⁺ concentration. The exploitation of the transmittance data, the direct band gap of pure and Mg-doped Mn-O films was determined using the Tauc’s relationship by intercepting of $(\alpha h\nu)^2$ versus photon energy ($h\nu$) plot. The band gap of Mn-O is found to be unstable; it varies from 2.5 eV for pure Mn-O to 1.5 eV after 7% Mg doping. This behavior may be attributed to defects introduced after Mg²⁺ substitution for Mn²⁺ and then enters into the Mn-O lattice due to the difference in electronegativity and ionic radius between Mn and Mg. The fact in having a mixture of Mn-O oxides (MnO, Mn₃O₄, Mn₂O₃ and MnO₂) can be explained by the variations of the value of E_g .

We planned to study electrical properties Mn-O films depending on Mg doping concentration but due to the lack of experimental equipment, we were unable to carry out this study. We will have postponed at later time it until later.

List of publications and communications issued from this work:

International publications:

- 1) Malika, A. ; Dahamni, M.A.; Ghamnia, M.; Boukhachem, A.; Boukrédimi, D.; Tonneau, D.; Fauquet, C. Synthesis and Investigation of Pure and Cu-Doped NiO Nanofilms for Future Applications in Wastewater Treatment Rejected by Textile Industry. *Catalysts* 2022, 12, 931. <https://doi.org/10.3390/catal12090931>
- 2) Aroussi, S.; Dahamni, M.A.; Ghamnia, M.; Tonneau, D.; Fauquet, C. Characterization of Some Physical and Photocatalytic Properties of CuO Nanofilms Synthesized by a Gentle Chemical Technique. *Condens. Matter* 2022, 7, 37. <https://doi.org/10.3390/condmat7020037>
- 3) Ouhaibi, A.; Saoula, N.; Ghamnia, M.; Dahamni, M. A.; Guerbous, L. Effect of Deposition Temperature on Morphological, Optical, and Photocatalytic Properties of ZnO Thin Films Synthesized by Ultrasonic Spray Pyrolysis Method. *Crystal Research and Technology* 2022, 57, 2100224. <https://doi.org/10.1002/crat.202100224>
- 4) Dahamni, M.A.; Ghamnia, M.; Naceri, S.E.; Fauquet, C.; Tonneau, D.; Pireaux, J.-J.; Bouadi, A. Spray Pyrolysis Synthesis of Pure and Mg-Doped Manganese Oxide Thin Films. *Coatings* 2021, 11, 598. <https://doi.org/10.3390/coatings11050598>
- 5) Hacini N.; Ghamnia M.; Dahamni M.; Boukhachem A.; Pireaux J.; Houssiau L. Compositional, Structural, Morphological, and Optical Properties of ZnO Thin Films Prepared by PECVD Technique. *Coatings*, 10 February 2021, 11(2), 202. <https://doi.org/10.3390/coatings11020202>.
- 6) Youcefi Z.; Ghamnia M.; Dahamni M.; Loukil A.; Bousbahi K. Extraction of some trapping parameters from experimental thermoluminescence (TL) signal of alumina (α -Al₂O₃) using analytical models. *Chinese Journal of Physics*, 30 December 2020, 70, 82-90. Doi: doi.org/10.1016/j.cjph.2020.12.017.
- 7) Benameur, N.; Chakhoum, M.; Boukhachem, A.; Dahamni, M.; Ghamnia, M.; Hacini, N.; Pireaux, J.; Houssiau, L.; Ziouche, A. Investigation of some physical properties of pure and Co-doped MoO₃ synthesized on glass substrates by the spray pyrolysis method. *Journal of Electron Spectroscopy and Related Phenomena*, 2019, 234, 71–79. doi: 10.1016/j.elspec.2019.05.01.

National and international communications:

1. Etude structurale, optique et catalytique des couches nanométriques de NiO dope au baryum synthétisées par spray pyrolyse, Centre de Recherche Nucléaire de DRARIA du Commissariat à l'Energie Atomique, Algérie, 16-18 Décembre 2019.
2. Zicaloy-4 present limitations and future advanced claddings, a review, Université Oran 1, Algérie, 09-11 Mars 2020
3. Synthesis and Characterization of Pure and Mg Doped MnO, Centre de Recherche Nucléaire de DRARIA du Commissariat à l'Energie Atomique, Algérie, 10-12 Octobre 2022.